TÉCNICO LISBOA

Design Study of a Side Intrusion Beam for Automotive Safety

Pedro Gomes Mota Rebelo

Thesis to obtain the Master of Science Degree in

Aerospace Engineering

Supervisor(s): Prof. André Calado Marta
Eng. Tiago Marcelino

Examination Committee

Chairperson: Prof. Filipe Szolnoky Ramos Pinto Cunha
Supervisor: Prof. André Calado Marta
Member of the Committee: Prof. Virginia Isabel Monteiro Nabais Infante

November 2016

Dedicated to my grandmother

Acknowledgments

First and foremost, I would like to thank my supervisors, Engineer Tiago Marcelino, from CEIIA, and Professor André Calado Marta, from Técnico Lisboa, for all the support, encouragement, knowledge and expertise, provided continuously during the development of the present work. Their guidance is immensely valued, and to them I am greatly grateful.

To CEIIA, and all my colleagues, specially Pedro Talaia, José Silva and Inês Crespo, for sharing their experience and for providing the tools I needed to develop this thesis.

To Técnico Lisboa, the school where I spent the last five years of my academic life, where I understood the real meaning of hard work, perseverance and excellency. To all my colleagues which helped me throughout this degree, I am sincerely grateful.

To my colleagues Tiago Torre, Henrique Raposo and Pedro Carvalheiro for riding alongside me in this amazing journey.

To Miguel Pinto, my best friend, for always being present and supporting me through the best and the hardest moments of my life. To João Maria Pedra Soares for proving me that it is never too late to start a great friendship, and for all the help and support towards the development of this thesis. To Francisco Gomes, my mentor, who taught me the self-discipline and the search for excellency I applied everyday when developing the present work.

To my parents. They are the reason I got to this moment of my life. To them, I owe everything, and for their unconditional support I will be forever grateful.

Finally, to Joana Rebelo. Her support and her friendship are the key elements of my life. She gave me the strength and the happiness I needed to pursue this goal, to endure each and every setback and to successfully develop this thesis. Thank you!

Resumo

A segurança rodoviária constitui uma das principais preocupações globais no que diz respeito à proteção de vidas humanas. Todos os anos, 1.2 milhões de pessoas morrem em acidentes rodoviários, e outros 20-50 milhões sofrem lesões não fatais. Depois do impacto frontal, a colisão lateral é a principal causa de morte em acidentes rodoviários. O projeto de sistemas de segurança que previnam a ocorrência do acidente, ou que controlem o efeito que este possa ter nos passageiros, é uma área de pesquisa global, na qual se insere o desenvolvimento deste trabalho.

A viga de intrusão lateral é um componente protetor instalado na porta do veículo, projetado para melhorar a segurança dos passageiros no evento de um impacto lateral. O papel desta estrutura passa pela absorção do máximo valor de energia de impacto possível, através de um processo de deformação elasto-plástica. As vigas de paredes finas são uma solução usualmente selecionada pela sua grande capacidade de absorção de energia. Essa mesma capacidade têm os materiais metálicos, consequência da sua elevada resistência mecânica associada a uma grande ductilidade. O trabalho desenvolvido concentra-se no estudo do impacto da geometria da secção e do material metálico aplicado no desempenho à flexão das vigas de paredes finas. Com um maior desempenho à flexão da viga, é esperada uma melhor resposta ao impacto por parte do veículo completo.

Uma vez atingidas melhorias significativas no desempenho à flexão da viga, as soluções são instaladas num modelo numérico de um veículo e testadas em diferentes configurações de impacto. A viga de intrusão lateral apresenta um efeito benéfico no ensaio específico de impacto lateral contra um poste, diminuindo a intrusão do mesmo no habitáculo do veículo.

Palavras-chave: vigas de paredes finas, absorção de energia, desempenho à flexão, desempenho ao impacto, deformação elasto-plástica

Abstract

Road safety is one of the major global concerns regarding the protection of human lives. Every year, 1.2 million people die in road related accidents, and 20-50 million suffer from non-fatal injuries. After frontal crash, side impact is the leading cause of road fatalities. Designing safety systems for preventing the accident, or controlling the damages it inflicts on the passengers once it occurs, is a global research subject in which the work developed in thesis is inserted.

The side intrusion beam is a protective component installed in the vehicle door, designed to enhance passengers safety in the event of a side collision. This structure's role is to absorb the maximum amount of impact energy through an elasto-plastic deformation process. Thin-walled beams are frequently applied due to their high energy absorption capacity. Metals are commonly selected for the beam design, since they combine a high strength with an also high ductility, both crucial to energy absorption. The present work focuses on studying the impact of the cross-section geometry and material of a thin-walled beam in its bending performance. With a higher bending performance of the side intrusion beam, a better overall performance in a crash event is expected.

After significant improvements in bending performance are achieved, the beam solutions are installed in a complete vehicle and tested in different crash configurations. The side intrusion beam is proven to improve the crash performance under specific conditions, for example, during a side pole impact, where the intrusion levels are reduced by the installation of this component.

Keywords: thin-walled beams, energy absorption, bending performance, crash performance, elasto-plastic deformation

Contents

List of Tables

List of Figures

Nomenclature

Greek symbols

α	Top anlge.
β	Bottom angle.
Δ	Change.
δ	Increment; displacement.
σ	Stress.
θ	Rotational angle.
υ	Poisson's ratio.
ε	Strain.
ρ	Density.

Roman symbols

A	Area.
a, b	Cross-section characteristic dimensions.
C	Center of curvature.
C	Weight coefficient.
c	Half of cross-section height.
D	Diameter.
d	Distance between nodes.
E	Modulus of elasticity.
F	Force.
H	Material strain constant.
h	Beam height.

I Second moment of area.

L Length; door level.

M Moment; mass.

m, n Geometric parameters

n Strain hardening coefficient.

R Radius.

S Span.

t Time; thickness.

W Width.

x, y, z Cartesian components.

Subscripts

$0, y$ Yield point.

$1, 2, 3, 4, 5, 6, 7, 8, 9$ Configuration index.

avg Average.

c Edge of cross-section.

e Elastic.

$freq$ Frequency.

i Initial.

m Geo Metro model.

max Maximum.

mdb Moving deformable barrier.

min Minimum.

p Plastic.

$pole$ Pole.

R Failure.

run Simulation.

UTS Ultimate tensile strength.

x, y, z Cartesian components.

ref Reference condition.

Glossary

ABS	Antilock Braking System
AEB	Autonomous Emergency Braking
AHSS	Advanced High Strength Steel
APC	Abdomen Performance Criteria
CFE	Crash Force Efficiency
CNC	Computer Numerically Controlled
EA	Energy Absorption
ESP®	Electronic Stability Programme
FEA	Finite Element Analysis
HPC	Head Performance Criteria
JASIC	Japan Automobile Standards Internationalisation Center
MDB	Mobile Deformable Barrier
NCAP	New Car Assessment Programme
NHTSA	National Highway Traffic Safety Administration
PPC	Pelvis Performance Criteria
PPSS	Pedestrian Passive Safety Systems
RS	Road Safety
SEA	Specific Energy Absorption
SIB	Side Intrusion Beam
TCS	Traction Control System
TPC	Thorax Performance Criteria
UNECE	United Nations Economic Commission for Europe
VRU	Vulnerable Road User

Chapter 1

Introduction

1.1 Motivation

Automotive safety is a major global concern addressed by several organizations worldwide, including the United Nations through its agency World Health Organization [1]. 1.2 million fatalities are registered every year [2] and many more are injured in road accidents. More than one third of the automotive accidents are related with side collisions [3] and about 35% of those accidents are proven fatal [4]. For this reason, designing new and better lateral safety systems is of the outmost relevance.

Crashworthiness is the ability of a vehicle to absorb impact energy and protect the vehicle occupants in case of an accident [5]. Cars are designed with multiple protective systems which intend to increase the vehicle crashworthiness. One of those elements is the side intrusion beam (SIB). This element is installed inside the vehicle doors and has the main goal of increasing passengers safety during a side crash. As the door assembly is all that stands between the passenger and the external object, all of its components, including the SIB, play a major role regarding the vehicle's crashworthiness.

SIB development has been the object of study for many authors. Maximizing energy absorption efficiency and attenuating the impact peak force are two crucial factors when designing a side intrusion beam [6]. Energy absorption efficiency means having the lightest beam absorbing the maximum impact energy. This concern rises from the imperative need of decreasing vehicle's weight in order to achieve international environmental milestones [7]. Controlling the impact peak force is of very importance as well, since occupant damage may arise from two situations [8]: direct contact between the impactor, or any other car component, and the passenger, or extreme accelerations induced to the human body, which are a direct result from the applied forces during the crash event. The SIB can, in these cases, help preventing the crushing of the occupant compartment and simultaneously induce a slower deceleration of the the impacting vehicle leading to a lower peak force and a softer collision event. Tang et al. [9] justify that thin-walled beams are the most appropriate solution to the SIB development due to their high reliability and excellent energy absorption capacity. Chen [10] and Zhang et al. [11] note that thin-walled beams will collapse in bending mode and, for that reason, the bending performance of the SIB becomes a matter of central importance.

The three-point bending test is a simple and effective procedure to evaluate the bending performance of beams. Authors have used this test to compare different thin-walled beams geometries and materials. Tang et al. [9] compared simple geometries and studied the introduction of inner reinforcements. Zhang et al. [6] wanted to understand how thickness distribution could affect the beam's performance. Černiauskas et al. [4] studied both open and closed profiles and different grades of steel to understand the effect of the mechanical properties on the bending performance of the SIB.

This thesis will focus on the bending performance of several geometries and materials, motivated by the previous work developed in this area, looking forward to develop a wide and comprehensive study on thin-walled beams. The results on improved bending performance will then be set as base to understand the usefullness of the side intrusion beam as protective element in the event of a side collision. This is of particular importance since the benefits of the SIB have been questioned by some authors, namely Preston and Shortridge [8] who, after conducting experimental tests, could not conclude on the effectiveness of the SIB on preventing passengers injuries or door penetration.

CEIIA had a crucial role in this study development as it, not only motivated the subject as part of the development of an electric vehicle which integrates the Be project, but also by supplying the tools and a significant knowledge network which made this thesis possible. Side impact testing is required to achieve international homologation and a lightweight solution is crucial in the development of a sustainable vehicle.

The work presented in this thesis was conducted to obtain the Master of Science degree in Aerospace Engineering, despite its focus relying on the development of an automotive safety system. The aerospace and automotive industries are certainly different. However, several study subjects are of common interest for both fields, such as the study of the bending behavior of beams. In an aeronautical application, the elastic bending of the wing's structural beams is crucial to evaluate this component's flexibility, which is of particular importance for high aspect ratio wings. Not only the subjects studied may be shared, but also the tools used to design and evaluate the structural components of both air and ground vehicles. The finite elements numerical tool used in this thesis, HyperWorks, is also applied to the aerospace industry to predict static and dynamic responses, significantly reducing the product's development costs.

1.2 CEIIA

CEIIA – Centro para a Excelência e Inovação na Indústria Automóvel is a center of engineering and product development that designs, implements and operates innovative products and systems for the aeronautic, mobility, naval/offshore and automotive industries. It is one of the main innovation hubs in Portuguese territory and currently employs over 200 engineers. Located in Matosinhos city, in the north region of Portugal, CEIIA is a non-profit organization which deeply cares about the community where it is inserted, promoting the development of future generations, encouraging the growth of a sustainable environment.

The development of the Be project has multiple goals [12]:

- To attract new investment associated to new logics of motorization and mobility services;

- To develop a national industrial cluster with capacity to design, develop, industrialize and test electric vehicles and integrated services for the new environments of sustainable mobility;
- To position Portugal as a world reference in Electric Mobility and export an integrated solution (system, service and vehicle).

The Be project focuses on the development of a 100% electric vehicle which comprises all the above objectives. CEIIA, in a partnership with several other Portuguese and international entities, is responsible for the design and conception, engineering and virtual validation of the full product. This thesis is integrated in the development of a safety system for the vehicle door, the side intrusion beam.

1.3 Objectives

This thesis focuses on studying the impact of geometry and material selection in a thin-walled beam bending performance. This work aims to develop an improved solution for a side intrusion beam to be applied in a future electric vehicle designed and engineered by CEIIA as part of the Be project. Determining an optimal solution, however, is dependent on several project requirements which, due to the early stage of its development, are still not available. For that reason, a wide range of solutions will be tested under a three-point bending configuration. Its equivalent numerical model will be built and validated to assess the beam's bending performance. A selection tool will be created to assist the decision process regarding the shape and the material of the final configuration for the side intrusion beam.

After determining which factors affect the most the beam's bending performance, a secondary analysis will be run in order to study how the bending performance improvement of a thin-walled beam relates with vehicle behavior during a side impact. This thesis aims to test both the side pole impact test and the side impact collision test in order to understand how the SIB helps protecting passengers in case of accident and how this protection can be efficiently enhanced. Figure 1.1 sums up the the objectives of this thesis.

1.4 Thesis Outline

This first chapter made an initial introduction to the problem studied throughout this thesis, and the motivation behind the development of a side intrusion beam.

Chapter 2 introduces the theme of road safety. Accidents related data show the importance of developing new and improved safety systems. Regulations for lateral impact are presented and some research is made on the state of the art for side intrusion beam development. A theoretical review on plastic deformation is also covered in this chapter.

Chapter 3 covers a description of both the problem approach and the numerical tools used to develop the several analyzes ran throughout this thesis.

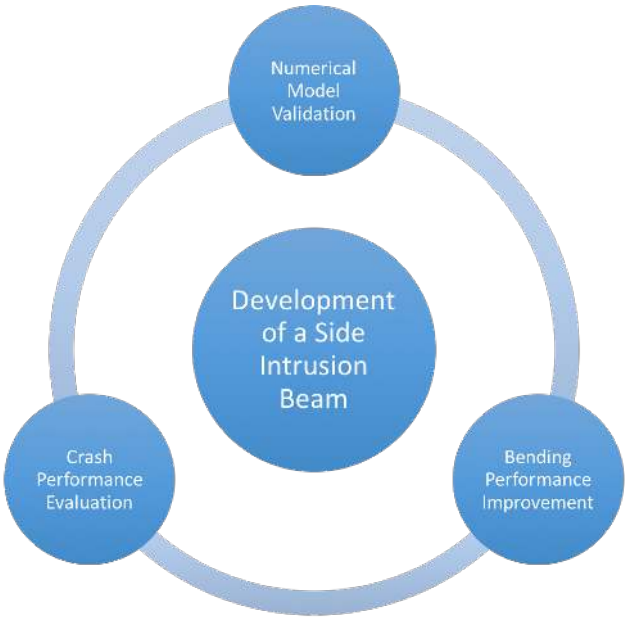

Figure 1.1: Thesis objectives

Chapter 4 concerns the development and validation through experimental testing of a three-point bending numerical model in order to evaluate thin-walled beam bending performance.

Chapter 5 comprehends an extensive study on the bending performance of several cross-section geometries and beam materials. Based on three criteria (mass, volumetry and bending performance) the best tested solutions are selected.

Chapter 6 looks at two different crash events, the side impact collision and the side pole tests, and studies the relationship between an improvement in bending performance computed in Chapter 5 and a real improvement in the crash performance of a complete vehicle model (Geo Metro).

Finally, Chapter 7 sums up the main achievements of the work developed throughout this thesis, and leaves some suggestions for future work on the crash research area.

Chapter 2

Automotive Safety

The rise of the automotive industry during the XX century contributed greatly for the evolution of transportation. Travelling for short distances became easier and faster than ever before. The advent of the combustion engine, combined with the power provided by natural fuels made it possible for engineers to build powerful machines capable of moving increasingly faster. Transport of both people and merchandise was forever revolutionized.

Moving faster, however, soon exposed one of the major concerns of every car manufacturer in the world, automotive safety. When a really fast moving item collides into a very slow or even stopped one, either the first or the second, or even both, suffer significant damage. Whether inside or outside the vehicle, when a person is involved, the crash has proven to be many times fatal. How to significantly decrease road fatalities and crash related injuries is the main motivation of automotive safety. During the last decades, a significant decrease in traffic related fatalities has been recorded not only in countries with a large industrial tradition but also in some new emerging economies [2]. These are usually linked to the development of active (e.g. tires, brakes) and passive (e.g. seatbelt, airbags, vehicle frame) safety systems. The first group, active safety systems, helps to avoid the accident, as the second one tries to contain its possible consequences. Recent data shows that, annually, 1.2 million people still die in automotive accidents and 20-50 million suffer from non-fatal injuries [2]. Even with a decreasing rate of fatal accidents, the emerging economies are mainly responsible for a significant increase in the number of vehicles on the roads, with China, India and Brazil leading this rapid growth. This means that at a constant, or even slowly decreasing fatality rate, the number of automotive related deaths tends to increase. Predictions estimate that, by 2030, ”road accidents will reach fifth place amongst the leading death causes in the world” state Hakkert and Gitelman [2] in their article *Thinking about the history of road safety research: Past achievements and future challenges*. Not only the increasing number of motorized vehicles represents a challenge. As the world population grows, so it does the number of pedestrians on largely populated areas, and as the environmental concern rises, so it does the number of people who opt to replace their traditional transport methods by more sustainable ones, such as cycling or even walking. All these pose intricate challenges to automotive safety, as all efforts should be made in order to avoid vehicle related fatalities.

This chapter is focused on automotive safety, thus some critical areas will be approached in greater depth. First, a brief analysis of passive and active safety systems will be presented. Next, a general look on the existing safety regulations and, finally, a state of the art research on side intrusion beam configurations. As this chapter evolves, its content will be successively more focused in the real motivation of this thesis, developing a side intrusion beam capable of increasing passengers safety in the event of a lateral collision.

Figure 2.1: Side impact test on a Tesla Model S [13]

2.1 Safety Systems

Automotive safety is a complex subject divided into multiple areas. From raising awareness until the airbag deployment, there is a long path in order to favor the first and, at all cost, avoid the need of the last. Here the focus will be on the existing systems, passive or active, which are designed to prevent the accident occurrence (active systems) or to reduce its physical consequences to any human being that may be involved (passive systems). Some of the most important safety systems are presented in Figure 2.2.

2.1.1 Active Systems

If all the preventive methods were totally effective, there would be no need for crash containing measures and passive systems would become redundant. The following list sums up the main active systems as their main functions and characteristics:

- **Brake** – responsible for decelerating the vehicle. It can be activated in movement using a hydraulic pedal or when parked (in order to keep null movement) using the mechanic parking brake;
- **Traction Control System (TCS)** – prevents the vehicle from slipping in low adherence conditions when accelerating. This is an automatic system which is trigerred to prevent car loss of control;
- **Antilock Braking Systems (ABS)** – prevents the wheels from blocking when the driver activates the brake pedal, which allows steering while braking;

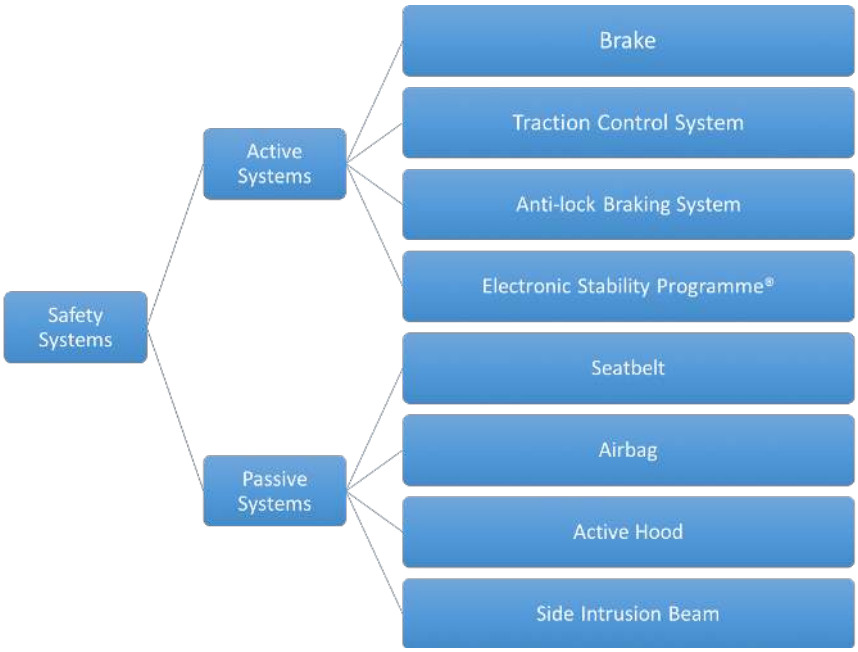

Figure 2.2: Safety systems

- **Electronic Stability Programme (ESP®)** – includes TCS, ABS and additional sensors to improve vehicle stability. The system checks 25 times per second whether the vehicle moving direction is equivalent to the driver steering input [14]. If not, it identifies the critical point causing adherence loss and locally activates the braking system, independently on the driver reaction, to regain vehicle control, within physical limits;

The advent of new and autonomous safety systems will bring to the automotive market safer solutions. However, these improvements tend to replace the driver's role, transforming the driving process into an automatic procedure, raising some questions on either some superficial issues, such as the pleasure withdrawn from the driving experience, or some deeper ones, such as the legal responsibility in case of an accident. An example of a recent advancement is the Autonomous Emergency Braking System (AEB) [15]. The word autonomous refers to the system's independency on the driver input to brake in emergency circumstances.

2.1.2 Passive Systems

Active safety systems are not always totally effective, either it is because all systems can fail, due to poor maintenance, design flaws or other external factors, or because there are unpredictable and unavoidable situations which inevitably lead to an accident. Therefore, designing and integrating a set of passive safety systems becomes crucial. They will be responsible for ensuring minimum damage in the vehicle occupants and in any other human life that may be involved in the collision. Several of the car components are designed as part of a global passive safety system. The following list sums up the main active systems as their main functions and characteristics:

- **Seatbelt** – the most notorious of all the safety systems. Studies show its high effectiveness,

with fatal injury probability decreasing 45% and moderate-to-critical injury decreasing 50% [16]. In Europe, most countries legislated seatbelt usage, making it compulsory, specially in the front seats [17], where passengers are more exposed to frontal impact;

- **Airbag** – its purpose is to slow the passenger movement for a small fraction of time countering the acceleration induced by the crash. There are frontal and lateral airbags, each with their specific characteristics. Lateral airbags, for example, need to become fully inflated in 8 milliseconds, as for frontal airbag this number rises to 50ms [17] . The airbag and seatbelt work together in protecting the passenger. Their coordination is crucial to ensure a higher level of safety, rather than increasing the fatality risk. Airbag malfunctions have caused throughout the years several deaths (in the USA, from 1987 to 2007, 181 frontal airbag related fatalities were registered [18]). However, it is widely recognized that its usage helps preventing more deaths than the ones it provokes (the same document refers 24334 lives were saved in the equivalent period);

- **Pedestrians Passive Safety Systems (PPSS)** – one of the largest concerns regarding RS is related to Vulnerable Road Users (VRUs), which include "pedestrians, bicyclists, two wheelers and other small vehicles" [19], particularly in emerging economies, such as the majority of the African countries where, as whole, 43% of road accident fatalities are connected to VRUs [1]. Even developed and rich cities, such as New York, present high rates of pedestrian fatalities (51% in 2011 [20]). PPSS development is a global challenge being currently addressed by great organizations such as the World Bank or Euro NCAP which test all vehicles for pedestrian impact [21]. There are some technologies in development phase which are intended to decrease the injuries suffered by pedestrians in case of impact. Windshield airbags to prevent head injuries (the most fatal [19]) or an active hood designed with the same purpose, automatically lifted in the collision moment in order to grant a certain flexibility to the impact surface, are two good examples of how it is possible to improve pedestrians safety. For instance, studies show that windshield airbags could decrease head injuries by 90% and upper body injuries by 50% [19];

- **Vehicle External Frame** – the first component responsible for absorbing the impact energy and, therefore, contributing to an increase in passenger safety, is the car's external frame. This structure is composed by many single components which, both individually and as a whole, play a significant role in impact damping. One of those elements is the focus of this thesis, the side intrusion beam. Its ability to enhance passenger safety will be further discussed as a number of comparative simulations will be performed, carefully evaluating the overall result of this beam installation. Figure 2.3 illustrates several components of the vehicle's external frame responsible for reducing the effect of different types of impact (frontal, lateral, roll-over, etc.), where the side intrusion beams are shown in orange.

Figure 2.3: Volvo V40 safety cage [22]

2.2 Safety Standards & Testing Procedures

Concerning automotive lateral safety, each door plays a crucial role in protecting the passengers when a side collision occurs. As a matter of fact, the door is the only component which stands between the passenger and the external object which collides into the car. In a frontal crash most of the vehicle systems rest between the passenger and the collision point. These components, such as the engine, radiator and body frame go through a deformation process which absorbs the crash energy, avoiding its transference and sequent damaging to the passengers. However, frontal crash usually occurs at higher speed, increasing the total amount of crash energy. Both collision types pose different engineering challenges, equally hard to solve and equally important regarding occupants' safety. Since the door is the only protective element in a side impact, its structural strength is a key factor in the design phase. This component must have the ability to absorb or transfer a significant part of the impact energy, having its deformation limits constrained not only by its materials' structural limits, but also by its penetration in the passenger compartment. These limits are defined by safety criteria regarding the acceleration and impact effect on a typical human body. Vehicle homologation in Europe is only possible if a test vehicle successfully goes through a specific procedure created by the United Nations Economic Commission for Europe (UNECE). This entity produces the European regulations for lateral and frontal crash regarding the behavior of multiple car components and its impact on passengers safety, using appropriate dummies during crash trials. The ECE R-95 regulation, created by UNECE, was specifically designed to regulate lateral collision and therefore will be presented next. Furthermore, a succinct description of auxiliary requirements produced by EuroNCAP will be considered.

2.2.1 European Regulation

In this section, a brief description of the homologation testing set will be presented, highlighting the specific parameters required for conducting the computational simulation of a regulated crash test. Further details concerning other non-applicable test procedure specifications (e.g. environment conditions) can be found in the ECE-R95 regulation[23].

Lateral impact is induced by a mobile deformable barrier (MDB) moving at a speed of 50km/h, which collides perpendicularly with the stationary test vehicle. After-impact displacement is allowed. MDB

configuration, which is stated in the regulation, requires a specific rigidity for the impactor. This parameter has an important role in crash analysis since the energy absorbed by MDB deformation will not be transferred to the test vehicle. The main purpose of this simulation is to evaluate the passenger safety during collision. Thus, in order to perform a valid simulation, it is necessary to design appropriate human-like dummies and place them inside the vehicle before crash. The mathematical method to assess the dummy damage is also described in ECE-R95. It allows for specific health assessment based on applied accelerations and displacements during collision. Several criteria are defined based on the location where these accelerations and displacements are imposed: head performance criteria, thorax performance criteria, pelvis performance criteria and abdomen performance criteria. The dummy must be installed in the front seat on the impact side, under all available safety systems (e.g. seatbelt, lateral and frontal airbags).

Conducting a simulation under all the specific regulations described above is, however, out of the scope of this thesis, since full vehicle and MDB models and an approved dummy design would be required. Instead, as it will be further discussed, a simpler global model will be used in order to run a comparative analysis regarding the door's structural performance.

2.2.2 Euro NCAP

Despite fulfilling the previous regulation being enough to achieve vehicle homologation, many other criteria can be found, developed by automotive safety oriented organizations, such as Euro NCAP, which significantly upgrade the structural requirements for the vehicle and consequently the passengers safety. Meeting these standards is important for automotive brands as they increase their vehicle's commercial value.

Euro NCAP was founded in 1997 providing "consumers with a realistic and objective assessment of the safety performance of some of the most popular cars sold in Europe" [24]. Euro NCAP is an independent organization backed by 7 governments (United Kingdom, France, Germany, Netherlands, the Catalonia region of Spain, Luxembourg and Sweden). Apart from their more rigid requirements, Euro NCAP takes another step towards passengers safety, performing collision tests not compulsory according to European regulations. One particular example is the side pole test. This test aims to verify how safe the vehicle is when colliding into pole-like structures, such as trees and signposts, among others. In order to assess occupants safety, a vehicle is crashed against a fixed pole, at a speed of 32km/h in an oblique direction (75^o between the car longitudinal axis and its velocity vector) [25]. In after-test analysis there are several parameters which must be checked. For example, it is required for all doors to open normally as it must be possible to remove the test dummy from the passenger compartment without performing any changes to the vehicle configuration [25]. Euro NCAP presents full descriptions of their testing methods, describing each requirement to the finest detail. More specific information can be found in [13].

(a) Front impact test

(b) Pole impact test

Figure 2.4: Tesla Model S during Euro NCAP's impact tests [13]

2.3 Side Intrusion Beam

A side intrusion beam is a component designed to integrate an automotive door system with the specific purpose of protecting the vehicle passengers in the event of a lateral collision. As the name suggests, it is a beam which connects the main pillars of a car's external frame through the door hinges and the door lock. Introducing this passive safety system is entirely relevant since recent statistics show that lateral impact reaches second as for the number of automotive total accidents, counting one third of total incidents, from which 35% become fatal [3]. The need of better and improved lateral protecting systems is indisputable. Being located precisely in the impact zone, the SIB plays a crucial role in absorbing and transferring the crash energy. Testing and improving both its shape and material, hence its bending performance, is the central focus of this thesis.

2.3.1 Review of Designs

Designing the SIB poses an extremely complex challenge. Its main purpose, damping impact forces by absorbing crash energy, is limited by maximum beam deformation. In other words, it shall "deform hardly while absorbing energy" [4]. Moreover, the SIB is also used to stiffen the door in case of frontal crash, which adds further constraints to the design. However, this specific function will not be considered throughout this thesis as only lateral impact simulations will be performed.

Regarding the beam's shape, multiple designs have been tested and even if it is possible to find many comparative studies [3][4][26], there is not a globally accepted solution as being the most effective in preventing passengers injuries in lateral impact. Some SIB cross section examples can be found in Figure 2.5.

Beam profiles are divided into two large groups: open and close sections. In set 1 of Figure 2.5 a mixed group of close sections, obtained after welding bent thin plates, was tested. When using these type of beams, special attention is required for the welding process used to close the free edges. Yoon et al. [26] state that a "whole-length welding throughout the distance of the pipe provided a maximum reaction force for the newly developed one-body door beam". Standard closed sections were firstly used

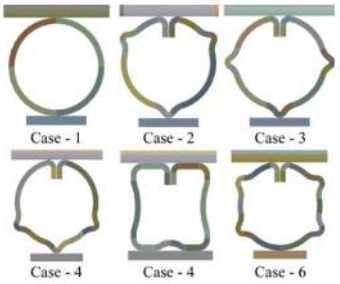

(a) Set 1 [26]

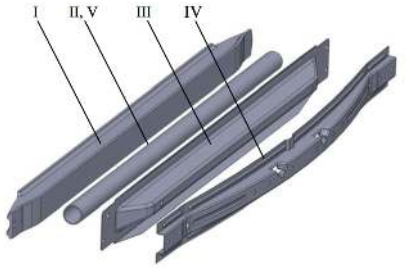

Profile number and cross-section at the center				
1	2	3	4	5
Distance between supports, mm				
955	760	900	740	820

(b) Set 2 [4]

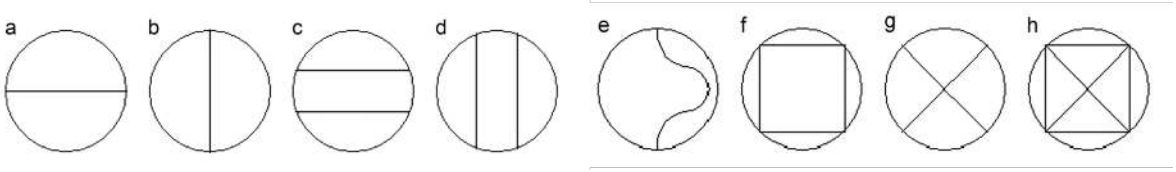

(c) Set 3 [3]

Figure 2.5: SIB profile examples (Adapted from [3][4][26])

with tubular shapes (set 2 of Figure 2.5 – 2 and 5). Stiffness requirements, however, led to the testing of new and more complex shapes which include the addition of internal walls to the traditional tubular closed section (set 3 of Figure 2.5). Open sections usually use ”S” or”C” shapes (set 2 of Figure 2.5 – 3 and 4, respectively) in order to enhance energy absorption. Besides the beam's cross section, its connection to the main frame must also be considered. The SIB may be welded [3] or bolted [4] to the door panel through intermediate components named brackets. These can be manufactured as an extra part (tubular shapes typically), or they can be stamped, for instance, alongside the beam's main cross section[26].

Materials selection is as much of an intricate process as designing its cross-section. Actually, they cannot be done separately since both stiffness and energy absorption depend on either one of them. Nonetheless, when combining structural requirements with materials' properties, it becomes possible to narrow the selection to a shorter list of possible solutions. Steel, aluminum and composites are the three larger groups which comprise the available market solutions. In fact, not only for the SIB, but also for the entire frame of the vehicle [27]. Building affordable vehicles while respecting the crash standards has always been possible with steel. Nevertheless, steel's increased weight comes with an environmental print, as fuel consumption and resulting gas emissions also increase (higher future costs for the consumer). Aluminum and composites are the alternative. The main reason why these materials are not widely used in the industry is linked to their high development and raw material costs. Aluminum is the main competitor of the steel industry. Despite its lower strength, aluminum has a lower density which, globally, turns out in lighter vehicle solutions. Composites are also an alternative due to their low weight/high strength relationship. However, their significant weight reduction comes alongside a major cost increase, being frequently used in higher rate vehicles (e.g. sports cars). Finally, there is a recent

class of materials whose mentioning is entirely relevant. They are a new class of steels, advanced high strength steels, AHSS. Their development arose from the traditional steels' competitive need facing the growth of aluminum usage in the industry. With AHSS, steel producers sought to create a stronger material in order to reduce the volume, hence the vehicle's weight, required to support the desired strengths. Steel producers claim they achieved a reduction in mass that can reach 25% [28]. Even so, new aluminum alloys are also being developed in what is already a tough competition for the market recognition as which is the best material for vehicle manufacturing. In Figure 2.6 the graph shows where each of the described materials stands when it comes to comparing costs with weight reduction.

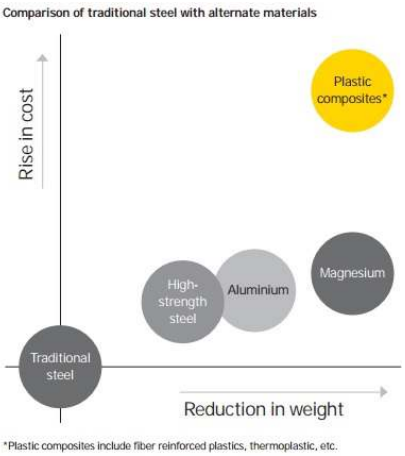

Figure 2.6: Cost Vs weight reduction [29]

2.3.2 Plastic Bending Theory – Mechanical Behaviour of Materials

In this section the plastic bending theory of beams will be shortly presented in a bibliographic review. This mechanism is part of the three-point bending test in which the elastic limits of the material are surpassed. The same process takes place during the side impact of a vehicle, where the SIB is forced to bend under the influence of the force applied by the impactor. Understanding the bending behavior of a beam is then crucial to the development of this thesis.

Review of Elastic Bending

The elastic bending theory of symmetrical beams will be briefly reviewed in this section. Symmetrical bending is observed in beams with single or double symmetric cross-sections [30]. Such geometries are illustrated in Figure 2.7. Hooke's Law is an important equation, which governs the elastic behavior of a material, and it is given by

$$\sigma = E\varepsilon \tag{2.1}$$

where σ is the applied stress, E is the modulus of elasticity and ε is the elastic strain

Let us assume the bending of a beam caused by a pure bending moment, M (see Figure 2.8). This moment will induce two different responses. The upper part of the beam will be under compressive forces, which increase towards the upper edge. The lower part will be under tensile forces which also

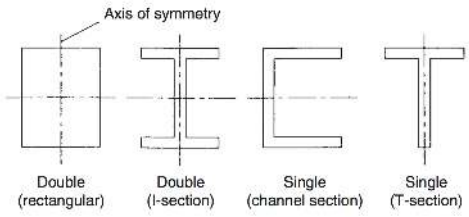

Figure 2.7: Single and double symmetric geometries [30]

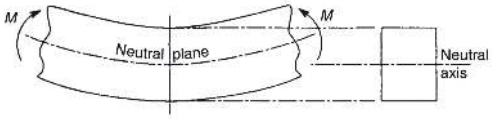

Figure 2.8: Pure bending moment [30]

increase towards the lower edge. Separating these two areas, there is a plane which extends through the entire beam where no compressive or tensile forces are applied. This is the neutral plane. The intersection of the neutral plane with the cross section at any point of the beam forms a neutral axis. This is showed in Figure 2.8. Assuming a linear elastic behavior for the material (equation (2.1)) and that the plane cross-sections of the beam remain plane and normal to the longitudinal fibers of the beam after bending, equation (2.2) can be derived,

$$\sigma = \frac{My}{I} \tag{2.2}$$

where σ is the applied normal stress, I is the second moment of area about the neutral axis and y the distance from the neutral axis. Equation (2.2) describes the stress distribution of a beam under a pure bending moment, i.e., with no applied axial load, which means that this equation also covers the bending cases where a single vertical load, perpendicular to the beam's axial direction, is applied (which is the case of a three-point bending test). It relates the normal stress exerted on the cross section with its distance from the neutral axis. The greater the distance, the higher the applied stresses are. This relationship is particularly useful when the beam must be kept in the elastic boundaries of the material. Knowing the section's geometry, both the greater value of y and the second moment of area I can be calculated, giving the maximum operational moment which can be applied on the beam before the yield stress, σ_y of the material is reached. Further detail on the elastic behavior of beams can be found in [30]. The three-point bending tests conducted in this study extend the material far beyond the yield point, and despite some regions never surpassing the elastic limit, the ruling phenomena of the bending process will be carried in an elasto-plastic, or fully plastic state.

Plasticity Models

Once surpassed the yield point, the deformation of the material starts becoming permanent or plastic. Each material has a different plastic behavior, and metals in particular, are highly ductile which mean they can sustain large plastic deformations. In a plastic state, stresses and strains are no longer proportional, hence Hooke's Law (2.1) cannot be applied. Further models are required to describe the plastic behavior of the material. These models will be presented next.

The first and simplest one is the elastic, perfectly plastic relationship [31]. This model predicts a linear elastic behavior according to Hooke's Law (2.1) until the yield point and then a perfectly plastic behavior, i.e., beyond the yield point the applied stress remains constant whichever the strain applied to

the material.

$$\begin{aligned} \sigma &= E\varepsilon \quad (\sigma \leq \sigma_0) \\ \sigma &= \sigma_0 \quad \left(\varepsilon \geq \frac{\sigma_0}{E}\right) \end{aligned} \tag{2.3}$$

where σ_0 is the yield stress. As mentioned before, this is the simplest formulation for the plastic behavior of a material. It is a reasonable approximation for the initial yielding deformation of some metals and is commonly used to perform initial estimations on materials which have a more complex behavior. Beyond the yielding point, the total strain is computed as the sum of its two components: elastic and plastic.

$$\varepsilon = \varepsilon_e + \varepsilon_p = \frac{\sigma_0}{E} + \varepsilon_p \quad \left(\varepsilon \geq \frac{\sigma_0}{E}\right) \tag{2.4}$$

The second model is the elastic, linear-hardening relationship [31]. This model gives a rough estimation for the behaviour of materials which go under significant hardening beyond the yielding point, i.e., whose stress-strain curves rise when plastic deformation begins, when compared to the perfectly plastic behavior. The hardening model is still very simple, considering a linear relationship between stress and strain, similar to Hooke's Law. A new dimensionless variable, $0 < \delta < 1$, is introduced to translate the slope of the plastic section of the curve as a fraction of the elastic modulus, δE, given by any two points beyond the yielding point.

$$\delta E = \frac{\sigma - \sigma_0}{\varepsilon - \varepsilon_0} \tag{2.5}$$

Knowing that $\sigma_0 = E\varepsilon_0$, the elastic, linear-hardening model can be described by the system (2.6)

$$\begin{aligned} \sigma &= E\varepsilon \quad (\sigma \leq \sigma_0) \\ \sigma &= (1-\delta)\sigma_0 + \delta E\varepsilon \quad (\sigma \geq \sigma_0) \end{aligned} \tag{2.6}$$

Rearranging the second equation, the global strain beyond the yield point is given by equation (2.7).

$$\varepsilon = \frac{\sigma_0}{E} + \frac{(\sigma - \sigma_0)}{\delta E} \quad (\sigma \geq \sigma_0) \tag{2.7}$$

This model can be expanded to a more complex linear description of the bending behaviour. Considering different slopes $\delta_i, \quad i = 1, 2, 3, ...$, the plastic section of the stress-strain curve can be linearly approximated to the material's actual response.

The third model is the elastic, power-hardening relationship [31]. This is a more complex model that predicts a proportional relationship between stress and strain raised to a power, beyond the yield point.

$$\begin{aligned} \sigma &= E\varepsilon \quad (\sigma \leq \sigma_0) \\ \sigma &= H_1\varepsilon^{n_1} \quad (\sigma \geq \sigma_0) \end{aligned} \tag{2.8}$$

where H_1 and n_1 are constants which depend on the tested material. The constant n_1 is called the strain hardening exponent. In order to calculate these two constants, the stress-strain curve should be plotted in a logarithmic scale. Applying the log function to both sides of the second equation of the

system (2.8) results,

$$\log(\sigma) = \log(H_1) + n_1 \log(\varepsilon) \tag{2.9}$$

which is represented by a linear relationship where n_1 is the slope of the straight line and H_1 is the value of σ when $\varepsilon = 1$. Once again rearranging the second equation of the system (2.8), the plastic strain is easily computed.

$$\varepsilon = \left(\frac{\sigma}{H_1}\right)^{\frac{1}{n_1}} \quad (\sigma \geq \sigma_0) \tag{2.10}$$

The final model presented in this section is the Ramberg-Osgood relationship [31], which is a variation from the power-hardening relationship. An exponential relation is used, but in this model, it is applied to the plastic strain, and not to the total strain as in the previous model.

$$\sigma = H\varepsilon_p^n \tag{2.11}$$

where n is also called strain hardening exponent. Total strain is computed by adding both elastic and plastic components.

$$\varepsilon = \varepsilon_e + \varepsilon_p = \frac{\sigma}{E} + \varepsilon_p = \frac{\sigma}{E} + \left(\frac{\sigma}{H}\right)^{\frac{1}{n}} \tag{2.12}$$

Equation (2.12) cannot be solved explicitly, but numerically it provides a smooth continuous curve which describes both elastic and plastic deformations with no distinct yield point. The fitting method is similar to the power-hardening method where the stress-strain curve is plotted in a logarithmic scale. These two methods are practically equivalent when the plastic portion of the curves dominates to the point where the elastic deformation can be considered negligible. The Ramber-Osgood relationship has the advantage that it can accurately represent the stress-strain curves of many materials.

These are the main models used to describe the plasticity of a material. Next, the beam's elasto-plastic bending behavior is studied in greater depth.

Plastic Bending Analysis by Integration

This thesis will only approach the study of symmetrical geometries, hence this section will consider the plastic bending theory of symmetrical cross-sections alone. An assumption already considered in the study of elastic bending, is that shear stresses are negligible during plastic deformation [31], which implies that originally plane cross-sections remain plane during deformation. This leads to a linear strain variation with distance to the neutral axis.

$$\frac{\varepsilon}{y} = \frac{\varepsilon_c}{c} \tag{2.13}$$

where ε_c is the value of ε at $y = c$ (see Figure 2.9). Due to this linear relationship, the stress distribution in the cross-section is identical to the stress-strain curve until the point $\varepsilon = \varepsilon_c$. Considering now that the sum of all the axial forces must be null in a pure bending scenario, results

$$P = \int_{-c_2}^{c_1} \sigma t \, \mathrm{d}y = 0 \tag{2.14}$$

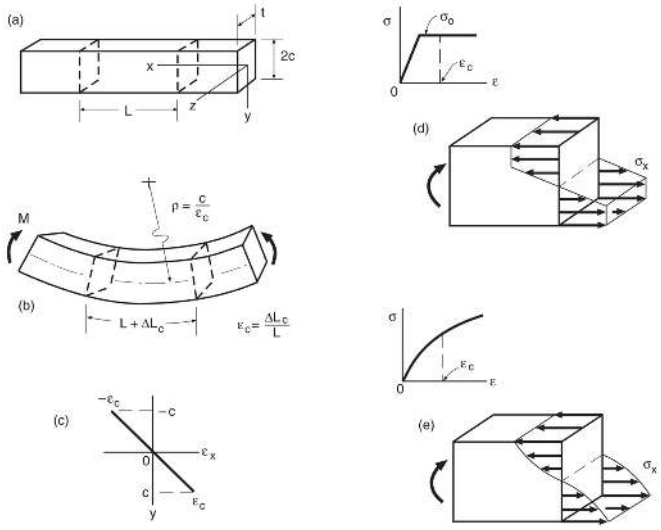

Figure 2.9: A rectangular beam subjected to pure bending which causes yielding [31]

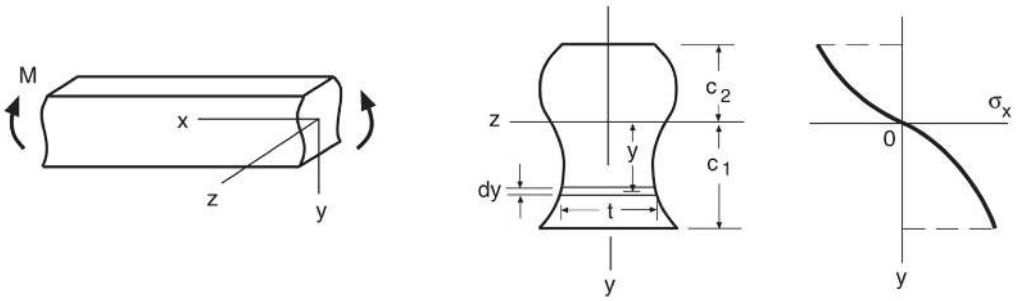

Figure 2.10: Area element ($t\,\mathrm{d}y$) and stress distribution needed for integration to relate bending moment M to stresses and strains [31]

The moment equation for a given symmetrical section (Figure 2.10) is given by

$$M = \int_{-c_2}^{c_1} \sigma t y \,\mathrm{d}y \tag{2.15}$$

Combining equations (2.13),(2.14) and (2.15) with stress-strain function, the moment value may be computed for specific scenarios, such as the plastic collapse load, when gross plastic deformation is reached.

Rectangular Shaped Beams

Considering the rectangular cross-section of a beam (see Figure 2.9), with double symmetry (y and z axes), whose material has an also symmetric stress-strain curve (identical for tension and compression), it is clear that $c_1 = c_2 = c$ and that the neutral axis remains at the centroid [30]. Due to symmetry, the moment can be calculated for half of the cross-section and then its value doubled for the entire area. Simplifying equation (2.15), results

$$M = 2t \int_0^c \sigma y \,\mathrm{d}y \tag{2.16}$$

Considering a power-hardening relationship for the stress-strain curve, neglecting the initial elastic region,

$$\varepsilon = f(\sigma) = \left(\frac{\sigma}{H_1}\right)^{\frac{1}{n_1}} \tag{2.17}$$

Solving for σ,

$$\sigma = H_1 \left(\frac{y\varepsilon_c}{c}\right)^{n_1} \tag{2.18}$$

Integrating equation (2.16),

$$M = \frac{2tc^2 H_1 \varepsilon_c^{n_1}}{n_1 + 2} = \frac{2tc^2 \sigma_c}{n_1 + 2} \tag{2.19}$$

where the second form is given by applying equation (2.18) with $\varepsilon = \varepsilon_c$, $\sigma = \sigma_c$ and $y = c$.

Discontinuous Stress-Strain Curves

Equation (2.17) allows a simple integration process. However, three of the plasticity models presented in this chapter have a purely elastic region separated from the plastic region by a discontinuity located at the yield point. Hence, in the same cross-section there will be two different regions. The region closer to the neutral axis (less deformed) will be under elastic bending and the region beyond the elasto-plastic boundary will be under plastic bending. Such models can be integrated under equation (2.16) but they require two steps. Assuming that yielding begins at a y_0 distance from the neutral axis, equation (2.17) is then split into

$$M = 2t\left[\int_0^{y_0} \sigma y \,\mathrm{d}y + \int_{y_0}^{c} \sigma y \,\mathrm{d}y\right] \tag{2.20}$$

Using equation (2.13) $\varepsilon = \varepsilon_0$ and $y = y_0$ and noting that Hooke's Law can be applied to the yield stress and strain ($\sigma_0 = E\varepsilon_0$), results

$$y_0 = \frac{\sigma_0 c}{E\varepsilon_c} \tag{2.21}$$

Let us consider first the elastic region, where Hooke's Law is valid. Equation (2.13) can be re-written into

$$\frac{\varepsilon}{y} = \frac{\sigma/E}{y} = \frac{\varepsilon_0}{y_0} \tag{2.22}$$

Solving for σ,

$$\sigma = \frac{E\varepsilon_0 y}{y_0} \quad (0 \leq y \leq y_0) \tag{2.23}$$

The plastic region can be described according to different models, but for simplicity reasons the elastic, perfect plastic model will be selected. Beyond $y = y_0$ the stress is given by,

$$\sigma = \sigma_0 \quad (y_0 \leq y \leq c) \tag{2.24}$$

Substituting equations (2.23) and (2.24) in the first and second terms of equation (2.20) respectively,

and using equation (2.22) to eliminate y_0 from the equation, and after some manipulation, the result is

$$M = tc^2\sigma_0 \left[1 - \frac{1}{3}\left(\frac{\sigma_0}{E\varepsilon_c}\right)^2\right] \quad (\varepsilon_c \geq \sigma_0/E) \tag{2.25}$$

This is a general solution which computes the bending moment, provided that plastic deformation occurs. In a limit situation, where only the edge of the beam is in plastic deformation, $\varepsilon_c = \sigma_0/E$, which leads to the initial yielding moment

$$M_e = \frac{2tc^2\sigma_0}{3} \tag{2.26}$$

which is equivalent to the elastic solution (see [31]). The opposite limit, with large values of strain ($\varepsilon_c \gg \sigma_0/E$), approaches the fully plastic moment, M_p.

$$M_p = tc^2\sigma_0 \tag{2.27}$$

As M_p is approached, large deformations are imposed, and the development of plastic hinges occurs. In this scenario the elastic region $y \leq y_0$ tends to zero. Figure 2.11 illustrates de development of plastic hinges of a rectangular beam in a three-point bending test and Figure 2.12 shows the moment vs. strain behavior of the same beam, exhibiting the stress distribution for various strain ratios. Further detail on the plastic behavior of beams can be found in [31].

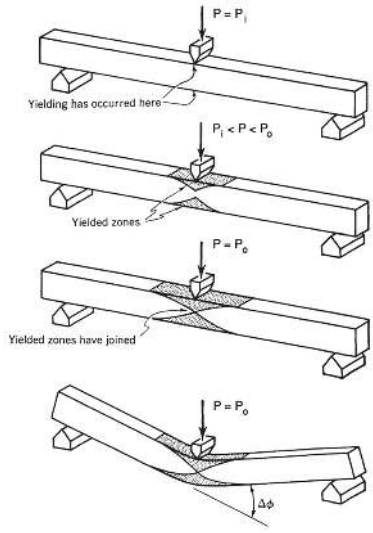

Figure 2.11: Development of a plastic hinge in three-point bending test [31]

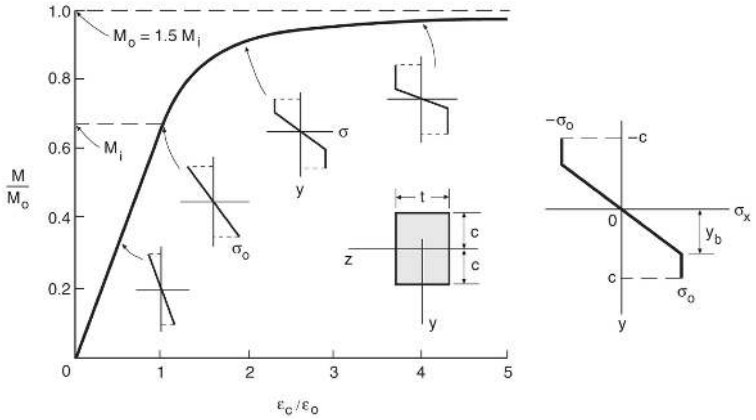

Figure 2.12: Moment vs. strain behavior for a rectangular beam of an elastic, perfectly plastic material [31]

2.3.3 Requirements and Performance Metrics

Bending performance can be measured in many different ways. However, a particular set of parameters (or part of it) has been frequently used in past work in this area [6][9][26], proving itself to be a good tool to study and compare different beams. Note that herein the z axis is considered as the load direction.

This set comprises four different parameters:

- *Energy absorption (EA)* – during a bending test, the applied force is recorded and matched with the imposed displacement. The resulting curve not only shows the magnitude of the exerted force throughout the bending process, but also enables further calculations which lead to the energy absorbed by the beam during its deformation.

$$EA = \int_0^{\delta} F(z)dz, \tag{2.28}$$

  where δ is the imposed displacement and F is the applied force in the z direction.

- *Specific energy absorption (SEA)* – energy absorbed per unit mass

$$SEA = \frac{EA}{M}, \tag{2.29}$$

  where M is the beam's mass.

- *Maximum crash force (F_{max})* – the maximum recorde value of the force/displacement curve

$$F_{max} = \max(F_z) \tag{2.30}$$

- *Crash force efficiency (CFE)* – ratio between the average applied force and F_{max}

$$CFE = \frac{F_{avg}}{F_{max}}, \tag{2.31}$$

  where F_{avg} is the average crash force which can be expressed as function of the energy absorption parameter and the total displacement,

$$F_{avg} = \frac{EA}{\delta}, \tag{2.32}$$

These parameters combined can be used to perform a comparative analysis on several different beams, working as tool to uncover which geometries and materials have the best bending behavior. This is a comprehensive set which measures force, energy and even an dimensionless figure, the CFE, which transmits the abruptness of the beam bending behavior. A CFE value close to 1 shows a beam which deforms steadily requiring almost the same force during the whole bending process, as a CFE close to 0 is representative of a high initial peak force followed by a significant decrease in the beam's ability to sustain the imposed displacement, hence its ability to absorb the crash energy. EA is an important parameter to rapidly understand which beam better responds to the impact. It does not, however, take the beam's mass into account. As the weight is a very significant factor in the automotive industry, in order to understand which beam has the best behavior, the SEA is also a very important parameter since it shows, per kg (mass), which beam absorbs the most energy.

Chapter 3

Approach & Methods

This chapter sets the basis for the work developed throughout this thesis. First, the approach to the general problem is described, highlighting the logical path which guided this work. Then the computational tools which support the work developed in this thesis are introduced, first the CAD software where the beams were designed and finally the Finite Element tools responsible for the structural analysis of the beam and for the crash simulation.

3.1 Problem Approach

The development of the side intrusion beam will be conducted using a powerful FEA tool, HyperWorks. A complete model of a Geo Metro (this vehicle's dimensions and configuration will be approached later) is used as test basis, since its dimensions are close to the Be's initial projected packaging. However, simulating a crash event with a full vehicle has proven to be time expensive thus, in order to perform an extensive study on several geometries and materials, a simpler and faster model is required. For that reason, a three-point bending model was designed with the intent of assessing the beam's bending performance in a simple low cost simulation. In fact, for side impact, the thin-walled beams will collapse in bending mode [9] which lays a common ground between a complete vehicle side crash simulation and a simple three-point bending test. This model will first be validated through experimental testing. Then, different geometries and materials will be tested using the same simulation and performance results will be compared. Concerning material selection, a wide variety of metals will be applied. The combination of high strength with high ductility makes the metal materials a logic option to a scenario where large deformations are expected. Steel is the most commonly used material, industry wise, but other metals are also tested considering, for example, the search for weight reduction alternative solutions. Selecting the best configuration is a process which depends on the project main requirements, such as bending performance, mass or even the available room inside the door. For that reason, a selection tool is designed to evaluate the tested solutions in different scenarios where the weight of each requirement in the overall assessment of a certain configuration is variable. Finally, the best configurations are installed and tested in a complete vehicle crash simulation and conclusions are withdrawn regarding the side

intrusion beam's overall impact in a side collision. The approach followed in this thesis is summarized in Figure 3.1.

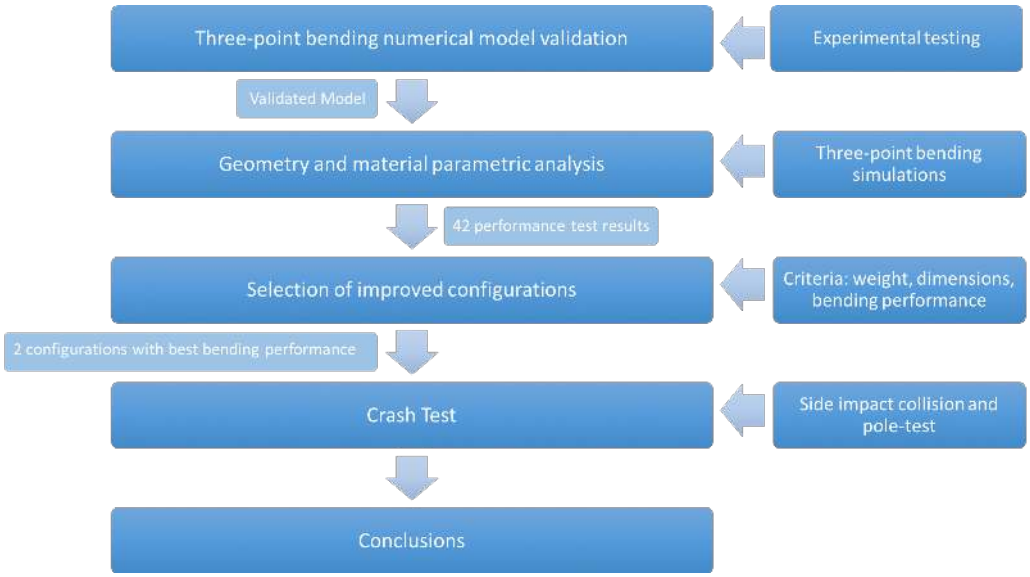

Figure 3.1: Problem approach

3.2 3D Modeling – CATIA

Designing a 3D model for each of the setup components is the first step. CATIA v5 r20 was selected for that purpose. This software has in-built tools for surface creation which, combined with an appealing and intuitive user interface, potentiate a simple, fast and clean designing process. A simple three-point bending simulation only requires three different components: impactor, supports and the beam itself, all of which have a simple design and can be modeled in two basic steps: wireframe design of the intended part's profile followed by surface extrusion with the intended part's length.

The option for a pure surface design is justified by the study of thin-walled configurations. Otherwise, solid bodies would have to be designed in CATIA through a algorithm very similar to the one described above. In a three-point bending test, the beam is simply rested on the supports and for that reason the profile can be extruded with no shape variations at its endings. Each part is exported in a ".stp" format so that it can be read by HyperWorks.

3.3 Finite Element Analysis – HyperWorks

HyperWorks is a comprehensive simulation tool developed by Altair which includes linear and nonlinear analyses, structural and system-level optimization, fluid and multi-body dynamics simulation, electro-magnetic compatibility (EMC), multiphysics analysis, model-based development, and data management solutions. It is used in several industries, such as the automotive, aerospace, biomedical, energy, rail, among others. HyperWorks was built to assist engineers in each step of the product development cycle, from the early stages of conceptual design until the final manufacturing process.

HyperWorks comprises an extensive tool set, providing engineering solutions to a great number of challenges regarding automotive design. The explicit non-linear finite element code RADIOSS [32] was used to develop the numerical models. Figure 3.2 illustrates the solutions used from this point forward. All the following tools are part of HyperWorks V13.0 package licensed by CEIIA, where the core research for this thesis was developed.

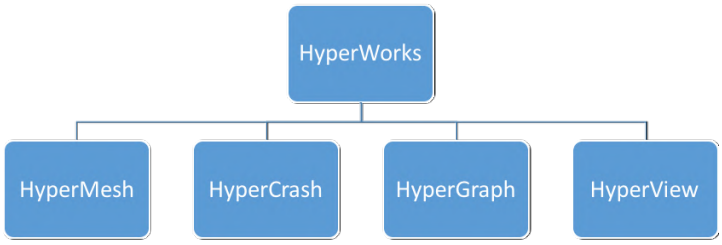

Figure 3.2: HyperWorks tools

3.3.1 HyperMesh

HyperMesh is the preferred pre-processing tool to apply a finite element mesh to the resulting surfaces from the design phase. Once imported all the parts which compose the setup, HyperMesh supplies the tools to move each part to its rightful position. A 2D finite elements mesh will be generated and applied throughout the surfaces. As in a three-point bending test only simple geometries are used, with a constant normal section throughout the entire beam, the meshing process is automatic, requiring user input for mesh type and refinement alone. Despite HyperMesh's capacities extending far beyond the meshing process, that is the only task which is required from this tool inside the scope of this thesis. A simple rectangular beam design in CATIA and meshed in HyperMesh is illustrated in Figure 3.3.

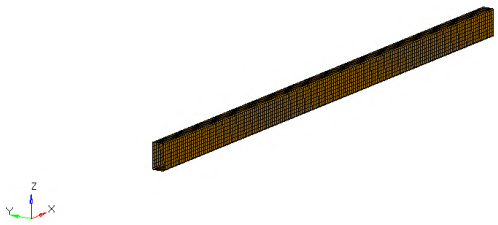

Figure 3.3: Sample beam after meshing process in HyperMesh

3.3.2 HyperCrash

HyperCrash is the engine responsible for most of the pre-processing features required to properly setup a crash simulation. Materials, properties, boundary conditions, contacts, imposed velocities, minimum time step, run time, all these are defined in HyperCrash. A three-point bending "quasi-static" simulation setup can also be configured in HyperCrash. This will be described in greater detail in Chapter 4. For

now, a general description of HyperCrash's general working logic is presented, applied to a three-point bending configuration.

Materials & Properties

After importing a meshed setup from HyperMesh, the first required step is to assign to each surface a property and a material. The material is responsible for the part's mechanical properties, as the property specifies surface thickness and other finite elements parameters such as the integration method. RADIOSS allows multiple definitions of the same material according to different theoretical formulations. One example is the material law MAT 36 – Elastic Plastic Piecewise Linear Material which "models an isotropic elasto-plastic material using user-defined functions for the work-hardening portion of the stress-strain curve (i.e. plastic strain vs stress) for different strain rates" [32], which is equivalent to the elastic, linear-hardening relationship described in section 2.3.2. Regarding properties assignment, when dealing with surfaces, a SHELL property must be selected in order to instruct RADIOSS to compute the simulation considering two-dimensional finite elements. Once the property is assigned, the element formulation must be specified. By default, a Belytscko-Tsay formulation (see [32]) is selected with one integration point (reduced integration). This is, computationally, the lightest and less accurate formulation available but, nevertheless, often produces satisfactory results.

Rigid Bodies

A rigid body is defined as a master node in the workspace connected to a particular set of slave nodes from the original mesh. HyperWorks constantly works with the terms master and slave when referring to nodes from different parts that are somehow connected. Many times this distinction is redundant as master and slave nodes play the same role in whichever connection they may have. However, in other cases, such as the rigid bodies, some properties may be defined directly towards the master or the slave nodes. Rigid bodies have a purely rigid behaviour (hence their designation) and are located by default in the slave system's centre of gravity (COG). All the constraints imposed to the rigid bodies are transmitted to its associated nodes. In a three-point bending impact test, creating two rigid bodies is the most adequate, one connected to the impactor and other to the supports (Figure 3.4).

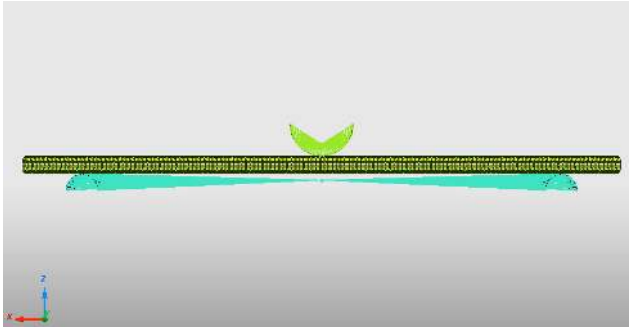

Figure 3.4: Rigid bodies

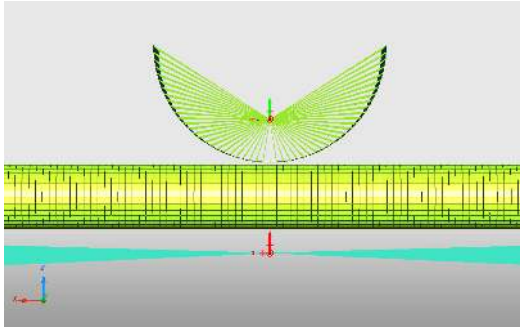

Figure 3.5: Boundary conditions

Boundary Conditions

A key step in pre-processing the model is the creation of the necessary boundary conditions. When performing a three-point bending test, the beam is left free to react to the impact. The remaining components however, are highly constrained. The supports are totally fixed, which means all their six degrees of freedom are locked. In order to apply this boundary condition, only the supports rigid body's master node has to be selected. The impactor's boundary condition differs from the supports because, otherwise, there would be no impact. Thus its degree of freedom related with translation in the z direction (see Figure 3.5) must be free. Although the impactor speed is also a boundary condition, due to its specificity, HyperCrash provides a special command, Imposed Velocity, which provides the necessary tools to apply a time function throughout the simulation. In a quasi-static test, impact speed will be constant. The imposed velocity is applied to the impactor's rigid body. The velocity vector's direction is along the z axis pointing in the negative direction (Figure 3.6). A simple imposed velocity applied on half of a circular beam is illustrated in Figure 3.6.

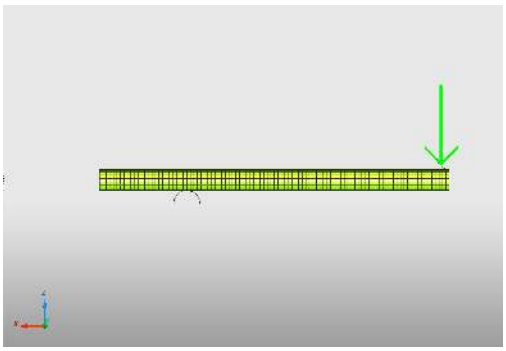

Figure 3.6: Imposed velocity vector applied on half of a symmetric system

Contact Interface

Creating contacts between the several surfaces which compose the studied model is critical in order to enable RADIOSS recognition of existent interfaces and their physical relationships (e.g. friction). HyperCrash provides a command named Contact Interface which is used to create or edit contacts between surfaces. There are numerous contact models available in RADIOSS. TYPE 7, for instance, is a multi-purposed surface oriented formulation. Within TYPE 7, some parameters must be defined to ensure a proper interface behaviour: friction, minimum gap for impact activity, contact stiffness and others. Contact definition is a central step when setting up a simulation since the system output is very sensible to a poor construction of the interface. In case of very small but unpredicted surface penetrations, the solution has proven to drastically diverge from the expected results.

Control Cards

Control cards are tools provided by RADIOSS to command the simulation process, to predict possible setbacks and to ensure the appropriate output results. It is possible to highly customize control cards

in order to improve the simulation's performance. Solution convergence may depend on key factors controlled by these elements (e.g. simulation time step). For a three-point bending setup, the following parameters must be specified: final run time, t_{run}; frequency for writing the animation files (for HyperView), T_{freq}; frequency for writing the history file (for HyperGraph), T_{freq}; minimum time step, Δt_{min}. Once all control cards are defined, the model is ready to be exported in a ".rad" format into HyperWorks Solver Run Manager. RADIOSS will then simulate the three-point bending impact test and generate a set of output files. Two of these files (.h3d and T01) are particularly important as they enable a graphical visualization of the obtained results. Further detail on post-processing will be presented in the following sections.

3.3.3 HyperGraph

HyperGraph imports the T01 file which contains the time history recorded data. When a time history is created, it is associated to a node or a group of nodes, and automatically a list of output parameters is recorded during the simulation (velocities, displacements, moments, among others). HyperGraph 2D is then able to plot any combination of these parameters. For example, in order to validate the three-point bending model, a comparison will be made between the force/displacement (z direction) curve of the impactor of an experimental test with the time history output from the master node of the impactor's rigid body in the computational model. Despite the created time histories, the T01 file also contains a set of global variables which are recorde by default, such as kinetic and internal energy, mass, time, hourglass energy, and more. These variables are important to test the validity of the results.

3.3.4 HyperView

HyperView reads the ".h3d" file which is automatically generated during the simulation. With HyperView it is possible to visualize the animation of the entire simulation and simultaneously observe the evolution of some physical quantities distribution throughout the tested components. These are specified during the pre-processing phase and may include von Mises stresses or the strain energy. A colorful distribution followed by a scale will indicate which values of a specific parameter are recorded in each time frame. Figure 3.7 illustrates the displacement distribution of a side pole test in HyperView.

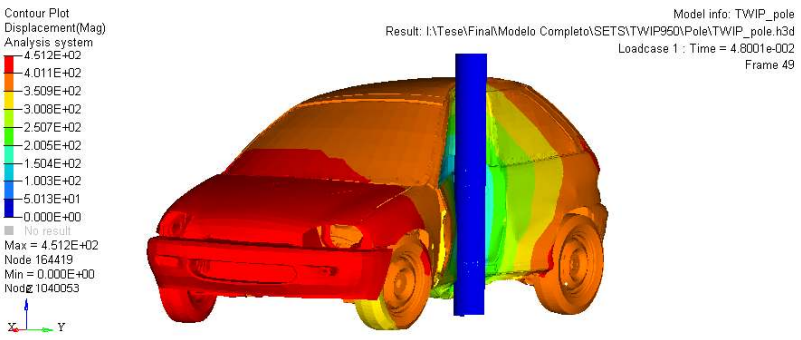

Figure 3.7: Displacement distribution of a pole impact test in HyperView

Chapter 4

Numerical Model Validation

This chapter's goal is to build and validate a numerical model for two bending test configurations, the three-point bending test and the four-point bending test. Only the first will be later used to evaluate the bending performance of the beam, but by validating the numerical model for both configurations, a more robust solution will be obtained. As this thesis focuses on the study of thin-walled structures, several thin-walled beams with variable geometry and thickness will be experimentally tested under three and four-point bending procedures. Then, a tensile test is conducted on material samples to record their stress-strain curves. This information is required to computationally characterize the material's plastic behavior. Finally, equivalent numerical bending models are built in HyperWorks and the simulation results are compared with the experimental data. Once validated the model, it will be used in the next chapter as tool to evaluate the thin-walled beams bending performance.

4.1 Experimental Bending Test

The first step towards model validation is the preparation of an equivalent experimental setup. Two different bending configurations will be tested, in three and in four points. Due to the unavailability of specific norms concerning these bending tests applied to thin-walled beams, a singular procedure will be built based on standard E 855–90 [33] which was designed for studying the bending strength of metallic strips or sheets.

4.1.1 Experimental Procedure

A 250kN MTS 661 High Capacity Force Transducer machine was used to perform the bending tests. The three-point bending impact test has a simple procedure, hence being frequently used to evaluate a beam's bending performance. A long beam (length, L) is placed over two identical cylindrical supports (diameter, D). A large span (S) separates both the supports. A cylindrical impactor (diameter, D) pushes the beam downward in its central point at a very small constant speed (v) since this is a quasi-static test. The test ends if one of two conditions are met: either a target displacement (δ_{max}) is reached and the machine stops advancing or, prior to that moment, the structure fails and the machine, detecting the

abrupt decrease in the applied force, autonomously finishes the test. The four-point bending test is very similar to the three-point bending but instead of having one central impactor, there are two symmetrically displaced impactors which push the beam at the same velocity Both the supports and impactor's material have a much greater rigidity than the beam's. Both tests configuration are illustrated in Figure 4.1.

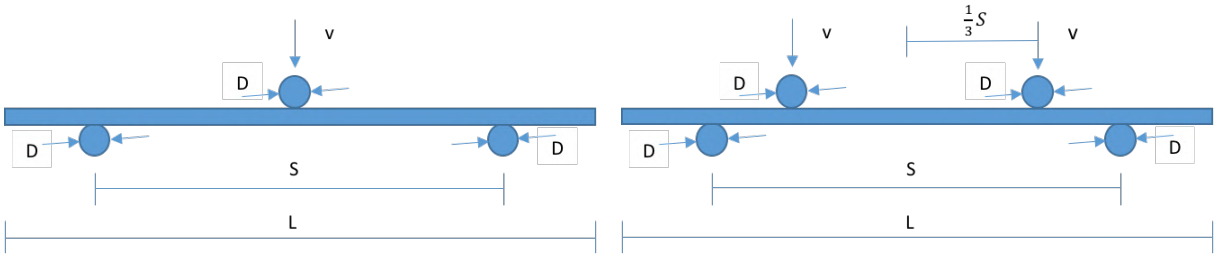

(a) Three-point bending setup

(b) Four-point bending setup

Figure 4.1: Experimental setup

	D/mm	S/mm	L/mm	$v/(mm/s)$	δ_{max}/mm
Three-point bending	30	600	800	0.2	50
Four-point bending	30	300	400	0.2	30

Table 4.1: Bending tests configuration data

Table 4.1 details the specific metrics used during the experimental procedure. This validation process intends to generate a robust model, hence the testing of two bending configurations. Moreover, three different geometries (circular, quadrangular and rectangular) are tested under the same procedure to test wether the numerical model can adapt to different beam behaviors. These are shown in Figure 4.2. Table 4.2 specifies the validation geometries dimensions. For the circular and quadrangular shapes, the the bending behavior of the beam is independent on the loading direction (z or y) since both axes cut the section in identical parts. The rectangular shape bending pattern, however, depends on the axis (z or y) chosen as the force vector, thus it will be tested with both loading configurations. All beams have the same material, a S235 steel.

The bending test laboratory procedure can be described by a short algorithm (from three to four-point bending, the only variation is the number of impactors and their position, according to Figure 4.1):

1. The supports and the impactors are fixed in the desired position;

2. The beam is centered over the supports;

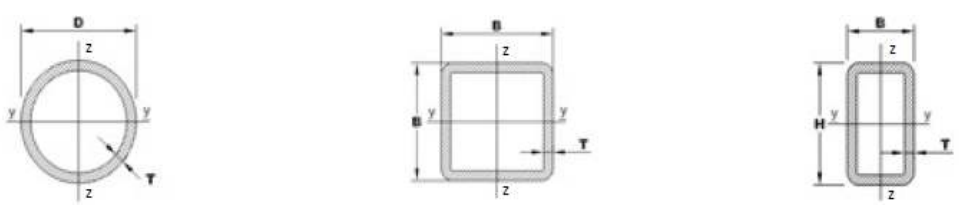

Figure 4.2: Tested geometries during validation tests

Dimension	Circle	Square	Rectangle
T (mm)	2.6	2	2
D (mm)	42.4	–	–
B (mm)	–	40	20
H (mm)	–	–	40

Table 4.2: Dimensions of validation geometries

3. The impactor is lowered until it slightly contacts the beam. This step must be performed carefully to avoid a pre-loading state due to an excessive lowering of the impactor;

4. Test begins with a constant downward speed of the impactor of $0.2mm/s$. This small velocity is selected to ensure procedure safety.

5. Once δ_{max} is reached the test stops. In both configurations this value was defined by the setup limitations;

6. The impactor returns to its original position, the bended beam can be retrieved and the procedure repeated.

To ensure the quality of the test results, each geometry was tested three times for each bending configuration. The rectangular beam was tested six times for three-point bending and six times for four-point bending considering different results were expected for the two different load scenarios. In total, 24 bending tests were conducted. Figure 4.3 illustrates both types of experimental procedure.

(a) Three-point bending experimental test

(b) Four-point bending experimental test

Figure 4.3: Experimental testing

4.1.2 Results & Discussion

Figures 4.4 and 4.5 show the force/displacement curves for each geometry under the three-point and four-point bending tests respectively. Globally, the three trials conducted for each setup can be considered sufficient as the curves in each graph are very precise. In the three-point bending test, the only case where the curves do not totally overlap is in the circular beam test, which has the $C3$ curve slightly

under the remaining two. This is an expected behavior from a pre-loaded beam. When an initial stress is applied, some elastic deformation occurs before the test begins. When finally the test is performed this initial load is artificially set to zero, although the applied deformation remains. This will ultimately result in curve with a smaller peak force but with the same bending pattern. Another way to explain it, would be by saying that the initial loading state induces a negative offset of the force/displacement curve. This small error occurred in the circular beam since, due to its round shape, a greater concern existed regarding the beam's fixation prior to the beginning of the test. With the exception of the four-point bending rectangular beam loaded in the y direction, which shows some instability on the end part of the output curve, all the remaining tests' trials completely overlap, leading to a strong confidence on the presented results. Figure 4.3 shows two pictures taken during the experimental procedure and illustrates both test configurations.

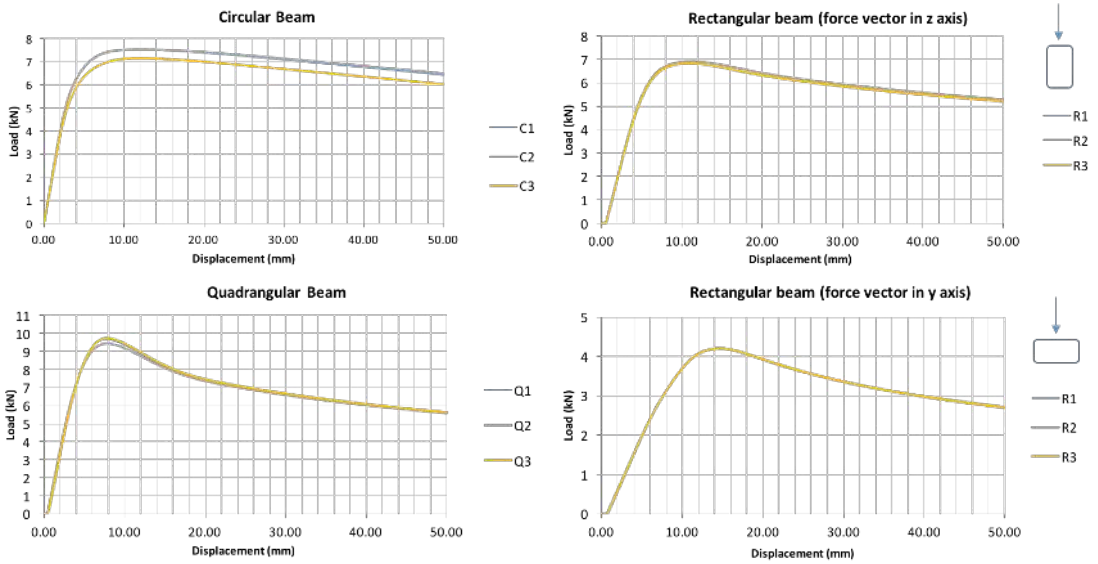

Figure 4.4: Three-point bending experimental results

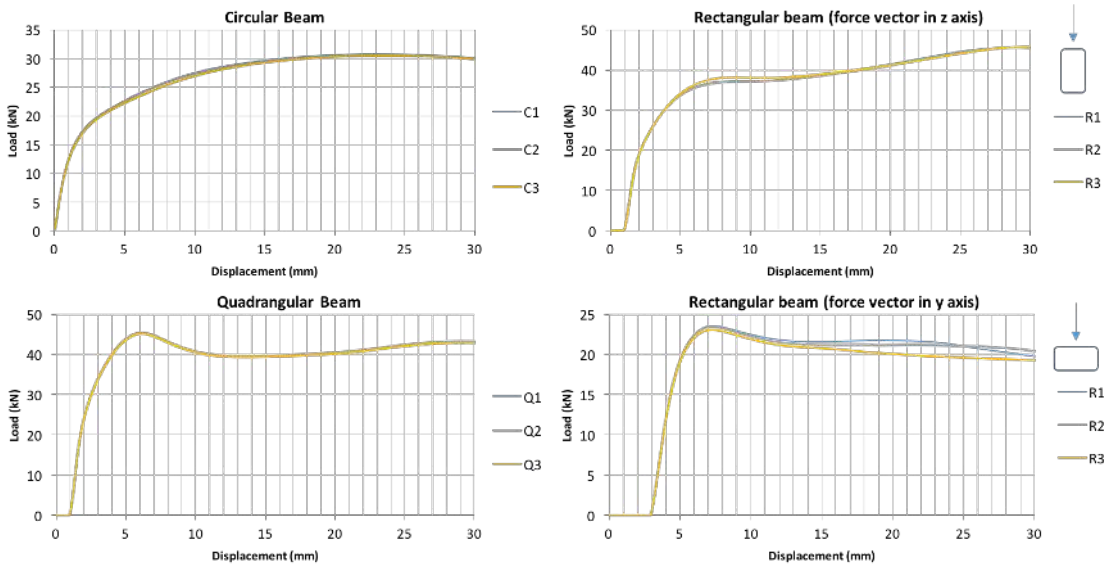

Figure 4.5: Four-point bending experimental results

4.2 Experimental Tensile Test

Although the same material was selected to every beam, the S235 grade does not specify a well determined stress-strain curve for the material, but a group of intervals where its mechanical properties should fit. However, the stress-strain curve is a crucial element when modeling the material in HyperWorks. For that reason, a tensile test is executed on material samples retrieved from the original beams.

4.2.1 Experimental Procedure

A 100kN MTS 661 High Capacity Force Transducer machine was used to perform this test. Rectangular specimens (initial length, L_0, and width, W) were extracted from the quadrangular and rectangular shaped beams. No specimen was retrieved from the circular beam due to the inability of testing curved profiles. No extensometer data was recorded due to equipment malfunction. The extracted output was a force/displacement curve, later converted in a stress/strain curve. This method affects solution quality, namely after the ultimate tensile strength is reached and reduction in area occurs. The experimental procedure can be described by the following algorithm:

1. The specimen of initial length L_0 is fixed between two crossheads;
2. While the lower crosshead remains fixed, the upper one applies a tension on the specimen by pulling it at a constant velocity v;
3. When the specimen fails, the machine detects it by the abrupt decrease in the applied force and stops the test;
4. The crossheads decrease the fixation pressure and it is possible to retrieve the tested specimen.

	L_0/mm	W/mm	$v/(mm/min)$
Tensile Test	250	10	2

Table 4.3: Tensile test configuration data

Three specimens from each type of beam (quadrangular and rectangular) are tested to ensure solution reliability. Table 4.3 sets the experimental values for the tensile test. The resulting curves are expected to be similar for the specimens retrieved from the rectangular beam and for the ones retrieved from the quadrangular beam, as they were ordered from the same supplier with the same S235 grade. The experimental procedure apparatus is shown in Figure 4.6.

4.2.2 Results & Discussion

During the test, an appropriate software records the applied force and plots it over the imposed displacement. Dividing the force by the section area, and dividing the imposed displacement by the original length, it is possible to convert the force/displacement curve into a stress/strain curve. These curves are

Figure 4.6: Tensile test apparatus

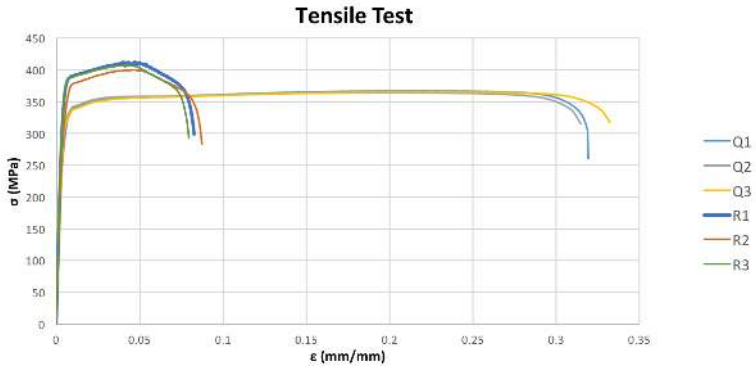

Figure 4.7: Tensile test results

presented in Figure 4.7 where the Q curves are related to the quadrangular beam specimens and the R curves are related to the rectangular beam specimens.

The first observation is that the different types of specimens are characterized by significantly different stress-strain curves. The initial step is apparently identical (same modulus of elasticity, E), but everything else is different. From the yield point, to the ultimate tensile strength passing by the major difference, the elongation at break, under 10% for the R specimens and over 30% for the Q specimens. Each type shows, however, great precision in the respective three trials, which shows that whatever difference between the results, it was not induced by any laboratorial procedure mistake.

Zooming in on the initial segments of both types of curve (Figure 4.8), it is possible to confirm the

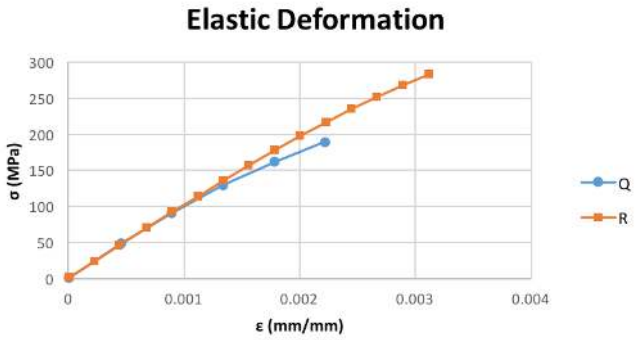

Figure 4.8: Elastic segment of the stress-strain curves

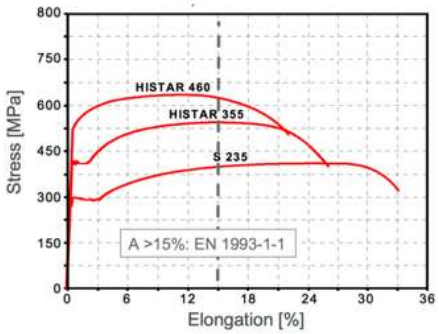

Figure 4.9: S235 typical stress-strain curve [34]

hypothesis that both materials share the same modulus of elasticity. However, it is also noticeable that the yield stress σ_y is larger on the R material than on the Q's. When comparing both curves to a traditional S235 steel, presented in Figure 4.9, it is clear that the Q material adjusts itself much better to the S235 grade than the R. The difference is so significative that one of two conclusions may be withdrawn: either the R material is not a S235 grade, or, during the extraction of the specimens from the original beam, some process somehow altered the material's mechanical properties. Either way, these results were not the expected. As the Q curve is much more similar to a typical S235 grade, during the model construction, it will be applied to the circular beam, whose material was not tested.

4.3 Numerical Simulation

In this section, a numerical model is built in HyperWorks and applied to all the different geometries tested in the laboratory. This model is also applied for both three-point bending and four-point bending configurations under the necessary geometrical adjustments.

4.3.1 Simulation Setup

The numerical setup was developed using the HyperWorks tools described in Chapter 3. The explicit non-linear finite element code, RADIOSS, is applied to compute the simulation. The beam, punch and support's geometries are the same used during the experimental tests. Materials are modeled through LAW36 – Piecewise-linear which builds a linear approximation of the true stress-strain curve from sample points collected from Figure 4.7. This law considers damage effects on the material, namely through the deletion of finite elements under higher strains than those which the material can withstand. Belytschko-Tsay 4-node shell elements are used to generate the beam's FE mesh. The use of shell elements is possible due to the small thickness of the beam's walls. A characteristic length of $5mm$ is used for the beam's mesh as, after a convergence analysis, this value showed a good compromise between solution quality and computational cost. The computational time of shell elements, when compared to solid elements, is lower and their reduced rigidity leads to a faster solution convergence. Belytschko-Tsay elements have a reduced (one-point) integration formulation with penalty methods to control spurious zero-energy deformation modes [32]. These elements are also applied to the punch and supports,

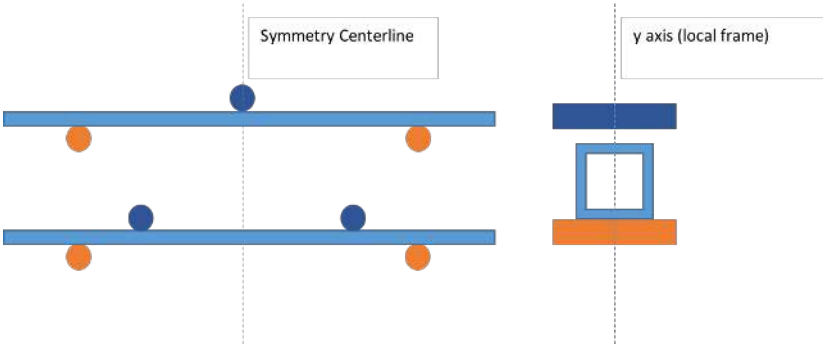

Figure 4.10: Setup double symmetry

which are considere rigid. This assumption is valid because the experimental punch and supports' rigidity (deformation) is much greater (smaller) than the beam's. Since the setup is symmetric towards its centreline and since the system cross section plus punch and support is also symmetric in relation to the z axis (Figure 4.10), only one fourth of the global system must be simulated. These simplifications account for a significant saving in computational time and cost do not affect in any way the system's response (provided the correct boundary conditions are applied at the symmetry planes).

Performing a quasi-static test requires a low impact speed. However, due to the small time steps induced by the also small characteristic length of a refined mesh's finite elements, the computational cost of a quasi-static simulation is not acceptable. For this reason, the simulation impact speed is accelerated by a factor of 2500 to a value of $500mm/s$. Strain rate effect may be ignored at these speeds because they are still relatively low. Results show that, despite the acceleration, the output curve remains independent on the speed value, while it remains low. In Chapter 5 the influence of the impact speed is studied in greater depth. Contacts are also defined, not only between the punch, the supports and the beam, but also a self-impact contact is created to avoid interpenetration caused by the beam's bending collapse. Representative images of the three-point bending and four-point bending numerical models are shown in Figure 4.11.

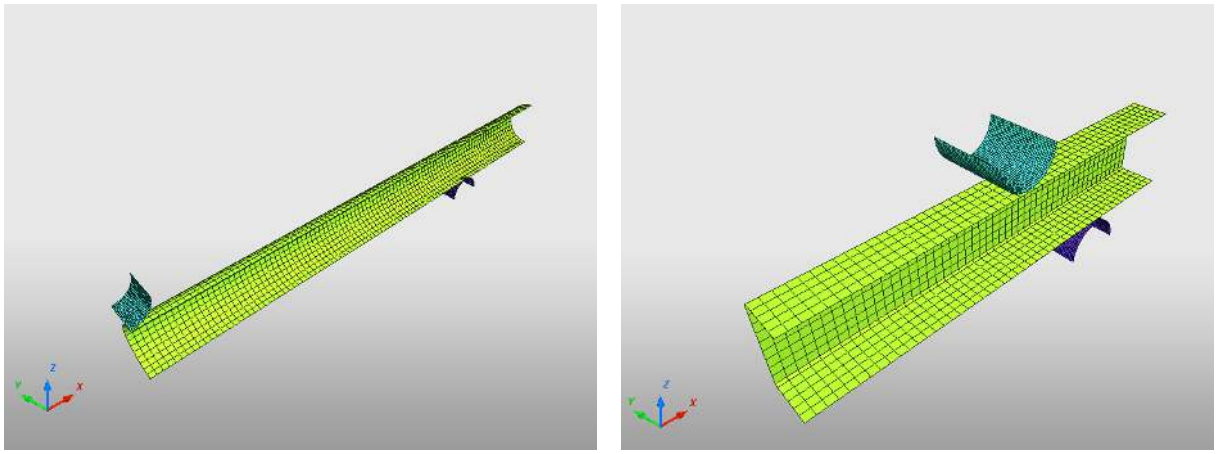

(a) Three-point bending

(b) Four-point bending

Figure 4.11: Bending numerical models

4.3.2 Results & Discussion

Figures 4.13 and 4.14 show the same test plots presented in Figures 4.4 and 4.5 but with the addition of the numerical curves obtained during the simulation. Figure 4.12 illustrates the bending simulation for both three-point and four-point bending models which can be compared with the experimental photos shown in Figure 4.3.

(a) Three-point bending

(b) Four-point bending

Figure 4.12: Bending simulations

The circular beam model shows a greater agreement with the experimental results in the three-point bending model, with the four-point bending experimental output having a positive offset, i.e., a similar shape but with higher values. The quadrangular beam shows a good agreement in both three-point bending and four-point bending, with the latter presenting an almost precise overlap between both experimental and numerical curves.

All the numerical curves obtained for the rectangular section do not fit the experimental results. The three-point bending simulation for the rectangular beam loaded in the y axis is the the only result where the numerical curve is similar to the experimental one, but even in this case, the accuracy of the model is not sufficient. The four-point bending solutions are even worse than the results obtained for the three-point bending simulation. The justification for this behavior, specially when compared to the accurate results obtained for the circular and quadrangular beams, may only rely on the stress-strain curve which is applied to rectangular beam, the R curve. This is obtained from Figure 4.7 and, as previously mentioned, differs significantly from the typical curve from a S235 material (see Figure 4.9). The main difference between the R curve and the Q curve is the elongation at break. The Q curve sustains strain values over 30% as the R curve does not reach even 10%. When the R curve is introduced in HyperWorks, it leads to a poor beam behaviour after the 10% strain is reached. Looking carefully at Figures 4.13 and 4.14 it is clear that the initial section of the numerical curve approximately fits the experimental results for both three-point bending and four-point bending rectangular configurations. However, the peak force is rapidly reached and from that point forward the applied force abruptly drops, consequence of reaching the maximum elongation sustained by the material. This is particularly visible in the four-point bending results since, due to a shorter distance between the impactor and the support, greater strains are applied to the material. From this results, it becomes clear that the R curve does not properly describe the material of the rectangular beam. The numerical model works, as seen for the circular and quadrangular beams, and the shape of the curve significantly differs from the typical S235 grade which was ordered from the supplier. A possible justification for the shape of the R curve is in the process through which the specimens were obtained. As they were cut from the original rectangular beam, there

may have been some residual stresses which altered the mechanical properties of the material, leading to poor tensile test results.

Overall it may be concluded that, not only the Q curves in Figure 4.7 represent an accurate description of the material behavior, but also that the numerical model adjusts itself to both quadrangular and circular beams in three and four-point bending tests. These results combined with the lack of confidence on the material description for the R material in Figure 4.7, which justifies the disagreement between numerical and experimental results for the rectangular beam, lead to the final conclusion of this chapter which states that the bending model, described in the last sections, is a robust and validated solution for testing the bending performance of a thin-walled beam, given the material accurate stress-strain curve.

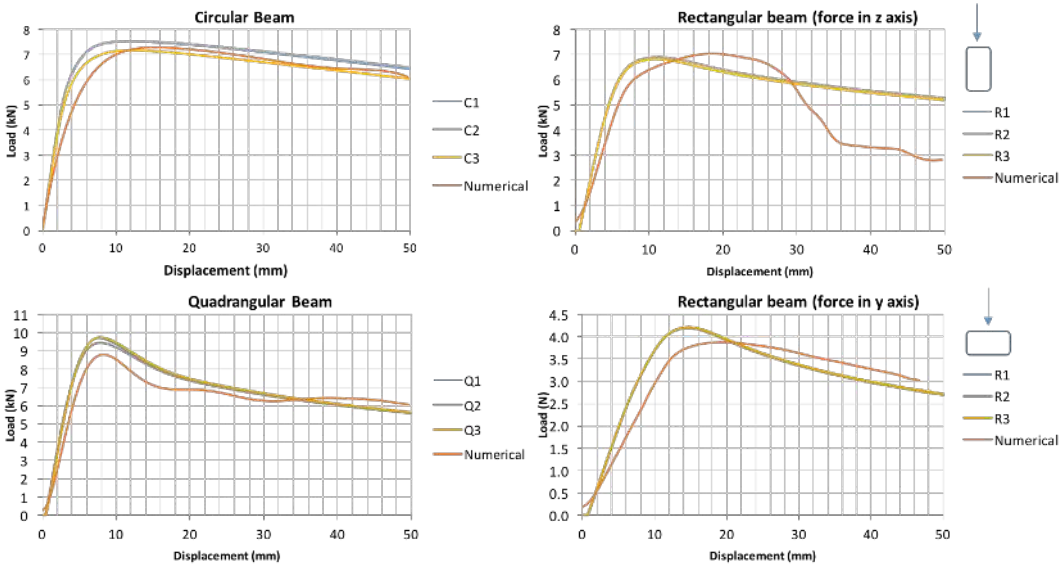

Figure 4.13: Three-point bending simulation results

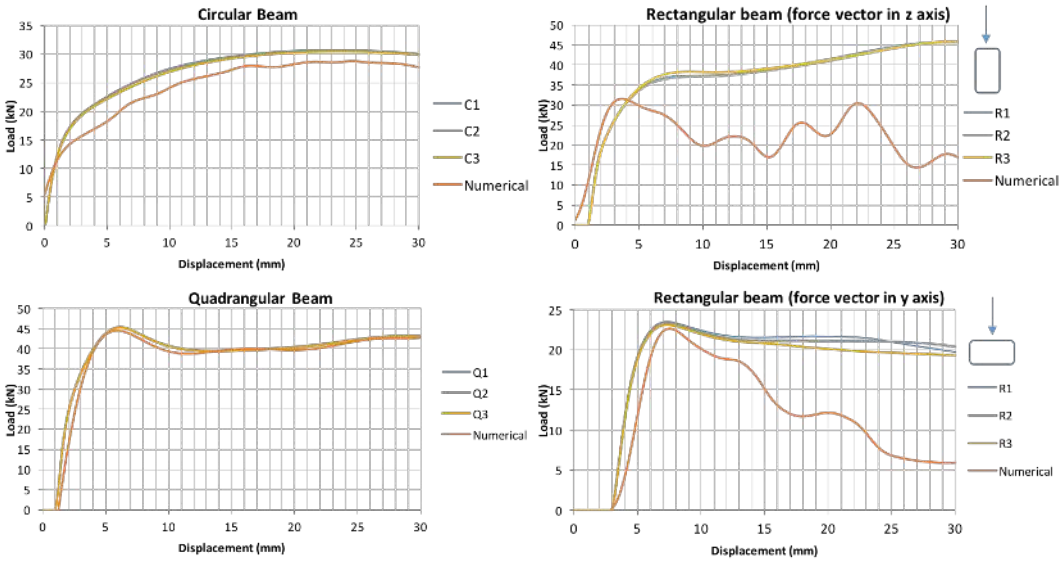

Figure 4.14: Four-point bending simulation results

Chapter 5

Side Intrusion Beam – Parametric Analysis

This chapter approaches the development of an improved solution for the design of a side intrusion thin-walled beam. Several geometries and materials will be tested in the three-point bending numerical model previously validated and their performance results will be compared according to the metrics presented in Chapter 3. The first step is the definition and analysis of a reference beam. This beam's dimensions were based on previous iterations of the beam used in the Be vehicle. Starting from this beam's geometry, a large group of geometrical parameters will be altered in order to understand which solutions increase more significantly the bending performance, always considering other relevant parameters such as the beam's mass or the volume required for the beam's installation. A comprehensive list of metallic materials will be tested under the same conditions with the same purpose. Despite the use of different materials, as seen in Chapter 4, the numerical model is valid as long as the according stress-strain curve is provided. Besides the geometrical and material analyses, an extra study is performed to understand the effect of deformation speed in the bending performance of a beam. Zhang et al. [6] performed a similar analysis showing that for a quadrangular beam, in a region where the strain-rate effect can be neglected, the impact speed does not play a crucial role in the beam's bending performance. This is of particular relevance since the three-point bending test is conducted in a quasi-static environment, and even if the numerical model validated in Chapter 4 is already accelerated (without any consequence upon the beam's response), the speed at which the impactor collides into the beam is still much lower than the one at which side collisions frequently occur. Finally, a selection tool is built to combine different criteria regarding the selection of the best solution for the development of a side intrusion beam.

5.1 Reference Beam

Setup

This section describes and analyzes the base beam for the parametric study. A rectangular shaped thin-walled beam of length L_{ref} illustrated in Figure 5.1 is considered. Table 5.1 supplies the data which fully describes the reference beam. The numerical model applied to the reference beam is identical to the one validated in Chapter 4. The provided data on the previous iteration of the Be project did not specify the beam's material. For this reason, a standard dual-phase steel, DP250/450, was selected as reference material. The properties of this material are far from the current options for SIB application. This option is intended to leave room for improvement. This same steel will be applied to all the geometry related parametric analyses, as the reference beam's shape will be applied to all the material related parametric studies.

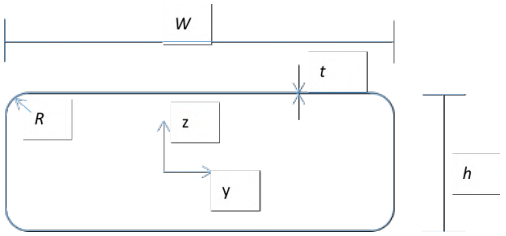

Figure 5.1: Reference beam

	$L_{ref}(mm)$	$R(mm)$	$h(mm)$	$t(mm)$	$W(mm)$
Ref. Beam	800	3	25	1.5	50

Table 5.1: Reference beam data

	$\rho(kg/m^3)$	$E(GPa)$	υ	$\sigma_y(MPa)$	$\sigma_{UTS}(MPa)$
DP250/450	8000	210	0.3	250	450

Table 5.2: DP250/450 properties (Adapted from [28])

Table 5.2 displays the properties of a DP250/450 steel grade, where ρ is the material's density, E is its modulus of elasticity, υ the Poisson's ration and σ_{UTS} its ultimate tensile strength. The Advanced High Strength Steel (AHSS) guide [28] from where the stress-strain curve illustrated in Figure A.1 (presented in Appendix A) and the stresses of Table 5.2 are retrieved, does not explicitly specify the values ρ, E and υ. However, since this guide presents a vast library of stress-strain curves for steel materials, required to perform the numerical simulations, standard steel values are assumed for these three parameters whenever this guide is used as the reference for a material. Since the physical boundaries which physically limited the experimental tests do not exist in the numerical model, an extended simulation will be conducted in order to ensure that the full bending behavior of each beam is observed. Then, a maximum displacement, δ_{max}, of $150mm$ will be imposed to each beam.

Results

The output of the simulation is, as seen in Chapter 4, a force/displacement curve, illustrated in Figure 5.2. From this plot, it is possible to compute the performance metrics described in section 2.3.3 (F_{max},

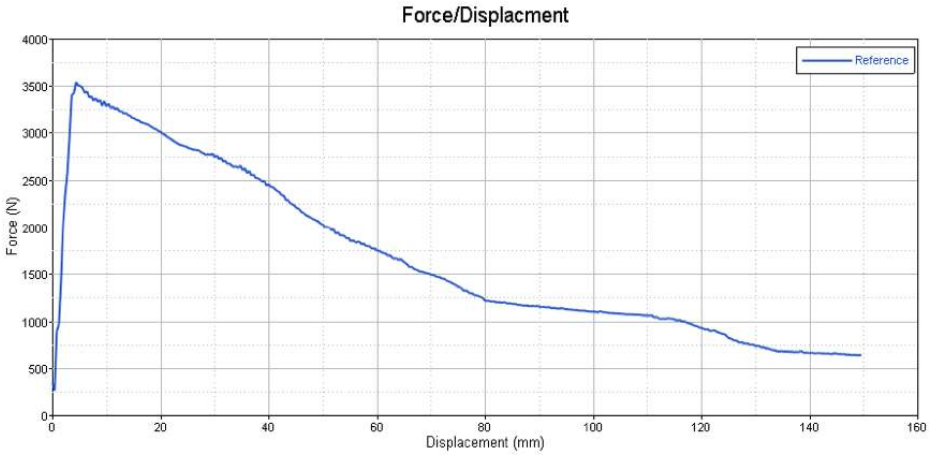

Figure 5.2: Force/displacement curve for the reference beam

EA, SEA, CFE). The beam's mass and the average applied force are required to compute the metrics above and, together with the cross-sectional area of the beam, are presented in Table 5.3.

	$Mass(kg)$	$F_{avg}(N)$	$Area(mm^2)$
Ref. Beam	1.360	1671.58	1250

Table 5.3: Reference beam output data

Using the values of Table 5.3 and applying equations (2.28)(2.29)(2.30) and (2.31), the bending performance metrics are computed and presented in Table 5.4.

	$F_{max}(N)$	$EA(kJ)$	$SEA(kJ/kg)$	CFE
Ref. Beam	3538.19	250.61	184.29	0.47

Table 5.4: Reference beam bending performance

These results alone do not provide a significant analysis on this beam's bending performance. However, when compared with different solutions from different geometries and materials, these metrics will work as a performance comparative tool. The only worthy remark at this point concerns the force/displacement curve's shape. Its initial peak and consequent abrupt decrease in the applied force justify the low CFE. This behavior is not desirable since the majority of the energy is absorbed during the initial peak, leading to strong accelerations transmitted to the vehicle passengers.

5.2 Geometry Analysis

Once the reference results are obtained, the comprehensive geometrical study may be conducted and the bending performance of the proposed solutions may be compared. Several geometry variations to the reference cross-section will be tested. First, a batch of regular polygons is tested to study the different bending behavior of these simple geometries. Then the side proportions of a rectangle, the diagonal proportions of an ellipse and the angle proportions of an isosceles triangle are altered. The

inner reinforcement of the reference beam is also studied. Open sections are a common solution in the automotive industry and several standard solutions are also analyzed. Finally the effect of thickness variation in the thin-walled beams is tested. Besides the geometrical variation, in this chapter is also included a study on the effects of the impactor speed on the beam's response. All the parameters shown in Table 5.5 are assumed constant throughout section 5.2 if not clearly stated otherwise.

Beam	$L(mm)$	$h(mm)$	$W(mm)$	$Material$	$\delta_{max}(mm)$	$v(mm/s)$	$t(mm)$
All	800	25	50	DP250/450	150	500	1.5

Table 5.5: Constants table

L is the beam's length, h is the beam's height, W its width, δ_{max} the maximum imposed displacement, v the imposed speed and t the walls' thickness. The force/displacement curves for each analysis are available at Appendix B.

5.2.1 Regular Polygons

This first group is composed by three, four, five and six-sided regular polygons, plus the circle. Two loading scenarios are considered for each polygon: normal to one of the polygon sides (due to symmetry the selected side is irrelevant) and through one of the vertexes (once again, due to symmetry, the vertex choice is irrelevant) passing by the the center of the polygon. Regular polygons were selected to study the bending behavior of such different geometries in order to understand how the number of sides of a polygon can change the bending performance of a beam.

Setup

The numerical model validated in Chapter 4 and adapted to test the reference beam in section 5.1 is applied to regular polygons analysis and to all the remaining geometry sets in section 5.2. The tested geometries and their respective loading scenarios are illustrated in Figure 5.3. The z direction, in which the loading is performed, simulates the impact direction in a real crash event. This direction is also representative of the door thickness, normal to both the inner and the outer panels. The h parameter in Figure 5.3 is frequently the limiting dimension for the beam development since other components must be fitted inside the door (audio system, window, window elevator, among others). As in the previous iteration a value of $h = 25mm$ was used, this will be considered a design limitation and, if possible, always applied to the tested geometries. The simulation will be carried until a maximum deformation $\delta_{max} = 150mm$ is reached. The beams' length, L, is identical to the length of the reference beam, $L_{ref} = 800mm$. This length will be considered for all the tested geometries and materials. The thickness, $t = 1.5mm$ is kept constant. As previously mentioned, in all the geometry analyzes, the applied material will be the steel grade DP250/450 which properties can be found in Table 5.2.

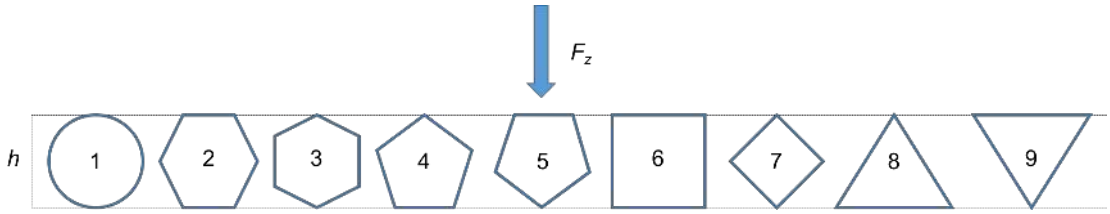

Figure 5.3: Regular polygons loading scenarios

Results

Figure B.1 (in Appendix B) shows the force/displacement curves for the regular polygons geometries and for the reference beam. Table 5.6 shows the auxiliary output data required to compute the bending performance metrics plus the smaller rectangular area where each geometry can be inserted. Figure 5.4 shows the bending performance results for the nine different loading scenarios.

Beam	1	2	3	4	5	6	7	8	9	Reference
$Mass(kg)$	0.705	0.666	0.773	0.718	0.718	0.880	0.609	0.787	0.787	1.360
$F_{avg}(N)$	1243.1	1170.9	1460.2	1309.5	1492.0	1714.2	1079.5	2052.3	1406.6	1671.58
$Area(mm^2)$	625.00	541.28	721.70	657.18	657.18	625.00	625.00	721.70	721.70	1250.00

Table 5.6: Regular polygons output data

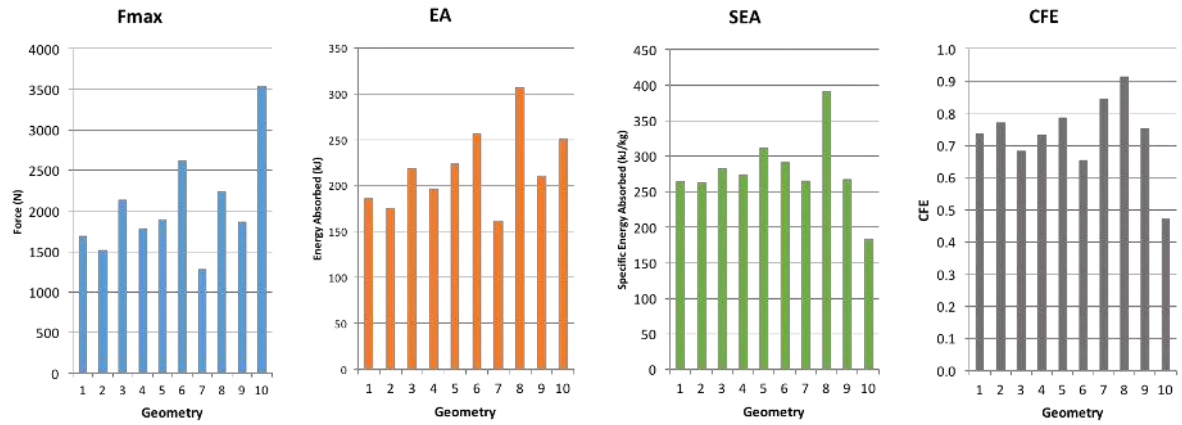

Figure 5.4: Regular polygons bending performance metrics

The higher F_{max} value is recorded for the reference beam (geometry number 10 in Figure 5.4), which represents a high initial peak force, leading to strong accelerations transmitted to the passengers, increasing the probability of injury. Both the triangular and quadrangular beams have a greater EA than the reference beam, despite its greater mass. When measured relatively to its mass, the reference beam presents the worse energy absorption, SEA, value of all the geometries. The same with the crash force efficiency, consequence of the initial peak force, clearly visible in Figure B.1 (in Appendix B). Regarding the remaining geometries, the scenario 8, where the triangular beam is loaded in its vertex shows the best bending performance, with the greatest values for EA, SEA and CFE. Plotting F_{max} and mass values together (see Figure 5.5) it is clear that there is a connection between these two metrics. This

relationship is expected since, as seen in Chapter 2 the fully plastic moment of a beam, when the plastic hinges are developed, followed by a decrease in the beam's capacity of sustaining the applied load, is dependent on the beam's cross sectional area (equation (2.27)). A greater mass corresponds to a greater area (with constant thickness) and consecutively to a greater peak force. Preventing a high value for the initial peak force is important to avoid high accelerations, hence the advantage of having a small cross-sectional area when it comes to analyzing this particular metric. All the curves plotted in Figure B.1 (in Appendix B) share a similar bending behavior: the applied load starts at zero and has a rapid initial growth; at some point F_{max} is reached and from that point forward the sustained load starts to decrease. F_{max} is attained when fully developed plastic hinges appear. Its magnitude depends mainly on the cross-sectional area, but the required displacement to reach the fully plastic state also plays a crucial role when determining the energy absorption capability ob the beam. The EA metric is computed directly by the integral of the force/displacement curve, which means that a high value of F_{max} reached only after a high displacement δ will lead to a greater EA value. This is visible in Figure B.1 (in Appendix B) where, despite the reference (10) and the quadrangular (6) beams having a higher peak force than the triangular section (8), because the triangular shape only reaches it with a greater displacement, it has a much greater energy absorption capacity (see Figure 5.4) than the other two geometries. The larger and wider area of the reference beam facilitates the appearance of plastic hinges leading to an initial high energy absorption capacity which rapidly drops. On the other hand, the alignment of the triangular section (8) sides with the load direction, postpones the development of the plastic hinges (high bending rigidity) leading to a large energy absorption capacity. Regarding the main goal of this analysis, it is visible that with the increasing number of sides of a polygon, the highest EA value, between the two tested orientations, decreases. The triangular section (8) has the highest EA, followed by the quadrangular (6), the inverted pentagonal (5), the straight hexagonal (3) and finally the infinite sided polygon, the circular beam (1). The energy absorption parameter is strongly related to the development of plastic hinges which is facilitated by an increasing number of edges in each geometry. These natural lines make it easier for the material to bend, leading to a poorer bending performance. However, as the number of sides increases, the less depending the beam's performance becomes on the impact orientation. Looking at the SEA gap between different orientations (SEA is considered because, due to the h restriction, different orientations imply significantly different mass values), it is clear that it is maximum for the triangular beam and minimum, actually null, for the circular beam, which is totally independent on the impact direction.

5.2.2 Geometrical Proportions

This second geometry set studies in greater depth some of the geometries tested in section 5.2.1. The beams with a higher energy absorption capacity, the quadrangular and the triangular, are selected together with the circular beam, which displays the minimum dependence on the impact direction. Keeping the geometries limited to the available height h, the importance of their characteristic dimension is studied, in particular the effect of having either a more flat or thinner configuration. Theoretically, equation

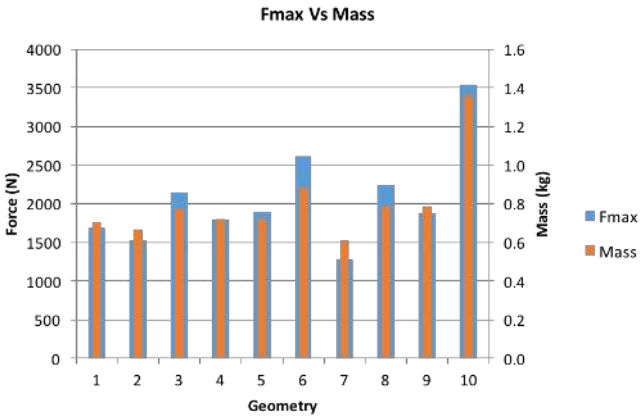

Figure 5.5: Regular polygons F_{max} Vs mass

(2.27) shows that a greater area leads to a higher fully plastic moment, hence to a greater maximum force. However, as previously noted, a higher peak force does not necessarily lead to a greater energy absorption. This set will test the relationship between a higher peak force and the energy absorption of similar parametrical geometries.

Setup

Three geometries (rectangle, ellipse and triangle) are simulated. Two key parameters of each geometry are selected and three different proportions are applied to each set of parameters. This set geometries are illustrated in Figure 5.6 and the geometrical parameters values are specified in Tables 5.7 and 5.8. The simulation specifications are set according to Table 5.5 and the numerical model validated in Chapter 4 is used.

	$m = 2n$			$m = n$			$m = n/2$		
Geometry	1	4	7	2	5	8	3	6	9
m	a_1	a_4	α_7	a_2	a_5	α_8	a_3	a_6	α_9
n	h	h	β_7	h	h	β_8	h	h	β_9

Table 5.7: Geometrical proportions parameters

$h(mm)$	$a_1(mm)$	$a_2(mm)$	$a_3(mm)$	$a_4(mm)$	$a_5(mm)$	$a_6(mm)$	α_7	α_8	α_9	β_7	β_8	β_9
25	50	25	12.5	50	25	12.5	90^o	60^o	36^o	45^o	60^o	72^o

Table 5.8: Geometrical proportions parameters values

Results

Figure B.2 (in Appendix B) shows the force/displacement curves for this geometries set. Table 5.9 shows the auxiliary output data required to compute the bending performance metrics plus the smaller

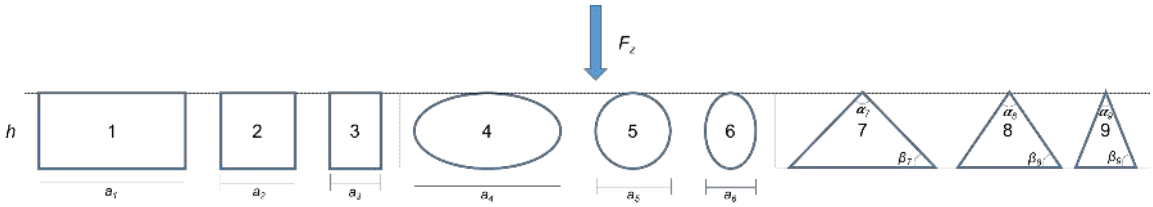

Figure 5.6: Geometrical proportions loading scenarios

rectangular area where each geometry can be inserted. Figure 5.7 shows the bending performance results for the nine different loading scenarios.

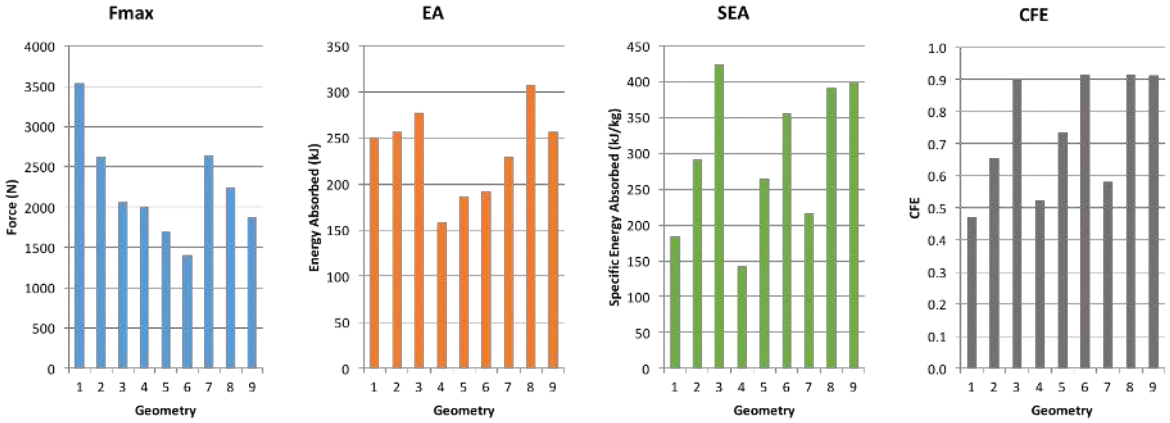

Figure 5.7: Geometrical proportions bending performance metrics

Beam	1	2	3	4	5	6	7	8	9
$Mass(kg)$	1.360	0.880	0.654	1.115	0.705	0.539	1.061	0.787	0.644
$F_{avg}(N)$	1671.6	1714.2	1848.8	1055.2	1243.1	1281.3	2052.3	2052.3	1714.4
$Area(mm^2)$	1250.00	625.00	312.50	1250.00	625.00	312.50	1250.00	883.88	657.16

Table 5.9: Geometrical proportions output data

All three geometries display a similar behavior when the parameter proportions are altered. As each geometry gets thinner, the area is reduced, hence the mass becomes lower. As seen in section 5.2.1, the drop in mass is followed by a drop in the maximum force. Despite the lower mass, the energy absorption increases in all geometries (with the exception of triangular beam (9)), as the width decreases. This leads to an even greater increase in the specific energy absorption (less mass absorbs more energy). The crash force efficiency also increases with a thinner geometry. This is due to a change in the force/displacement curve configuration. For the wider geometries (1, 4 and 7), the curve displays an initial peak force followed by a sudden drop in load sustaining capacity. On the other hand, the thinner geometries (3, 6 and 9), display a much more constant behavior, only reaching F_{max} after a considerable displacement is imposed (the curve does not display a peak). This constant performance is responsible for the greater values of energy absorption, despite the lower peak force, and is caused by the structural rigidity imposed by having a more aligned geometry with the loading direction. The thinner

configuration delays the development of plastic hinges, requiring a greater displacement before the drop in the load sustaining capacity occurs (plastic collapse). Triangular beam (9), however, represents an exception due to a decrease in the EA and CFE values (despite having a greater SEA). This leads to the hypothesis of the existence of an optimal proportion, for a determined available height, h, where the energy absorption is maximum for each specific shape.

5.2.3 Reference Beam Reinforcement

This geometry set studies the effect on bending performance of the introduction of inner thin-walled reinforcements in the reference beam.

Setup

Reinforcement introduction has the goal of increasing the beam's bending performance without further increasing the necessary space to fit the beam, nor changing the installation requirements. Five different reinforcement configurations are simulated. Two of those configurations, 3 and 5, are reinforced by the introduction of horizontal and vertical ribs, respectively. The other three configurations, 1, 2 and 4 are reinforced by the combination of previously tested geometries, the triangular , the ellipse and the diamond, respectively. The reinforced geometries are illustrated in Figure 5.8. The reinforcement thickness is kept constant and identical to the remaining cross-section. The simulation specifications are set according to Table 5.5 and the numerical model validated in Chapter 4 is used.

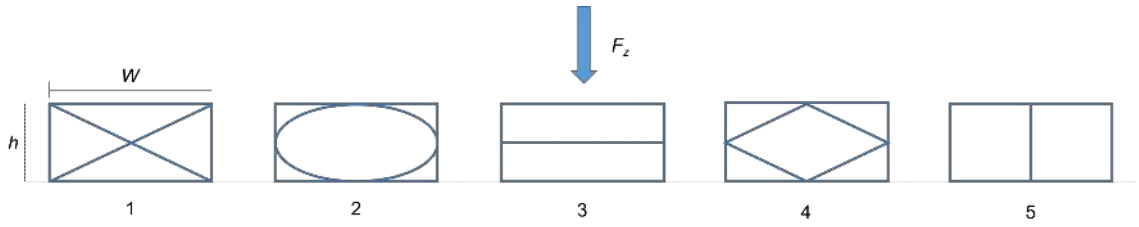

Figure 5.8: Reference beam reinforcements loading scenarios

Results

Figure B.3 (in Appendix B) shows the force/displacement curves for the reinforced geometries. Table 5.10 shows the auxiliary output data required to compute the bending performance metrics plus the smaller rectangular area where each geometry can be inserted. Figure 5.9 shows the bending performance results for the five different loading scenarios plus the reference beam.

Beam	1	2	3	4	5	Reference
$Mass(kg)$	2.382	2.475	1.826	2.395	1.586	1.360
$F_{avg}(N)$	3092.7	3324.3	2536.0	3819.5	3718.8	1671.58
$Area(mm^2)$	1250.00	1250.00	1250.00	1250.00	1250.00	1250.00

Table 5.10: Reference beam reinforcements output data

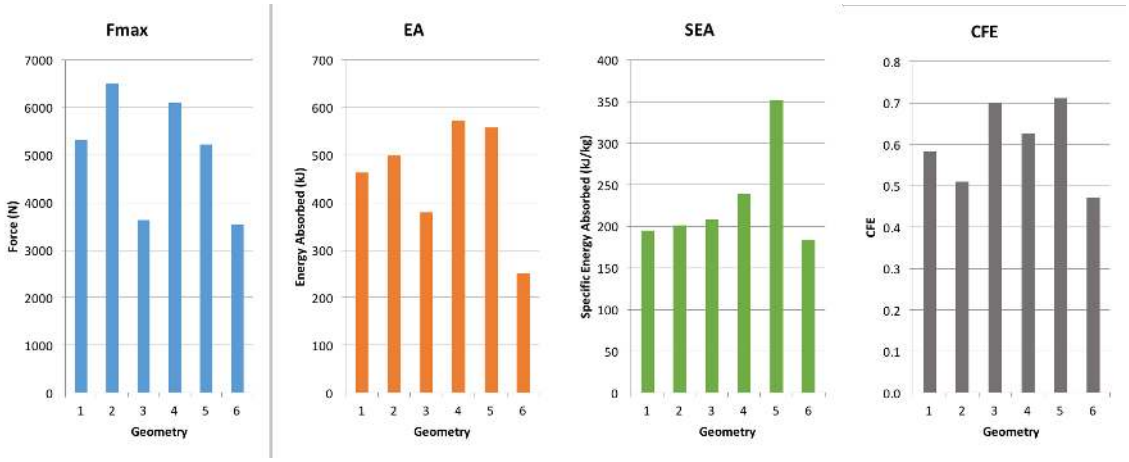

Figure 5.9: Reference beam reinforcements bending performance metrics

The first observation is that Geometry 5 has the second greatest energy absorption capacity and, when measured by kg, it has, by 47%, the largest SEA when compared with the following solution (4). Beam 5 also has the highest CFE. This outstanding bending performance is a consequence of the vertical reinforcement. As seen in previous sections, the more aligned with the loading direction the section is, the better the bending performance. Introducing a thin-walled reinforcement perfectly aligned with the applied force, delays the appearance of plastic hinges, which drastically increases the beam's rigidity. The reference beam (represented in Figure 5.9 as number 6) has a worse bending performance considering every metric than any of the tested solutions, hence the conclusion that inner reinforcements introduction are a good way of improving the side intrusion beam design. A high initial force may present a real danger for the passenger, but if the maximum load which a beam can sustain is too low, it would mean that energy absorption capacity of the beam would be low as well. In order to achieve a good bending performance, a high crash force efficiency is required. This efficiency is not sufficient, as the average force can be close to the maximum load both being low, but this proximity, which results from a steady force/displacement curve, is a requirement for a good performance since it is representative of a large energy absorption capability throughout the whole deformation process. It is more important for a beam to have a high F_{avg} than a high F_{max} since the relationship between the first and the energy absorption is direct, as given by equation (2.32). Globally, the results from configurations 1, 2 and 3, where the reinforcements are focused on the horizontal direction, show a worse bending performance than the more vertical solutions, 4 and 5. The comparison between geometries 1 and 4 clearly shows how important the reinforcement displacement can be. The same mass is added, but with a more vertical configuration, an EA improvement of 24% is achieved.

5.2.4 Geometrical Expansion/Reduction

So far, the beam's volumetry has been limited by the height value, h. This is a reasonable consideration since the available space for installing the beam is often quite limited. However, if an expansion becomes possible, or if a reduction becomes necessary, it is important to understand how the beam performance would change in such scenarios. This geometries set studies the effect of simple expansion

and reduction processes in the bending performance of simple closed section thin-walled beams.

Setup

The reference beam is tested alongside the circular beam. Two different geometries are simulated in order get a more general understanding of these variations effect (see Figure 5.10). Geometries 2 and 5 were already tested before. Geometry two is identical to the reference beam and geometry 5 is the same circular beam tested in section 5.2.1. Then, $b_2 = a_5 = h = 25mm$ and $a_2 = W = 50mm$.

Geometries 1 and 4 printed dimensions are half of the equivalent dimensions in geometries 2 and 5 respectively. Geometries 3 and 6 printed dimensions are the double of the equivalent dimensions in geometries 2 and 5 respectively. In Table 5.11 are listed all the geometrical parameters values for Figure 5.6. The simulation specifications are set according to Table 5.5 and the numerical model validated in Chapter 4 is used.

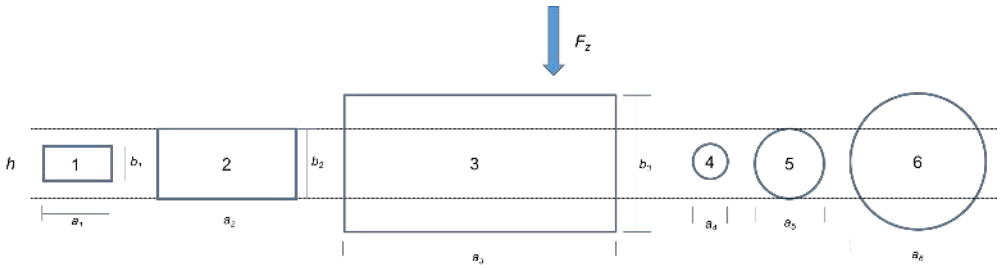

Figure 5.10: Geometrical expansion/reduction loading scenarios

$h(mm)$	$a_1(mm)$	$a_2(mm)$	$a_3(mm)$	$a_4(mm)$	$a_5(mm)$	$a_6(mm)$	$b_1(mm)$	$b_2(mm)$	$b_3(mm)$
25	25	50	100	12.5	25	50	12.5	25	50

Table 5.11: Geometrical expansion/reduction geometrical parameters values

Results

Figure B.4 (in Appendix B) shows the force/displacement curves for the expanded geometries. Table 5.12 shows the auxiliary output data required to compute the bending performance metrics plus the smaller rectangular area where each geometry can be inserted. Figure 5.11 shows the bending performance results for the six different loading scenarios.

Beam	1	2	3	4	5	6
$Mass(kg)$	0.640	1.360	2.800	0.329	0.705	1.461
$F_{avg}(N)$	818.6	1671.6	3600.4	361.9	1243.1	2573.9
$Area(mm^2)$	312.50	1250.00	5000.00	156.25	625.00	2500.00

Table 5.12: Geometrical expansion/reduction output data

Expanding the geometry has some immediate consequences. The area increases and, with constant thickness, so does the beam's mass. With the expansion of the geometry, three metrics vary similarly,

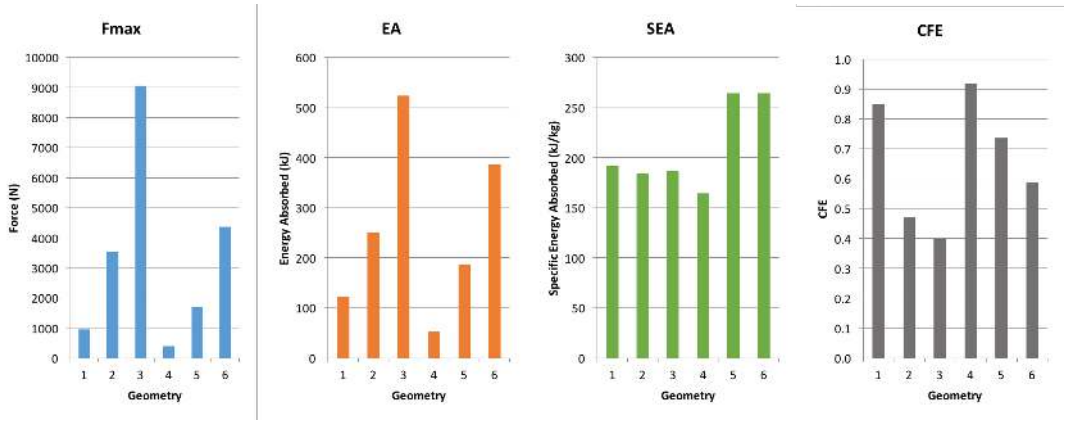

Figure 5.11: Geometrical expansion/reduction bending performance metrics

independently on the geometry: F_{max} and EA increase and CFE decreases. This means that a greater and heavier beam sustains a higher maximum force, absorbs more energy, but does it in a more abrupt process as the force/displacement curve migrates to a more steep configuration. The SEA parameter, however, does not display such a linear evolution. The results for the expansion of the rectangular beam suggest that the SEA value is dependent only on the geometry and not on its dimensions, i.e., for each particular geometry there is a specific SEA value, which would lead to a linear relationship between the absorbed energy and the beam's mass (provided the geometry was kept proportional). The circular beam results disprove this hypothesis, at least partially, since the smaller beam presents a different SEA value than the remaining two. However, beams 5 and 6 have the same SEA which, combined with the results from the rectangle expansion simulations, suggest that, provided a certain dimension (note that beam 5 has a diameter which is equal to the rectangle number 1 width), each geometry displays a constant SEA value regardless its mass. During the analysis of section 5.2.2, an unexpected EA value was obtained for the rectangular beam (number 9) when its width was dramatically reduced. Despite being just an hypothesis, the suggestion that there is a lower limit, under which the beam's behavior is different, appears again in this geometries set. In fact, as the characteristic dimensions of the cross-section's geometry decrease, if a constant thickness is kept, then the beam's behavior deviates from what is to be expected from a thin-walled beam and moves closer to the behavior of a solid body. Regardless the confirmation of the hypothesis stated in this section, the results allow the conclusion that the expansion or reduction of the reference beam to, at least, a factor of two, will not change its SEA value. Overall, it can be concluded that expanding the geometry leads to a higher energy absorption, followed by a greater peak force and an inferior crash efficiency. The change in the force/displacement curve pattern to a more steep shape is undesirable since it connects a greater EA to a greater initial acceleration, potentially dangerous for the passengers.

5.2.5 Open Sections

This geometries set, similarly to section 5.2.1, comprehends a study on diverse geometries, this time on open section thin-walled beams.

Setup

Three common open section geometries, C shape, I shape, L shape are tested together with some open variations of the already tested circular and rectangular beams. Open section beams have manufacturing advantages (may be obtained through stamping, for instance) and are commonly used in the industry. Open section geometries are illustrated in Figure 5.12 and the geometrical dimensions are specified in Table 5.13. The simulation specifications are set according to Table 5.5 and the numerical model validated in Chapter 4 is used.

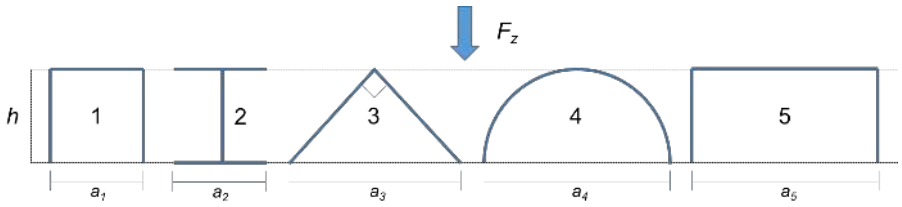

Figure 5.12: Open sections loading scenarios

$h(mm)$	$a_1(mm)$	$a_2(mm)$	$a_3(mm)$	$a_4(mm)$	$a_5(mm)$
25	25	25	50	50	50

Table 5.13: Open sections geometrical parameters values

Results

Figure B.5 (in Appendix B) shows the force/displacement curves for the open section geometries. Table 5.14 shows the auxiliary output data required to compute the bending performance metrics plus the smaller rectangular area where each geometry can be inserted. Figure 5.13 shows the bending performance results for the five different loading scenarios plus the reference beam (number 6).

Beam	1	2	3	4	5	Reference
$Mass(kg)$	0.707	0.706	0.666	0.758	0.947	1.360
$F_{avg}(N)$	1604.3	1972.1	659.4	837.6	1616.99	1671.6
$Area(mm^2)$	625.00	625.00	1250.00	1250.00	1250.00	1250.00

Table 5.14: Open sections output data

Observing Figure B.5 (in Appendix B), the first great difference from all the tested open sections in relation to the reference beam is the force/displacement curve shape. While the reference beam displays a peak-like curve, all the open section beams display a much more steady bending behavior. This difference is emphasized by the CFE plot (Figure 5.13) which shows greater values for all the open sections. Nonetheless, beams 3 and 4 display a lower CFE value. This is not because their force/displacement curve is more steep, but because their load sustaining capacity is much inferior when compared with the other beams, dropping to near zero values with an imposed displacement much lower than δ_{max}. Despite the greater CFE, these geometries have a lower bending performance

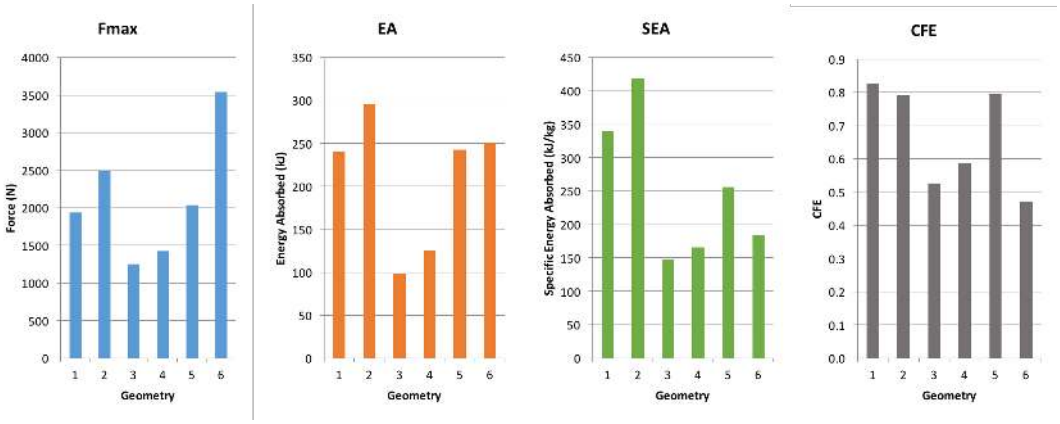

Figure 5.13: Open sections bending performance metrics

than even the reference beam (lower F_{max}, EA and SEA). The vertical web of beam number 2 grants it the best bending performance, once again dependent on the perfect alignment with the applied force. Beam 1, despite having a SEA value 18% lower than beam 2, has a C shape which is a more robust solution, providing a SEA value equivalent to the vertically reinforced beam (beam number five in Figure 5.8). Finally, it is interesting to evaluate the effect of öpeningä section. Beam 5 is no different than the reference beam without its lower flange. Removing this component and opening the section, almost the same EA value is obtained. This with a lower mass, a higher crash force efficiency and a much lower F_{max}. This result alone shows the evident advantages of opting for an open section beam.

5.2.6 Thickness Variation

Finally, this geometries set studies the effect of thickness variation in the bending performance of the reference beam. Increasing the walls' thickness will lead to a greater mass and a higher F_{max}. The three-point bending test will dictate how the remaining parameters change in these conditions.

Setup

Four different thickness values (including the reference t) are evenly applied through the cross-section. In a thin-walled beam the thickness of both the webs and the flanges are expected to have a great impact in the beam's bending performance. Thickness variation is illustrated in Figure 5.14 and the geometrical dimensions are specified in Table 5.15. The simulation specifications are set according to Table 5.5 and the numerical model validated in Chapter 4 is used.

$h(mm)$	$W(mm)$	$t_1(mm)$	$t_2(mm)$	$t_3(mm)$	$t_4(mm)$
25	50	0.5	1.5	3	5

Table 5.15: Thickness variation geometrical parameters values

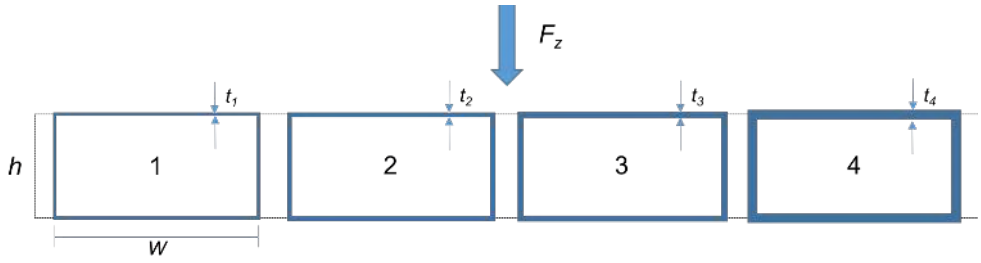

Figure 5.14: Thickness variation loading scenarios

Results

Figure B.6 (in Appendix B) shows the force/displacement curves for the thickness variation geometries. Table 5.16 shows the auxiliary output data required to compute the bending performance metrics plus the smaller rectangular area where each geometry can be inserted. Figure 5.15 shows the bending performance results for the four different loading scenarios.

Beam	1	2	3	4
$Mass(kg)$	0.533	1.360	2.720	4.533
$F_{avg}(N)$	328.9	1671.6	5909.3	14142.7
$Area(mm^2)$	1250.00	1250.00	1250.00	1250.00

Table 5.16: Thickness variation output data

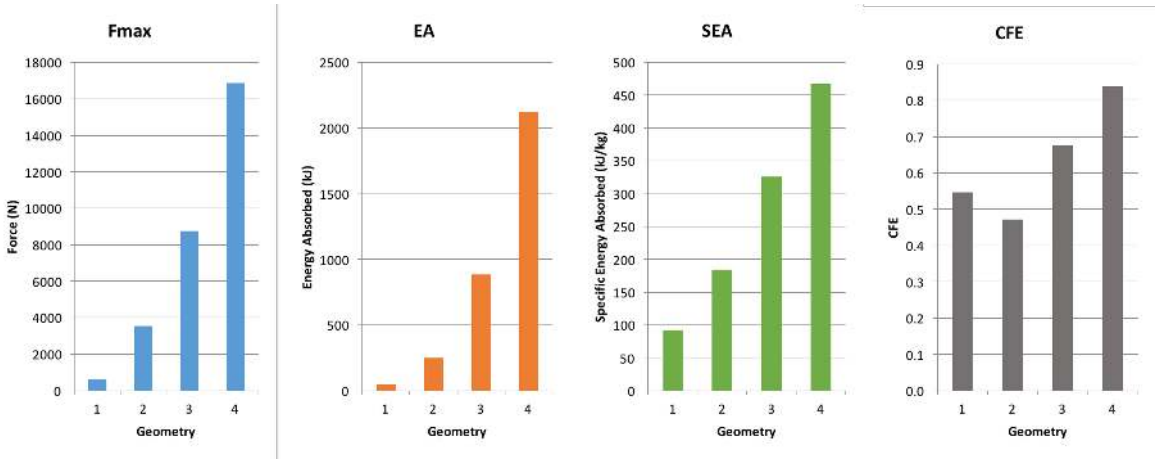

Figure 5.15: Thickness variation bending performance metrics

An assumption is made regarding the cross-sectional area, which is considered constant despite the thickness increase. As expected, thickness variation plays a determinant role regarding beam bending performance. Thickness increase leads to a greater F_{max}, EA, SEA and CFE (with the exception of an initial drop from beam 1 to beam 2) which, not only means a greater energy absorption capacity, but also that the increase in maximum force is not followed by a steeper curve, but on the contrary, by a steadier response as seen in Figure B.6 (in Appendix B). A greater thickness delays the hinge development by strengthening each wall, leading to a quite superior bending performance. The results tendency suggests that a further increase in wall thickness would lead to an even better performance.

However, it is important to remember that the thin-walled behavior relies on the assumption of thin walls. A great increase in thickness would inevitably lead to a situation similar to that observed in section 5.2.4 (beam 4) where unexpected results occurred once the beam thickness became closer to the order of magnitude of the cross-section's characteristic dimensions.

5.2.7 Impact Speed

This set studies the effect of the impact speed in the bending performance of two different beams. This analysis is particularly important since it validates that all the analyses performed on the geometries' bending performance under a low speed is equally valid when higher impact rates (crash event, for instance) are applied.

Setup

Four different velocities (including reference velocity v) are applied to both the reference and the circular beams. The maximum tested velocity is equivalent to $36km/h$ which is similar to the imposed speed ($32km/h$) in a pole impact test performed by EuroNCAP. Impact speed configurations are illustrated in Figure 5.16 and the geometrical dimensions are specified in Table 5.17. The simulation specifications are set according to Table 5.5 except the variation in speed specified in Table 5.17.

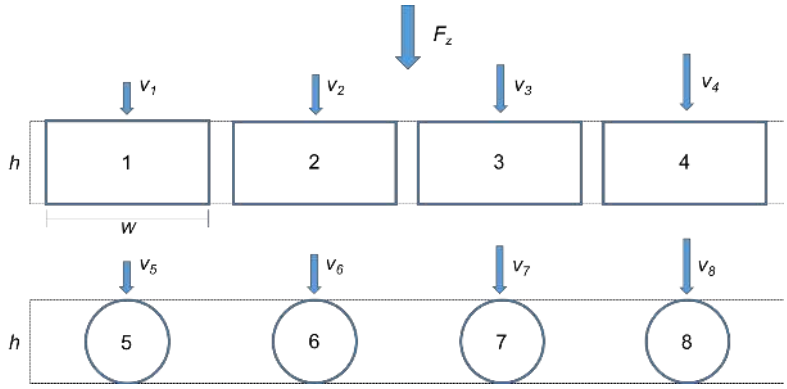

Figure 5.16: Impact speed loading scenarios

$h(mm)$	$W(mm)$	$v_1 = v_5(mm/s)$	$v_2 = v_6(mm/s)$	$v_3 = v_7(mm/s)$	$v_4 = v_8(mm/s)$
25	50	500	2500	5000	10000

Table 5.17: Impact speed geometrical parameters values

Results

Figure B.7 (in Appendix B) shows the force/displacement curves for the impact speed configurations. Figure 5.17 shows the bending performance results for the eight different loading scenarios.

Configurations 1 and 5 correspond to already tested scenarios and as such, in Figure B.7 (in Appendix B) the blue curves show an identical shape to the ones previously presented. The difference,

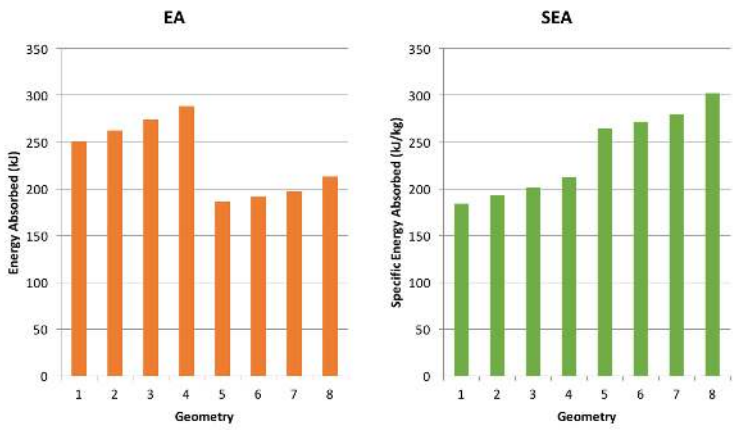

Figure 5.17: Impact speed bending performance metrics

however, appears when the impact speed is raised. The solution becomes increasingly noisier and an artificial (reason why it is not displayed in Figure 5.17) initial peak force is displayed. Nonetheless, and this is particularly visible in curves 2, 3, 5 and 6, when the speed increase does not introduce a significant amount of noise, with the advancement of the impactor, the force/displacement curve tends to the exact same solution which was obtained under a lower speed. The bending behavior is, therefore, the same, a statement which can be founded on Figure 5.17 which shows that with increasing speed, the energy absorption capacity of the beam only slightly increases due to some advantage during the integral calculation introduced by noise appearance. Overall the curve shape for the two different geometries is very similar, regardless the impact speed, which leads to the conclusion that a slower simulation, which can be easily validated through a quasi-static experimental test, is a valid model to study the bending performance of a beam even if the final purpose is the development of a design to sustain much higher impacts. In other words, all the conclusions retrieved on bending performance from all the previous geometries sets, are extensive to real impact situations. This analysis is valid based on the assumption that the strain rate effect does not alter significantly the stress-strain behavior of the material, which at still relatively low speeds [9], is a valid presumption.

5.3 Materials Analysis

In this section, a different approach is taken concerning the improvement of beam bending performance. Instead of varying the thin-walled beam geometry, the reference beam will be selected to perform a material comparative analysis. Several metals will be applied to the same geometry and their performances will be recorded. Once again the three-point bending model from Chapter 4 is used to compute the simulations.

Setup

The reference beam geometry is illustrated in Figure 5.1 and the geometrical dimensions are specified in Table 5.1. The simulation specifications are set according to Table 5.5 and the numerical model

validated in Chapter 4 is used. Three metal types were selected: steel, aluminum and titanium. A full list of the used materials (including the reference material DP250/450) and their respective properties is presented in Table 5.18, where ε_R represents the elongation at break, or fracture strain. As previously mentioned, the properties ρ, E and υ for all the steel grades referenced from [28] are approximated, since no exact values were available. These materials' stress-strain curves are available for consultation in Appendix A.

		$\rho(kg/m^3)$	$E(GPa)$	υ	$\sigma_y(MPa)$	$\sigma_{UTS}(MPa)$	$\varepsilon_R(\%)$
Steel	DP250/450 [28]	8000	210.0	0.30	250	450	32
	HSLA350/450 [28]	8000	210.0	0.30	350	450	27
	FB450/600 [28]	8000	210.0	0.30	450	600	17.5
	CP650/850 [28]	8000	210.0	0.30	650	850	13.5
	TWIP750/1000 [28]	8000	210.0	0.30	750	1000	37
	TWIP950/1200 [28]	8000	210.0	0.30	950	1200	20
Aluminum	Al2014-T6 [35][36]	2800	72.4	0.33	414	483	12
	Al5086-H32 [35][36]	2660	71.0	0.33	207	326	12.4
	Al6061-T65 [35][36]	2700	68.9	0.33	276	303	15
	Al7075-T62 [35][36]	2810	71.7	0.30	503	621	11
Titanium	Ti-6Al-4V [36][37]	4430	113.8	0.34	880	1009	11

Table 5.18: Materials list and respective properties (Adapted from [28][35][36][37])

Results

Figure B.8 (in Appendix B) shows the force/displacement curves for the material configurations. Figure 5.18 shows the bending performance results for the eleven different loading scenarios.

Beam	1	2	3	4	5	6	7	8	9	10	11
$Mass(kg)$	1.360	1.360	1.360	1.360	1.360	1.360	0.476	0.452	0.459	0.476	0.753
$F_{avg}(N)$	1671.6	1831.1	1807.9	2708.3	4300.3	4779.0	1416.3	1166.7	844.6	2407.9	2268.0
$Area(mm^2)$	1250.0	1250.0	1250.0	1250.0	1250.0	1250.0	1250.0	1250.0	1250.0	1250.0	1250.0

Table 5.19: Materials output data

The material list tested in this section is vast. Analyzing Figure B.8 (in Appendix B), the three metal groups, steel, aluminum and titanium, are easily identifiable by the initial slope of the respective force/displacement curves. Two properties vary accordingly to this slope difference: the density, ρ, and the modulus of elasticity, E. Since the initial deformation of the beam occurs in an elastic state, where by Hooke's Law (2.1), the stress is proportional to the strain, a larger E value for the steel grades justifies the higher slope registered in the force/displacement curves. Despite the different stress-strain curves (see Appendix A) which define this vast selection of materials, having different yield points, different elongations at break and other different properties, the force/displacement curve always presents an initial peak configuration followed by a sudden drop in load sustaining capability. This leads to the conclusion that the bending pattern does not depend on the material as much as it depends on the

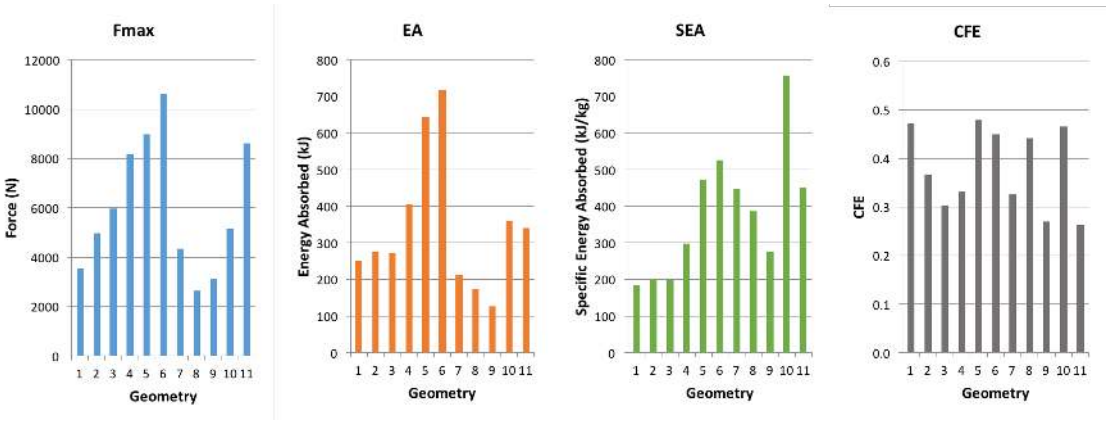

Figure 5.18: Materials bending performance metrics

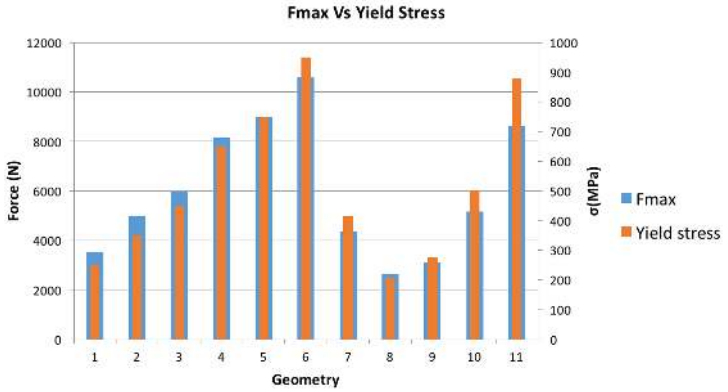

Figure 5.19: Reference beam reinforcements F_{max} Vs σ_y

cross-section geometry. The metrics, however, vary significantly depending on the material selection. Plotting the maximum force together with each material's yield stress (see Figure 5.19), it is clear that they are both highly related. The rectangular geometry exhibits an initial force peak, related to the starting deformation process. During this early stage of the simulation, a great portion of the solicited region of the beam is still in an elastic state. Requiring a higher stress to transition to a plastic state, the materials with higher σ_y demand a greater effort from the impactor to impose the same displacement. The TWIP grades have the highest yield points and ultimate tensile strength, which lead to a higher peak force and energy absorption. Nevertheless, the steel grades approximate density is much higher than the density of the aluminum. Combining a tensile yield strength over $500MPa$ with a low density which represents only 35% of a traditional steel, the Al7075 grade has the highest SEA value by a margin 44% when compared to the next best performer, the TWIP950/1200. The CFE parameter does not show any evident patterns, mostly varying between low values 0.3 and 0.5. This small fluctuation is consistent with the hypothesis that the crash efficiency is more influenced by geometrical factors rather than material ones. The titanium grade is not an appropriate choice due to the nature of its stress-strain curve (see Appendix A). Despite its high yield point and ultimate tensile strength (over $1000MPa$), the titanium's elongation at break is 11% which induces a rapid decrease in load sustaining capacity, thus diminishing the energy absorption and the crash force efficiency. When comparing aluminum and steel, the deci-

sion must weigh some important factors: with the exception of the TWIP grades, all aluminums have a greater SEA value. However, this is followed by a lower EA, which ultimately leads to a choice between mass (aluminum) reduction or bending performance (steel); the manufacturability of the stronger steels, such as the TWIP grades, poses intricate challenges connected to those materials' high yield points; the price of each material. The aluminum grades are appealing due to their lower mass and higher specific energy absorption, but the raw material price is usually higher than steel's.

In an academic point of view, excluding the external, industry-related factors, the selection of the best material, in this case, is highly dependent on how important it is to keep the mass low or, on the other hand, having the greatest energy absorption possible. The choice will always recall on either the Al7075 or the TWIP950 grades. In order to clarify the evaluation criteria and to select the best solutions from the extensive geometrical and material analyzes done until this point, in the following section a selection tool is designed and applied to the present study.

5.4 Selection Tool

Determining the best solution off all the tested geometries and materials, is not a straightforward process. Actually, depending on the selected criteria, there may be more than one "best solution". This section focuses on the development of a selection tool to weigh the several criteria and, according to the results obtained through Chapter 5, to choose which configuration brings a better improvement to the reference beam's overall performance.

5.4.1 Criteria Definition

The first step in the tool design process is the definition of the criteria under which the performance of the tested beams will be evaluated. Many factors affect the choice of a specific configuration. Manufacturing feasibility and cost are two of those factors, and despite being key elements in the decision process which leads to a final design, these are parameters hard to evaluate and cannot be extracted from the output results obtained via a three-point bending model. For that reason, they will not be considered in this section. If the best configuration according to the selection tool proves itself to be unfeasible or to costly, the tool will also evaluate and provide an ordered list with the remaining tested solutions. Any other configuration may also be analyzed and compared using this tool, provided the performance metrics indicated in Chapter 3 are obtained via the model validated in Chapter 4.

Three criteria are selected to evaluate the beams' performance:

- **Mass** – the beam's mass, M, is a key factor in any project design. With the increasing concerns surrounding environmental sustainability, the mass of the vehicle must be kept as small as possible;
- **Volumetry** – equivalent to the smallest rectangular area where the cross-section can be fitted, A, is also a very important parameter due to the space unavailability inside the door compartment. Several components, such as the window, the window elevator, the stereo system, among others, limit the room available for the beam installation;

- **Bending Performance** – evaluating the bending performance of a beam has been the main goal of this thesis until this point. Four different metrics were used to assess each configuration. However, these parameters are mathematically connected and, in order to reach a comparable magnitude for the bending performance, they are not all required. Only the EA and CFE metrics will be considered. The SEA value is given by a relationship between EA and the beam's mass, which is already considered in the mass criterion. Using this parameter to evaluate the bending performance as well would become redundant. The F_{max} parameter is accounted for in the crash force efficiency calculation, which translates a more comprehensive measure of the force distribution, rather than a simple value which, alone, transmits little information on the bending performance. A new dimensionless metric named bending performance, BP, is created and is given by equation (5.1).

$$BP = 0.8\frac{EA_i - EA_{ref}}{EA_{ref}} + 0.2\frac{CFE_i - CFE_{ref}}{CFE_{ref}} \tag{5.1}$$

  EA_i and CFE_i are the EA and CFE values of any tested beam whose BP value is being calculated. The BP parameter is a comparative metric measured in relation to a well-known reference. The BP of the reference beam will, naturally, be equal to zero. The comparative nature of this tool will be further detailed in the following sections. The ponderation between the two parameters, clearly in favor of the EA metric, is based on the main function of the side intrusion beam, which is to absorb the maximum impact energy possible. However, doing it with a better crash efficiency, leads to an overall better performance. Other ponderation factors could be selected.

5.4.2 Tool Design

This selection tool is no more than a comparative mechanism, hence a reference is needed. That reference is no other than the reference beam. Each configuration's performance metrics will be compared in magnitude to the ones obtained for the reference beam, creating three dimensionless variables, each corresponding to one of the criteria previously described (mass, volumetry and bending performance). A ponderation of these three variables will result in a final score for each beam which will ultimately determine the best solution. The weight of each criteria in this final ponderation is determined by user input and is crucial to the final output. Different weight distributions lead to different solutions, hence three scenarios will be studied, each one highlighting the importance of a particular criterion. In Table 5.20 the metrics correspondent to the reference beam three-point bending simulation, required by the criteria specified in section 5.4.1 and obtained in the simulations ran in section 5.1 are presented. Table 5.20 also includes the same metrics for the simulation of the hexagonal and quadrangular (configurations 2 and 6 of Figure 5.3) cross-section beams in section 5.2.1, section 5.2.1.

	$M(kg)$	$A(mm^2)$	$EA(kJ)$	CFE
Ref. Beam	1.360	1250.0	250.61	0.47
Hexagonal	0.666	541.3	175.48	0.77
Quadrangular	0.880	1714.2	256.93	0.66

Table 5.20: Required metrics

The BP metric is already dimensionless, and is computed from parameters EA and CFE by equation 5.1. An equivalent process leads to the creation of two other dimensionless variables, ΔM and ΔA, given by equations (5.2) and (5.3) respectively, which represent a comparative measure of any test result metrics to the reference beam's equivalent parameters.

$$\Delta M = \frac{M_i - M_{ref}}{M_{ref}} \tag{5.2}$$

$$\Delta A = \frac{A_i - A_{ref}}{A_{ref}} \tag{5.3}$$

The indicatives i and ref refer to a particular studied beam and to the reference beam respectively. Using equations (5.1),(5.2) and (5.3), the tool metrics are computed and presented in Table 5.23

	ΔM	ΔA	BP
Hexagonal	-0.510	-0.567	-0.114
Quadrangular	-0.353	-0.500	0.098

Table 5.21: Selection tool metrics for the quadrangular beam

The three metrics displayed in Table 5.23 show, for the quadrangular beam, a negative evolution in both mass and volumetry and a positive evolution in the bending performance. These results state that in all three criteria the quadrangular section beam is better than the reference beam. The hexagonal beam, however, despite registering a greater decrease in mass and volumetry, it presents a negative evolution in the bending performance. Determining if this beam is better or worse than either the reference or quadrangular beams, requires a ponderation between the three metrics displayed in Table 5.23. Combining these metrics and reaching a final score for each configuration is the goal of the following section.

5.4.3 Evaluation Scenarios

$$FS = -C_1\Delta M - C_2\Delta A + C_3 BP \tag{5.4}$$

Equation (5.4) calculates the final score, FS, for each configuration, based on the the tool metrics. Coefficients C_1, C_2 and C_3 have an individual value between 0 and 1, and must respect equation (5.5). C_1 and C_2 coefficients are preceded by a negative, $-$, signal since a negative evolution from both mass and volumetry is seen as positive contribute to the final score.

$$C_1 + C_2 + C_3 = 1 \tag{5.5}$$

Attributing values to these constants sets the weight of each criterion on the final score calculation. Let us consider three different scenarios presented in Table 5.22.

The first scenario proposes an even distribution for each metric, i.e., a relative improvement regarding the beam's mass contributes equally to the final score as an identical relative gain in bending performance, for example. This is the case when all the three criteria are crucial to the beam design.

Scenario	C_1	C_2	C_3
1	0.33	0.33	0.33
2	0.60	0.30	0.10
3	0.20	0.30	0.50

Table 5.22: Ponderation scenarios

The second scenario suffers a weight shift from the bending performance to the beam's mass. This is the case when the most crucial factor is the component's mass. It is seen as an extra safety system, whose installation should provide some more safety to the vehicle passengers, but which may not compromise the vehicle mass target.

The third and final scenario is the opposite of the previous case. Here the main concern is to improve the beam bending performance and a compromise may be made, forgiving a mass increase if necessary.

In all scenarios the C_2 coefficient is kept approximately constant. This is because the space available for the beam is usually highly restricted. Not existing great room for expansion, an increased volumetry will always be penalized by a 0.3 coefficient. Applying equation (5.4) to the metrics of Table 5.20 and considering the three scenarios of Table 5.22, six different final scores are obtained (Table 5.23).

Scenario	1	2	3
Hexagonal	0.465	0.321	0.215
Quadrangular	0.372	0.317	0.269

Table 5.23: Final score for hexagonal and quadrangular beams in three different scenarios

The final score, despite being a dimensionless figure, provides a comparative measure of how better a beam is relatively to the reference beam, whose FS will always be zero, and to every other beam analyzed with the same tool. These results show, firstly, that considering any scenario, either the hexagonal or the quadrangular configurations are always a better solution than the reference beam. The results also show, that determining the best final score is dependent on the considered scenario. If with an even coefficient distribution, the FS of both beams is similar, the metrics which contribute to this score differ from each other. The quadrangular beam has a better bending performance than the hexagonal configuration, but also a higher mass and volumetry. In scenario 3 where the mass increase is accepted as compromise for a better bending performance, the quadrangular beam has the advantage. However, in scenario 1, where the solution mass is crucial, the hexagonal beam takes the advantage due to its 51% mass reduction, despite having a lower BP than the quadrangular and reference beams.

This analysis on two of the tested geometries sampled the design and workflow of this selection tool. Next, the tool is applied to all the tested geometries and materials and, considering the same three scenarios presented here, a final selection is made based on the highest final scores. These beams will then be installed in a vehicle model and tested under crash conditions.

In this chapter, 32 different geometries and 11 different materials were tested. Gathering all the results, introducing them in the selection tool and considering three different scenarios, three final scores for each one of the 42 different configurations (1 of the 11 materials was applied to all the 32 geometries)

are obtained. In Table 5.24 the top three final scores are presented for each geometries set in each of the three different scenarios.

		Scenario 1		Scenario 2		Scenario 3	
		Config.	FS	Config.	FS	Config.	FS
Regular Polygons	1^{st}	7	0.469	8	0.404	8	0.395
	2^{nd}	2	0.465	5	0.331	6	0.269
	3^{rd}	5	0.430	2	0.321	5	0.260
Geometrical Proportions	1^{st}	6	0.587	3	0.511	3	0.461
	2^{nd}	3	0.563	9	0.469	9	0.411
	3^{rd}	9	0.539	6	0.451	8	0.395
Reference Beam Reinforcement	1^{st}	5	0.009	5	0.305	5	0.507
	2^{nd}	6	0.000	4	0.111	4	0.394
	3^{rd}	3	-0.155	3	0.056	2	0.239
Geometrical Expansion/Reduction	1^{st}	4	0.636	4	0.356	1	0.206
	2^{nd}	1	0.518	1	0.343	5	0.199
	3^{rd}	5	0.430	5	0.296	4	0.157
Open Sections	1^{st}	2	0.467	2	0.420	2	0.386
	2^{nd}	1	0.426	1	0.339	1	0.281
	3^{rd}	4	0.357	4	0.171	5	0.092
Thickness Variation	1^{st}	1	0.304	4	1.262	4	2.594
	2^{nd}	2	0.000	3	0.371	3	0.857
	3^{rd}	3	-0.389	2	0.000	2	0.000
Materials	1^{st}	10	0.425	6	0.492	6	0.739
	2^{nd}	8	0.375	5	0.420	5	0.630
	3^{rd}	7	0.372	10	0.333	10	0.305

Table 5.24: Final scores for parametric analysis

Some general patterns emerge from the vast data recorded and computed throughout Chapter 4. Scenarios 2 and 3 tend to select approximately the same beam configurations, despite attributing different final scores. The greater changes are observed in scenario 1 where the weight of the mass criterion plays a crucial role in evaluating the available solutions.

5.5 Side Intrusion Beam Performance

In this final section, the overall performance of the tested solutions for bending performance improvement is presented. First, the main conclusions relatively to each configurations set are summed up. The configurations tested in section 5.2.7 are not considered since their purpose was to study the effect of the test velocity on the bending performance of the beam, and not to test a new solution to improve that same bending performance. Finally, the top results of Table 5.24 are analyzed.

- **Regular Polygons** – Increasing the number of sides in a close section leads to both a lower EA and a greater independence on the load direction. The number of edges in a beam is deeply connected with the development of plastic hinges which ultimately lead to a structural plastic collapse.

- **Geometrical Proportions** – The thinner the geometry, the better the bending performance. This is a consequence of a greater alignment of the geometry with the loading direction. The development of plastic hinges is delayed, i.e, a greater displacement is required to induce plastic collapse. By opposition, a wider geometry absorbs less energy with a bending behavior denoted by its initial peak force, followed by a sudden drop in load sustaining capacity.
- **Reference Beam Reinforcement** – Reinforcements introduction leads necessarily to a mass increase. Nevertheless, they always prove to enhance the beam's bending performance. Vertical, load aligned reinforcements are preferable since they are more effective in increasing the beam's rigidity.
- **Geometrical Expansion/Reduction** – SEA values remain constant through both expansion and reduction processes, thus this is a proportional way of increasing or decreasing the beam's bending performance, based on the available space and mass requirements. Note that CFE values decrease with size which means the abruptness of the deformation process is higher for bigger solutions.
- **Open Sections** – Open sections show SEA and CFE values generally higher and a much more smooth force/displacement curve is recorded. Their open side allows for a greater deformation before the development of plastic hinges, delaying the drop in load sustaining capacity. Opening a section leads to a slight drop in energy absorption followed by a much greater drop in mass and peak force. These results show the potential of open sections. With much lower forces involved, similar energy absorption capacity is obtained.
- **Thickness Variation** – Thickness increase inevitably leads to both a greater mass and a better bending performance. If mass is not a critical factor, this is certainly the best way of increasing the performance of a beam under lateral impact.
- **Materials** – The higher the yield stress of a material, the higher are the EA and F_{max} values. This means that the increase in bending performance is a consequence of having larger forces involved in the deformation process, rather than having a transformation in bending pattern of the beam. On the contrary, the beam's material shows a marginal influence on the pattern of the force/displacement curve. All materials were tested on the reference beam and, despite the wide variety of densities, yield stress and modulus of elasticity values, all output curves displayed the initial peak force followed by a sudden drop in load sustaining capacity. This leads to the conclusion that each bending pattern is characteristic of a certain cross-section geometry and not of the applied material.

Based on Table 5.24, it is possible to extract the best overall final scores for each of the three scenarios. That information is gathered in Table 5.25.

Both the final scores and selected configurations vary significantly according to the studied scenario:

- **Scenario 1** – low mass solutions are preferred and for that reason smaller geometries from the proportion and reduction analyzes present a higher FS;

	Scenario 1			Scenario 2			Scenario 3		
	Set	Config.	FS	Set	Config.	FS	Set	Config.	FS
1^{st}	Expansion/Reduction	4	0.636	Thickness	4	1.262	Thickness	4	2.594
2^{nd}	Proportions	6	0.587	Proportions	3	0.511	Thickness	3	0.857
3^{rd}	Proportions	3	0.563	Materials	11	0.492	Materials	11	0.739

Table 5.25: Overall best final scores

- **Scenario 2** – an even weight distribution through all the criteria leads to the most balanced solutions. The best option in this scenario is the $5mm$ thick beam;
- **Scenario 3** – here the bending performance is the key factor and for that reason, large thickness and strong material options score the highest FS values. The $5mm$ thickness option is, once again, the best solution. The reason why it does not appear in the top 3 of scenario 1 is linked to the high mass increase associated with a larger thickness.

Finally, when it comes to selecting the beam solutions to be tested in a crash simulation, it is more logical to look at the scenario 3 results, since the mass and volumetry are inputs for the simulation and the aim of Chapter 6 is to study the connection between the output of a slow three-point bending test and fast impact event. Since the first and second solutions of scenario 3 are both related to thickness increase, the third option, introduction of a TWIP950/1200 steel grade, is considered alongside the $5mm$ thick thin-walled beam.

Before advancing to the following chapter, it is important to note that all the tested geometries and materials sets produced at least one, and in many cases several more, solutions with positive final scores for every scenario. This means that all the diverse parametrical variations, such as a thickness increase or the introduction of a vertical reinforcement or a change in the steel grade applied on the beam, led into improvements in bending performance. This parameters were independently tested, but together, can bring even greater improvements to the beam solution. The pursuit of this study extends beyond the scope of this thesis. However, the study of different configurations becomes quite facilitated by the standard procedure developed in this thesis. In a future work context, this may certainly be a relevant study matter.

Chapter 6

Complete Model Crash Test

This chapter covers the final objective of this thesis, which is the study of the relationship between an improvement in bending performance of the side intrusion beam and the consequent increase in passengers safety. Regulatory agencies require the placement of dummies inside the vehicle to properly assess the probable damages from a side impact. This chapter, however, will proceed to a number of simplifications in order to decrease the simulations' cost:

- No dummy model is placed inside the vehicle;
- The moving deformable barrier, used in the side impact collision simulation, is considered rigid;
- A detailed Geo Metro model provided and validated by the National Crash Analysis Center (NCAC) [38] is used. The passengers compartment is not modeled, hence a conservative approach is taken since all the missing elements are also responsible for some energy absorption.
- No validation is performed on the vehicle numerical model, assuming that the impact simulations on the Geo Metro provide an accurate description of real crash events.

The lack of a dummy model limits the damage information that may be retrieved from this numerical model. Thus, in order to analyze the behavior of different beams, a comparative study will be conducted in this chapter. First, the vehicle is crashed with the reference beam. Then, both configurations selected in Chapter 5 are tested and, finally, a no-beam configuration is also tested. These several analyzes will show, first, how an improvement in bending performance relates to the full vehicle crash behavior, and second, what role the reference beam would play, when compared to a no-beam configuration.

The force/displacement curve will not be used to assess energy absorption since there is no exact way of recording which amount of force is directly applied on the beam. Instead, a displacement analysis on the door's inner panel will be performed to understand which solutions predict a smaller intrusion from the external object into the passengers compartment. Despite being far from the required damage assessments, this method provides a simple way of testing, in a crash event, how a more rigid beam behaves and what impact that behavior has on the intrusion of an external object. This is a very limited approach, but once again, the purpose of this chapter is to confirm wether or not an improved beam configuration displays a better performance in a crash scenario.

Two different crash scenarios will be tested. The first, the side impact collision test, studies the vehicle response to a lateral impact of an average road car. A moving deformable barrier (as it is called; in this case the barrier is considered rigid) simulates the impacting vehicle. The collision occurs perpendicularly to the vehicle longitudinal axis. The setup for this configuration is based on the ECE R-95 regulation [23]. The second, the side pole test, studies the vehicle response to an impact against pole-like structures, such as trees and signposts. In this configuration, the vehicle is led into a static and rigid pole with an angle of 75^o between the impact direction and the vehicle longitudinal axis. The setup for this test is based on the Euro NCAP procedure [25].

Once all the tests are completed, conclusions on the importance of using a side intrusion beam and on the effect of using an improved solution will be withdrawn. The beams with a higher bending performance are expected to prevent more effectively the intrusion of the door into the passengers compartment, absorbing a greater amount of energy during the same imposed displacement.

6.1 Side Impact Collision

In this section, the focus relies on the side impact collision test which simulates side crash between an average road car and the tested vehicle. The corresponding physical procedure is required for achieving vehicle homologation. Thus, the european regulation, ECE R-95 [23] will be used as a reference to build the numerical setup. The results and conclusions will be analyzed from the door's inner panel displacement.

6.1.1 Crash Test Setup

A crash always involves two different objects colliding against one another at high speeds. These two objects are, in the case of a side impact collision test, the studied vehicle and the moving deformable barrier.

Geo Metro

A Geo Metro detailed model, MetroD, is used to perform the crash tests. This model has been developed by the NCAC [38] of The George Washington University under a contract with the Federal Highway Administration and NHTSA of the United States Department of Transportation. This model is composed by 193200 finite elements, including 1D, 2D and 3D configurations. It is validated for crash analyzes ran on the solver LS-DYNA. This solver is different from RADIOSS, but it is also designed for crash & safety simulations. HyperCrash is able to convert the LS-DYNA file into an equivalent RADIOSS extension, and the model is assumed to remain valid. Several models are provided by the NCAC [38], but the Geo Metro was selected due to its similar dimensions to the initial Be model. The Geo Metro finite element model, illustrated in Figure 6.1 has the dimensions presented in Table 6.1, where M_m is the mass of the vehicle.

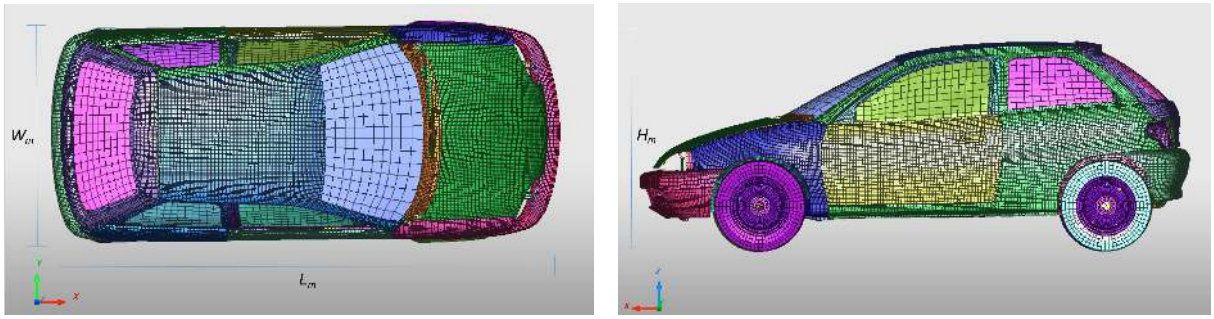

(a) Top view (b) Side view

Figure 6.1: Geo Metro finite element model

	$L_m(mm)$	$W_m(mm)$	$H_m(mm)$	$M_m(kg)$
Geo Metro	3750	1550	1430	592

Table 6.1: Geo Metro main dimensions

Moving Deformable Barrier

A simplified version of the moving deformable barrier described in the ECE R-95 regulation is considered. As previously mentioned, a rigid structure will be used, having a total mass of $M_{mdb} = 950kg$, greater than the vehicle's. The conventional configuration for a moving deformable barrier, used during the homologation process, is presented in Figure 6.2. The regulation details several technical specifications regarding the impactor's material and its crushing pattern, or even the location of the center of gravity for the global structure. However, in order to decrease the model's complexity and its subsequent computational cost, a simpler configuration is adopted. The mechanical properties of the material used are irrelevant since the barrier is considered a rigid body. For this reason, the simplest formulation, purely elastic material, is used to define the material, whose density must be calculated in order to provide the barrier the necessary mass, M_{mdb}. The impactor's dimensions are those used in the regulatory test procedures, and all the barrier's mass, M_{mdb}, is concentrated on the impactor. An impact velocity, v_i, is applied to the impactor and the crash results are observed. The barrier is modeled as a rigid shell and 2D four nodes elements mesh is applied. A Belytschko-Tsay formulation (see [32]) is selected with one integration point (reduced integration). In Figure 6.3 this simplified configuration is presented, and the respective dimensions can be consulted in Table 6.2. The rigid consideration is far from a real scenario, but since this study does not pretend to confirm wether a certain solution would or not guarantee vehicle homologation (that would require the full vehicle model and an appropriate dummy), this conservative approach will serve as a comparative tool between different solutions.

	$L_{mdb}(mm)$	$W_{mdb}(mm)$	$H_{mdb}(mm)$	$a_{mdb}(mm)$	$b_{mdb}(mm)$	$M_{mdb}(kg)$
Impactor	200	1500	500	60	250	950

Table 6.2: Moving deformable barrier simplified model's main dimensions (Adapted from [23])

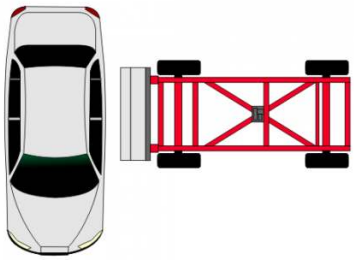

Figure 6.2: Conventional configuration of a moving deformable barrier [39]

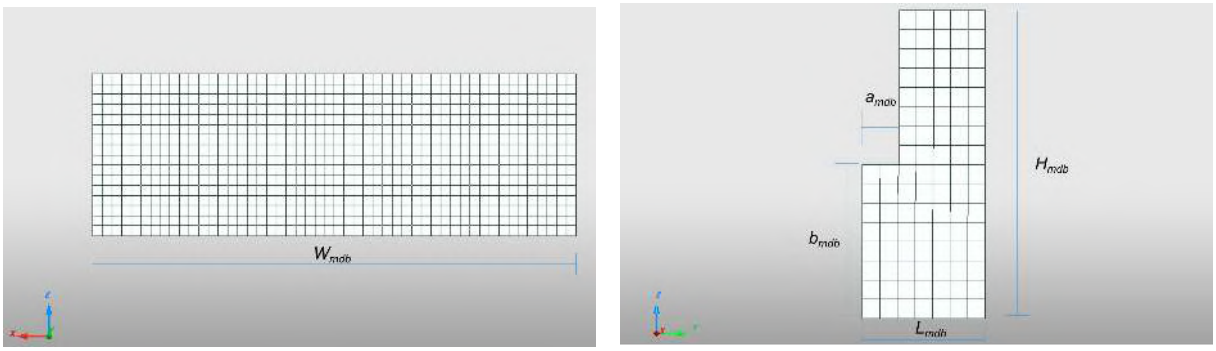

(a) Front view (b) Side view

Figure 6.3: Moving deformable barrier finite element simplified model

Side Intrusion Beam

By the end of Chapter 5, two beam configurations were selected:

- The $5mm$ thick rectangular beam, $Beam5$, with a DP250/450 steel grade;
- The TWIP950/1200 steel grade beam, $Beam950$, applied on the reference beam's rectangular geometry.

These two configurations, together with the reference beam, are illustrated in Figure 6.4. Despite their cross-sections remaining constant, the beams' length must be adapted to the Geo Metro's door, increasing from $L = 800mm$ (see Table 5.5) to $L = 1000mm$. A fourth analysis will also be considered, under a scenario where no side intrusion beam is used. In the other three scenarios, the beam is rigidly fixed to a support at both its endings and each of the supports is attached to either A or B pillars. This configuration is illustrated in Figure 6.5.

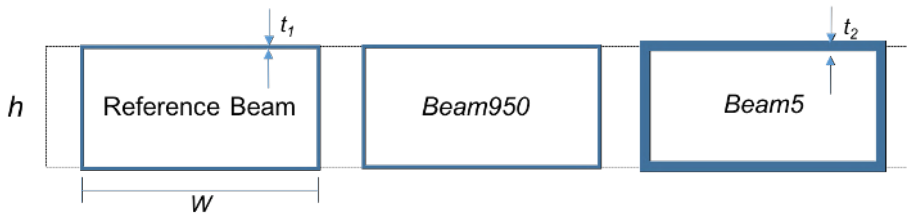

Figure 6.4: Geometries selected from Chapter 5

$h(mm)$	$W(mm)$	$t_1(mm)$	$t_2(mm)$
25	50	1.5	5

Table 6.3: Parameters of Figure 6.4

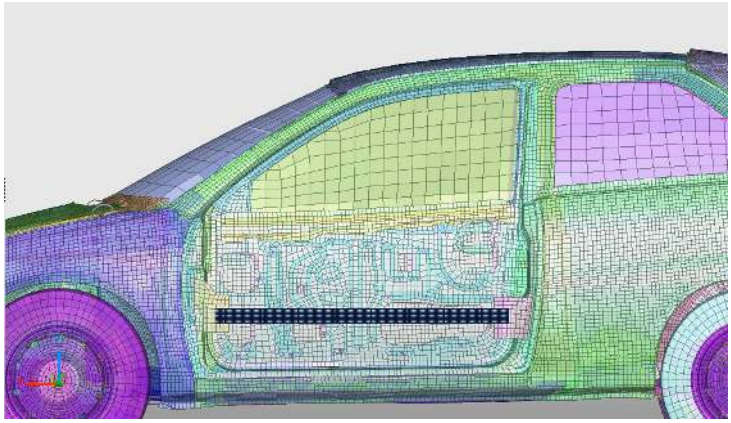

Figure 6.5: Side intrusion beam installed inside the door

Impact Configuration

As seen in Chapter 3, HyperCrash is the appropriate tool from the HyperWorks set to build the numerical setup for a crash event. Some key setup steps should be considered:

- **Initial velocity** – an initial impact speed of $v_i = 13888.9mm/s$ or $v_i = 50km/h$ is applied to the impactor in the negative direction of the y axis. This vector is perpendicular to the longitudinal axis of the vehicle, which has an initial zero velocity. However, the vehicle is standing on a numerical floor and, once the crash occurs, the vehicle will accelerate in the impact direction, always considering the laws of friction.

- **Initial positioning** – despite the fact that in a real crash test the moving deformable barrier needs to be accelerated through a long distance to achieve v_i, in the simulation setup, the impactor is placed as close as possible to the vehicle, without any contact activation, in order to avoid the computational cost associated to the time interval between the beginning of the simulation and the actual crash. The median plane of the impactor must be coincident to the front seat R Point. The R Point is the theoretical location for the passenger's hip point considered during the design phase. Since the location of the R Point is unknown (due to the unavailability of the passengers compartment model), it will be assumed as being $135mm$ away from the B pillar to the front of the vehicle.

- **Simulation time** – the crash event will be studied for the first $0.06s$. This period is long enough to observe a considerable displacement and limits the computational cost to acceptable values.

- **Time history** – the door displacement in the impact direction (y axis) is measured discretely through a selected number of nodes displayed throughout its inner panel. These nodes' locations is illustrated in Figure 6.6. Five levels are identified, $L_{1...5}$, whose values, presented in Table

6.4, represent their distance in relation to the ground. The H-point height is based on an estimation made by [40] for a similar vehicle. The d value in the same table is the approximate measured distance between each of the eight consecutive points (except in level five (L5), where there are only four points) which compose each level. The number of data nodes per level was selected based on a compromise between solution accuracy and data processing cost. Eight nodes per level are sufficient to provide a smooth description of the panel's deformation pattern. A time history is created (as seen in Chapter 3) and associated to these nodes, recording their displacement during the entire simulation.

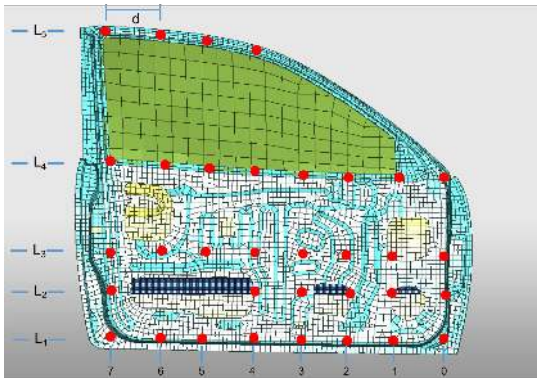

Figure 6.6: Selected nodes from the inner panel

	Location	Distance from ground(mm)
L_1	Sill top	360
L_2	Occupant H-point	500
L_3	Mid-door	640
L_4	Window sill	900
L_5	Window top	1300
d	–	140

Table 6.4: Parameters of Figure 6.6

The final setup is illustrated in Figure 6.7. All models are developed with the explicit non-linear finite element code RADIOSS.

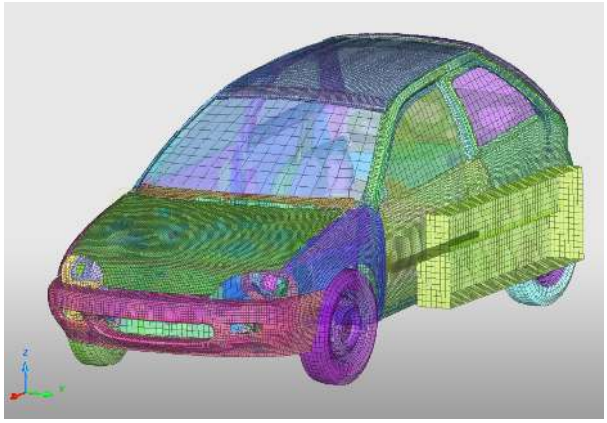

Figure 6.7: Side impact collision global setup

6.1.2 Crash Results

Figure 6.8 shows the inner panel displacement (in the impact direction, (y)) curves for the five levels and for the four tested solutions. The total simulation time is divided into three equally distant intervals of $0.02s$ each and the displacement curves at the end of each interval are shown. In Figure 6.8 the graphic results observed in HyperView at each time step for $Beam5$ configuration are also shown. Despite

the impact being directed towards the negative side of the y axis, the graphics of Figure 6.8 show the negative displacements caused by that impact as being positive.

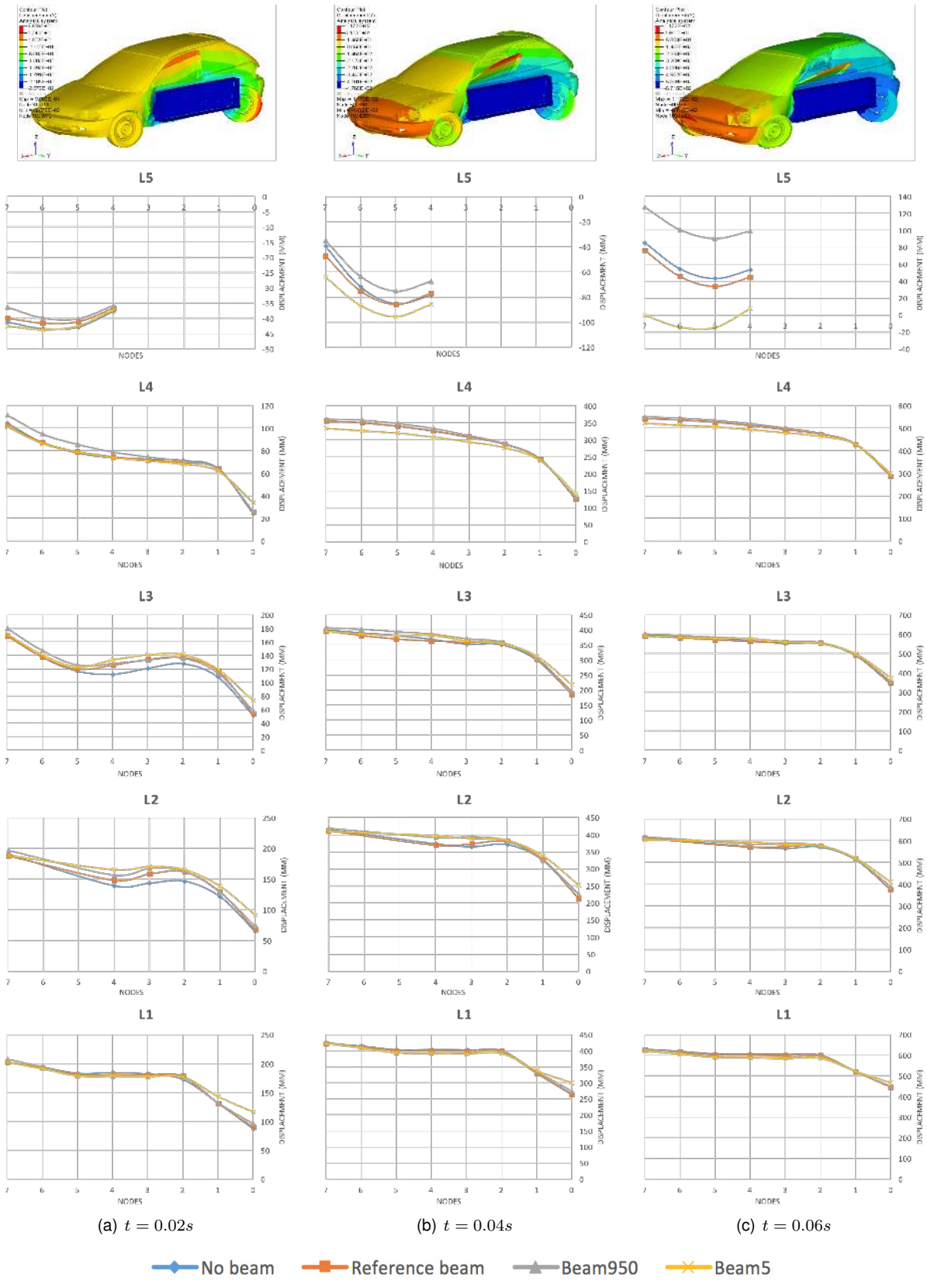

(a) $t = 0.02s$ (b) $t = 0.04s$ (c) $t = 0.06s$

Figure 6.8: Inner panel global displacement under a side impact collision test

Looking at the displacement results, two comparative analysis can be performed, either by level or by time step. Starting by the different levels, it is clear that the major differences between the several beam solutions occur in levels two (L2),three (L3) and five. Level one (L1) is almost insensible to the beam selection and level four (L4) shows a slight improvement introduced by $Beam5$ with $Beam950$ showing the highest displacement. The results obtained for level one derive from the proximity to the sill which is connected directly to the vehicle's floor. For this reason the energy absorbed in this area will depend much more on the sill and floor's mechanical properties and design, rather than on the selected solution for the side intrusion beam. However, close to the A pillar (node 0), a significant displacement variation is measured. The better the bending performance of the used beam, the higher the deformation of the panel in this region. This result contradicts the premiss which states that a higher bending performance should result in greater safety levels for vehicle passengers. Since proving this premiss is a major goal of this thesis, a deeper analysis is required in order to fully understand what is the root cause of this unexpected behavior. Levels two and three show once again the same phenomenon, but this time throughout the whole beam. This is specially visible in the first time step ($t = 0.02s$) results. In level two, for example, node 0 of $Beam5$ has a displacement 40% higher than the no beam scenario, and node 4, right in the middle of the panel, also displays a greater displacement by 19%. Level five shows a peculiar behavior since the displacement occurs in a direction opposite to the impact. This is visible in the HyperView images of Figure 6.8 and leads to the conclusion that, at least through a direct contact, level five will not be responsible for any damage on the vehicle passengers. When the impact occurs, during an initial period, the vehicle components deform themselves and absorb part of the impact energy. However, part of that energy is transmitted to the impact vehicle in a kinetic form and the vehicle accelerates. This imprinted velocity, which is either translational or rotational, is accounted for the displacement measurements presented in Figure 6.8. As a consequence, as time advances, the measured displacement becomes less representative of the panel intrusion. Before moving to a displacement analysis in a local referential, let us observe the bending pattern of the three different solutions (the no beam solution will not be commented because no beam is tested), at $t = 0.02s$, when the maximum divergences are noted.

$Beam5$ of Figure 6.9 shows a clearly inferior deformation in relation to the other two solutions. The reference beam presents the higher deformation, visually noticeable by the greater decrease in the cross-sectional area in the bending region and by the shorter angle between the two beam sections separated by the bending axis. $Beam950$ displays a bending pattern close to the reference beam, being evident the development of plastic hinges in the main solicited area. This phenomenon is consequence of reaching the material's maximum bending resistance moment equivalent to a fully plastic state. This is particularly relevant since it means that the greater displacement recorded for $Beam5$ is not a consequence of its lower deformation. $Beam950$ is deformed into a fully plastic state close to the reference beam, absorbing more energy during the bending process but still leading to a greater overall displacement. If the initial results could suggest that the improved solutions were not adding any energy absorption capability since they suffered a greater displacement, now that hypothesis is proven wrong by the deformation pattern of $Beam950$. If energy absorption is not, at least directly, related to the unexpected results of Figure 6.8,

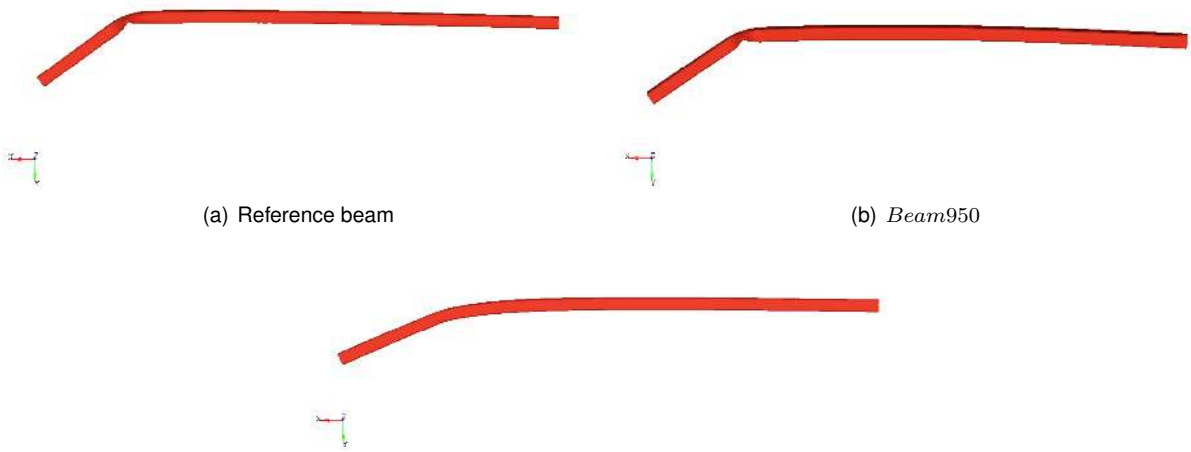

(a) Reference beam

(b) $Beam950$

(c) $Beam5$

Figure 6.9: Side intrusion beam deformation pattern at $t = 0.02s$

some external, so far not considered factor must be the source of this behavior.

Figure 6.10 shows the displacement patterns for the four solutions in the same time steps used in Figure 6.8, but instead of using the global referential, a local moving axis system is created which, for each level, measures the displacement from the straight line which connects nodes 0 to 7. In other words, the x axis is attached to nodes 0 and 7, the z axis remains constant and the displacement is measured normally to the plane formed by the two axes. The resulting displacement curves can be obtained through the results of Figure 6.8, by subtracting to each node's displacement the coordinate of the straight line which connects the first and last nodes' displacement value. Logically the extreme coordinates belong to the local referential's x axis, hence having a null local displacement. Level five is not considered in Figure 6.10 since node 7 is not available, and also because, as previously mentioned, the door displacement at this level is opposite to the impact direction, moving away from the passenger, thus not causing any damage through direct contact.

A completely different perspective is given by the graphics of Figure 6.10. The first observation is that, in the local referential, there is a direct relationship between bending performance and panel deformation. Through all levels and time steps, the reference beam always displays a greater displacement than $Beam950$, and $Beam950$ always undergoes a greater deformation than $Beam5$. The no beam solution, however, has a variable deformation pattern, frequently better than some of the beam configurations. First, it is important to understand why the better performing beams exhibited a larger displacement in the global referential and now, in the local referential, show a better bending pattern. When from a local perspective, $Beam5$ has the best crash performance, which was the expected result for its overall behavior, since this is a solution improved from the original reference beam. The local displacement measurement translates the pure panel deformation, i.e., how much its configuration changes due to the crash event. From this angle, a more rigid beam, such as $Beam5$, will prevent that deformation by requiring a larger energy/force to bend. Since the applied force is derived from the barrier's momentum, which does not vary between simulations, a greater rigidity will lead to a lesser deformation. This conclusion is clear in every graphic of Figure 6.10. Nevertheless, this lower local deformation is not followed

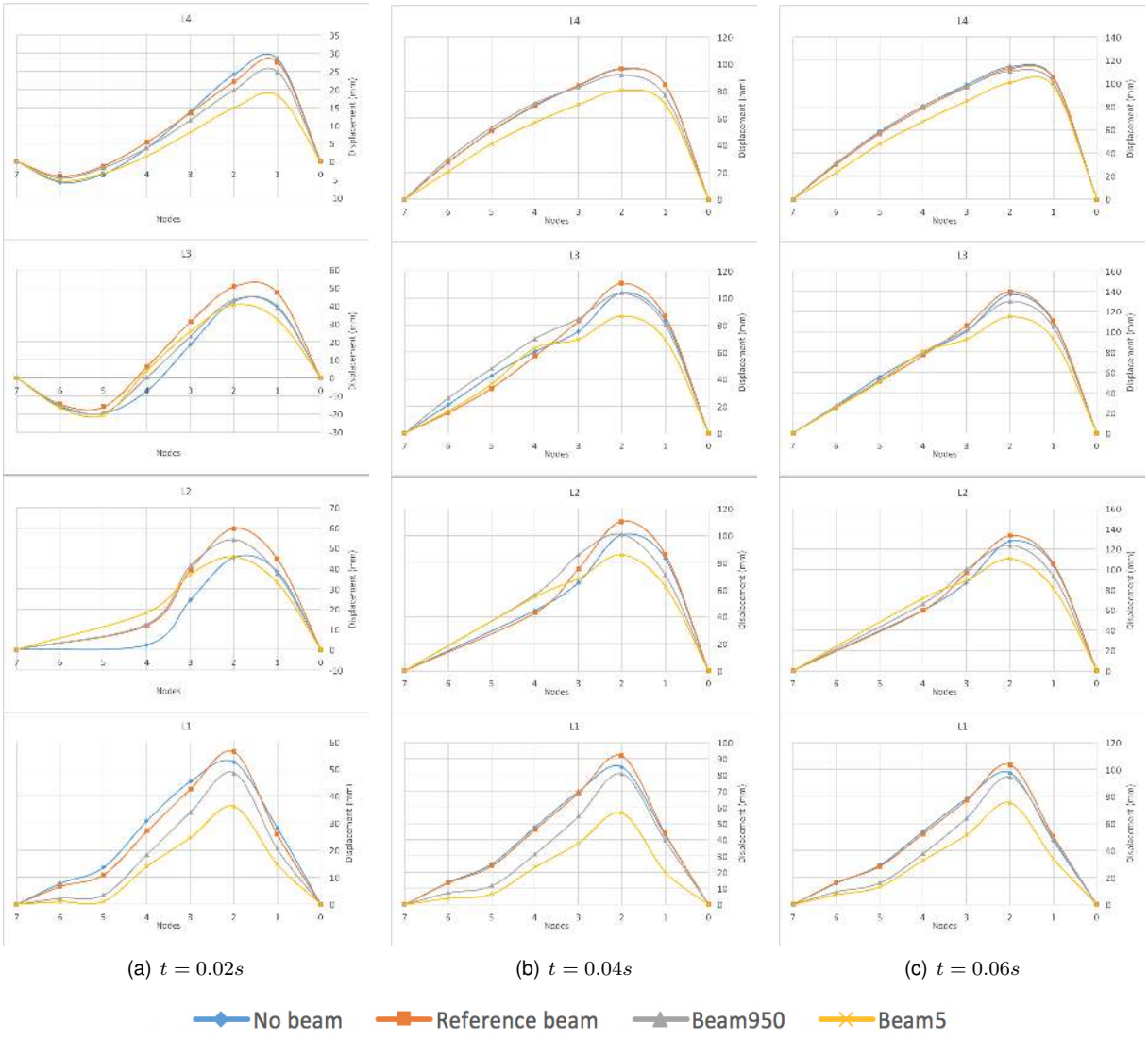

(a) $t = 0.02s$ (b) $t = 0.04s$ (c) $t = 0.06s$

Figure 6.10: Inner panel local displacement under a side impact collision test

by the global results. Two factors are responsible for this unexpected and unwanted behavior. First, the structural strength of the elements which support the beam at its endings is limited. If the beam requires a stronger force to bend, a higher solicitation will be transmitted to the beam support elements. If these elements are not able to withstand the applied forces, the beam will not bend as the energy/force which was directly applied to it, will be transferred to deformation phenomena of the surrounding components. This will lead to a higher global door penetration which, specially close to the A pillar, in node 0, where a greater force is transmitted to the supports due to the proximity to the bending axis. The second factor is related to force distribution. In the side impact collision test, the force is applied through a wide barrier over an area which extends beyond the side intrusion beam's length. When a side intrusion beam is installed, the force distribution field is affected by the higher rigidity of this element and concentrated in the beam region. In other words, there is a load transfer caused by the introduction a of a more rigid element. As a consequence, the beam region will be responsible for absorbing a greater portion of the impact energy and consequently will suffer a greater deformation, whereas the rear region of the vehicle, also impacted by the barrier will show a smaller deformation. This load transference occurs in the

opposite direction of a desirable scenario. The beam's purpose is to help absorbing and transferring the impact energy away from the passenger region and not to focus the crash force in the region where the occupants are seated. This deformation pattern variation is visible in Figure 6.11. The rear region which precedes the door panel, also directly impacted by the barrier, shows a greater displacement in the no beam scenario. The visible reduction in this region's deformation when $Beam5$ is installed is compensated by a higher deformation throughout the door's inner panel. The loads are concentrated on the side intrusion beam. As the beam's rigidity increases, so it does the load concentration phenomenon. This is why, even when seen from the local referential, the displacement curve of the no beam scenario is so many cases better than having the reference beam and in some cases better than having $Beam950$ or even $Beam5$. This means that, even if the surrounding components are improved to provide the necessary sustain to the involved bending forces, the use of a side intrusion beam is not always advisable. For example, the reference beam is, in no case, a good solution for this particular vehicle, as it consistently presents a larger deformation both in the global and local axis systems. $Beam5$ and $Beam950$, given this particular vehicle, increase the panel intrusion. However, as they present a panel deformation inferior to the no beam scenario, in case of improvement of the surrounding elements' rigidity, this better local patterns may eventually provide a certain improvement to the overall crash performance.

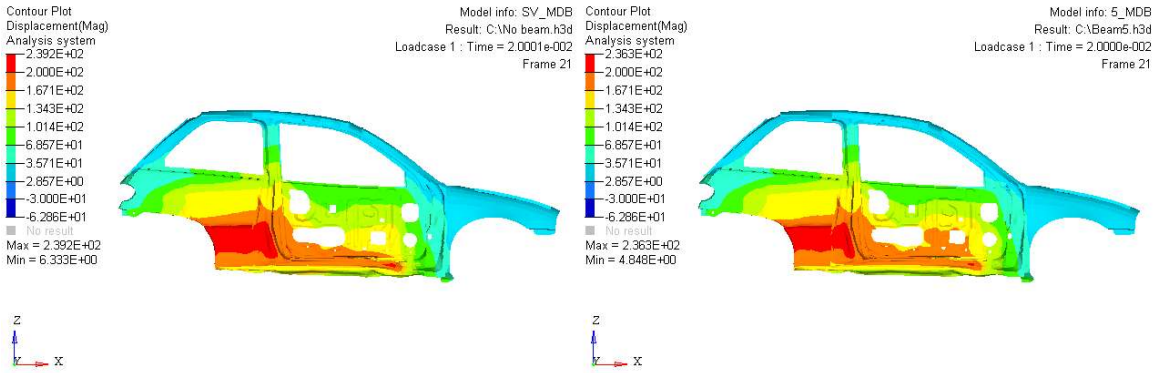

Figure 6.11: Front and rear extended analysis of the impact displacement at $t = 0.02s$

Overall, it may be concluded that, in a side collision impact test, the use of a side intrusion beam has not been proved as beneficial towards the increase in passengers safety. A better performing beam displays an improved local deformation pattern, but the increase in rigidity leads to other phenomena such as loads concentration and excessive external solicitations, which ultimately result in a globally lower crash performance. This conclusion has its own limitations. A rigid barrier was used, which increases the load concentration, and crash performance is being measured solely by the barrier's intrusion. Other factors should be considered, such as the acceleration levels induced on the passengers. These can be measured with dummy models, not available in the context of this thesis. A greater deformation leads to a greater value of absorbed energy, which means that less kinetic energy is transferred to the impacted vehicle and its passengers. An excessive deformation, however, can cause severe damages to the passengers, either by direct impact or by compartment crushing. The answer for the best solution relies on a structure that absorbs and transfers the largest amount of impact energy, providing simultaneously the required stiffness to ensure that the external object intrusion is controlled.

6.2 Side Pole

The side pole test test aims to study the impact effects of the tested vehicle against pole-like structures, such as tress or signposts. The following procedure is not, however, required to achieve vehicle homologation, thus no regulations are available. For this reason, the EuroNCAP test procedure is used [25] to build the simulation setup. This entity performs a comprehensive set of tests which go beyond the european requirements in order to ensure the maximum safety for both vehicle passengers and pedestrians. Similarly to section 6.1, here the results will also be analyzed recording the door's inner panel imposed displacement.

6.2.1 Crash Test Setup

The side pole test setup has some similarities to the side impact collision procedure previously described. Both the vehicle and the side intrusion beam configurations are identical to the ones described in section 6.1.1. This means that the test will be performed with the same Geo Metro model and with all four beam configurations (no beam, reference beam, $Beam950$ and $Beam5$). Nonetheless, the moving deformable barrier is replaced by a pole and some of the impact configuration setting differ from one test to another. Those differences are now described.

Pole

Instead of a deformable barrier, the side pole test analyzes the crash between the studied vehicle and a rigid pole, in which case the rigid assumption made during the simulation is totally valid. For this reason, the material selection during the simulation is irrelevant, since no mechanical behavior is expected nor the pole's mass has any influence in the results. In the side pole setup, it is the vehicle which has an initial velocity, v_i, as the pole remains static during the whole crash event. The pole is modeled using 2D shell finite elements and considered fixed. Figure 6.12 and Table 6.5 illustrate the numerical model of the pole used in this section and specify its dimensions according to EuroNCAP test procedures [25].

(a) Front view (b) Top view

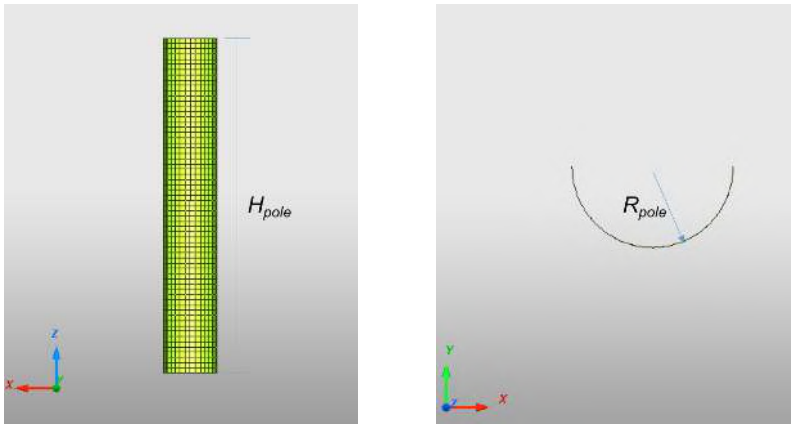

Figure 6.12: Rigid pole model

	Pole
$H_{pole}(mm)$	1530
$R_{pole}(mm)$	127

Table 6.5: Rigid pole's main dimensions (Adapted from [25])

Impact Configuration

HyperCrash will, once again, be used to compose the numerical setup. Some key features are worth a more detailed description:

- **Initial velocity** – an initial impact speed, $v_i = 8888.9mm/s$ or $v_i = 32km/h$ is applied to the vehicle with an angle of 75^o in relation to the vehicle longitudinal axis. The pole is considered static during the whole simulation.
- **Initial positioning** – Similarly to the moving barrier, the pole is positioned as close as possible from the vehicle as long as no contact activation is registered. The pole must be positioned so that the line which crosses the passenger's center of gravity with v_i direction is coincident with the center of the cylinder. This is illustrated in Figure 6.13.
- **Simulation time** – the crash event will be studied for the first $0.06s$. This period is long enough to observe a considerable displacement and limits the computational cost to acceptable values.
- **Time history** – the inner panel displacement will be measured using the nodes illustrated in Figure 6.6. For both simulation time and time history configurations, the parameters remain identical between both tests.

The final setup is illustrated in Figure 6.14. All models are developed with the explicit non-linear finite element code RADIOSS.

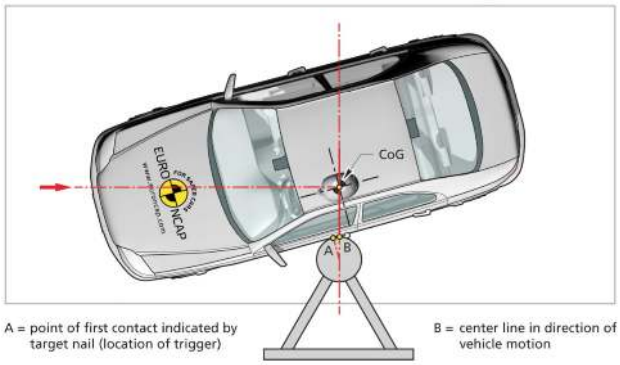

Figure 6.13: Pole positioning [25]

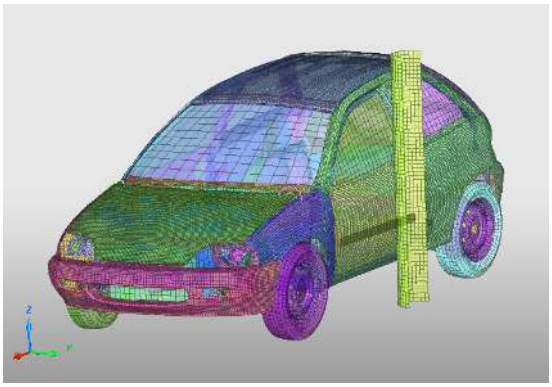

Figure 6.14: Side pole global setup

6.2.2 Crash Results

Figure 6.15 shows the inner panel displacement curves for the five levels and for the four tested solutions. In Figure 6.15 the graphic results observed in HyperView at each time step for $Beam5$ configuration are also shown. In this test, the impact speed coincides with the positive direction of the y axis.

Once again levels one and four are the least affected by the beam selection, level one being very close to the sill and level four still registering significant displacement variations close to the B pillar. As the pole is a rigid structure, the maximum panel displacement in node 5 remains constant through

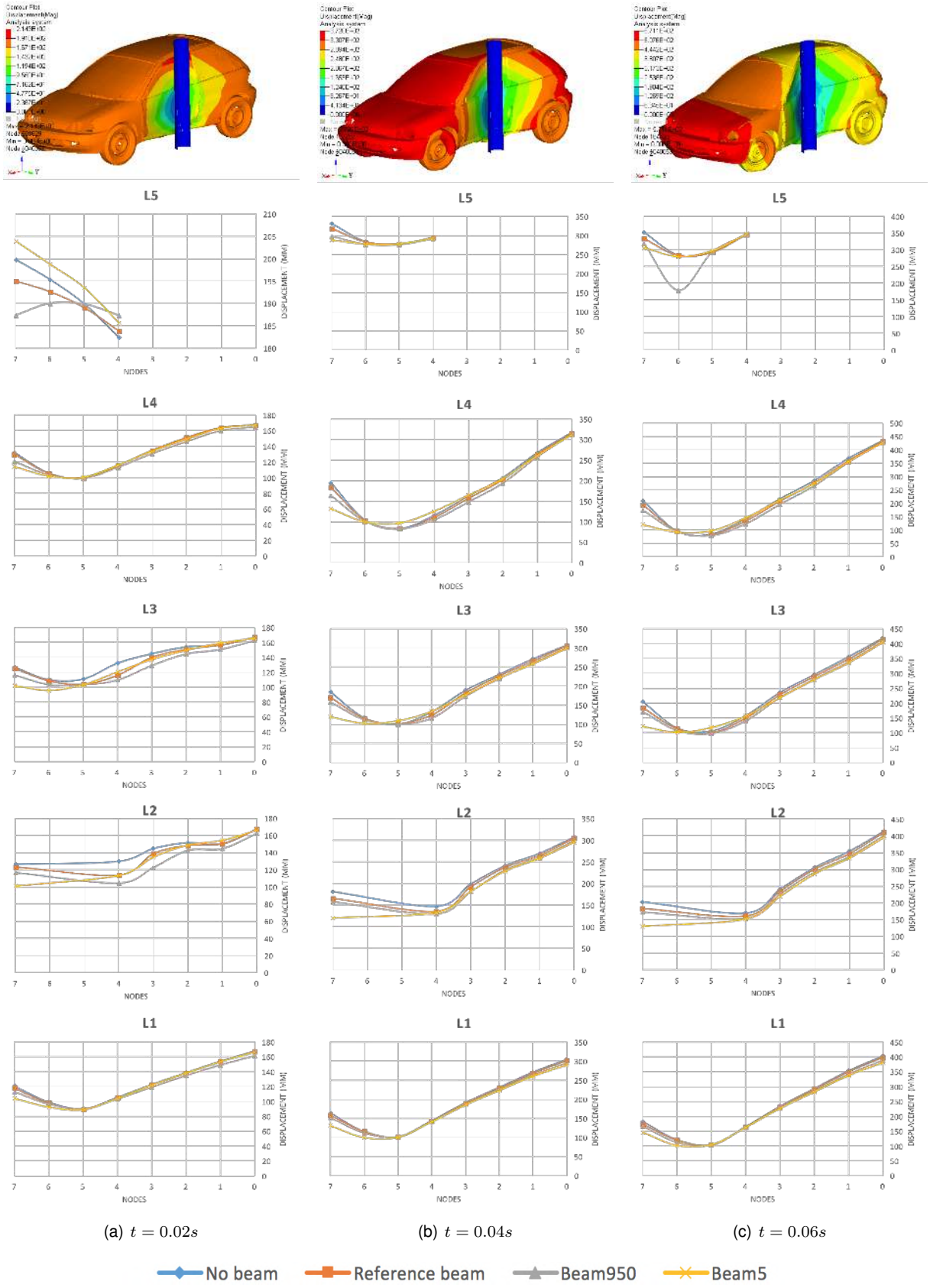

(a) $t = 0.02s$ (b) $t = 0.04s$ (c) $t = 0.06s$

Figure 6.15: Inner panel global displacement under a side pole test

time as the door crushes into the pole and the original distance of approximately $100mm$ is reduced to $0mm$. The beam's bending axis is contained by the plane formed by the cylinder central axis and the impact direction, therefore, closer to the B pillar, by opposition to the side impact collision test where the bending axis was much closer to the A pillar. The physics of a side pole test differ from the previous crash configuration because in this case it is the vehicle which has an initial speed and the impact occurs between a moving object and a perfectly still, perfectly rigid pole. In addition, the impact occurs in a much more concentrated area, by opposition to the moving barrier which contacted with a great portion of the vehicle's lateral length. In this scenario, the goal is to prevent the vehicle from wrapping around the pole, as that would lead to a more significant intrusion. A more rigid solution is, therefore, a better option, even when considering the deformation patterns in a global referential. Looking at Figure 6.15, either level by level, or time step by time step, the results clearly show a link between a better bending performance and a decrease in panel displacement. $Beam5$ displays in every scenario the best bending pattern and the no beam configuration tends to suffer the highest intrusion levels.

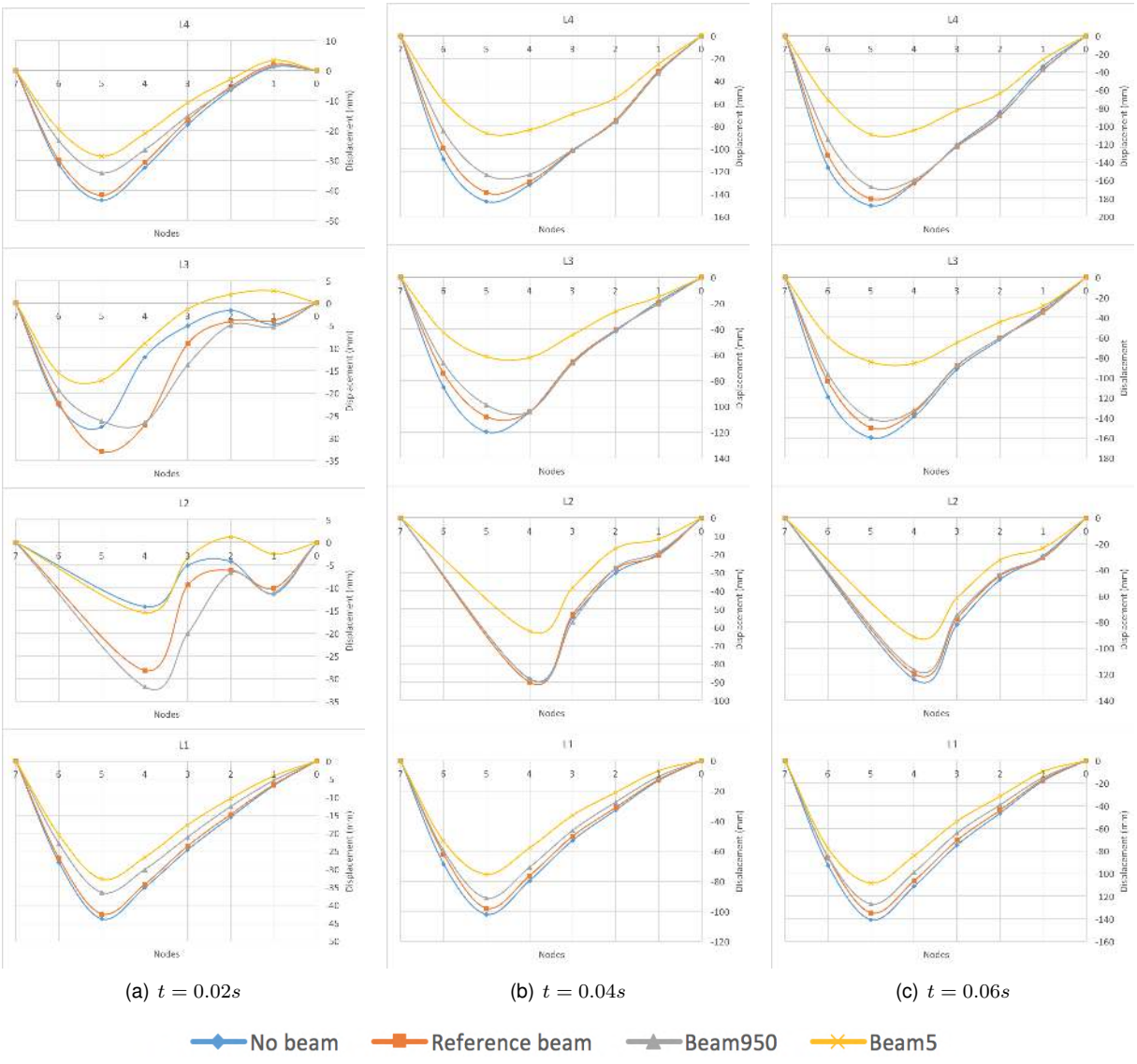

(a) $t = 0.02s$ (b) $t = 0.04s$ (c) $t = 0.06s$

Figure 6.16: Inner panel local displacement under a side pole test

The results become even more evident when observed in the local referential. Here the deformation curves show even better the improvement associated with a greater bending performance, and even if in levels two and three, show an initial unexpected positive behavior of the no beam configuration, it soon vanishes and in the following time steps the effect of a side intrusion beam becomes evident. It is no coincidence that the side pole test shows such a good relationship between bending performance and deformation pattern. As a matter of fact, the bending performance of the beam was computed through a three-point bending test whose procedure solicits the beam in a similar way to the side pole test. An important observation is that, in opposition to the side impact collision test, here the no beam scenario always shows a worse bending pattern than even the reference beam (provided enough simulation time). This results from the different crash natures which differentiate both tests. In a side pole test, the crash event is much more focused and if a side intrusion beam is logically installed in order to protect the passenger from a direct hit to the R point, it is shown, not only that even a reference beam can be beneficial, but mainly that this benefit can be greatly improved by studying ways of improving the thin-walled beam's bending performance. If in a side collision impact test the beam ends up concentrating the impact force in the door region, during a side pole test the beam absorbs and distributes the impact energy, contributing to a smaller intrusion and a better crash performance.

Overall, it may be concluded that the installation of a side intrusion beam improves the crash performance in a side pole test and that a bending performance improvement achieved through the evaluation process developed in this thesis, has a positive impact on the crash performance of a vehicle.

Chapter 7

Conclusions

The work developed in thesis was integrated in the Be project which is currently being developed at CEIIA. This project concerns the design and production of the first Portuguese vehicle 100% electric. Due to its initial phase, most of the project geometric constraints and performance requirements for the development of the side intrusion beam were still unavailable. In order to make this study commercially relevant, the focus was set on the development of a generic solution evaluation process, rather than on the search for an optimal configuration using an estimated environment whose adherence to the real project conditions would be quite limited.

Testing different side intrusion beam configurations in a real or numerical complete vehicle is proven to be a very slow and high cost procedure. In furtherance of achieving a higher bending performance, a simple three-point bending test numerical model was built using the HyperWorks tool and validated through experimental testing. This validation process led to a robust model, highly dependent on a good material description, and adaptable to different cross-section geometries.

Applying the three-point bending test numerical model on a comprehensive set of geometries and materials, and analyzing the results with an appropriate set of performance metrics, several conclusions were withdrawn in relation to the energy absorption capacity and bending pattern of thin-walled beams. A selection tool was built to integrate the several performance metrics and to provide the engineer an improved solution according to the project requirements.

Finally, the best geometries were installed in a full Geo Metro vehicle model and tested under two crash configurations: side impact collision and side pole tests. In order to study the relevance of installing a side intrusion beam, an additional no beam configuration was also tested. These results led to a better understanding of the relationship between an improvement in the beam's bending performance and its effect regarding passengers safety.

7.1 Achievements

The major achievements of the present work are now presented:

- A robust three-point bending test numerical model is built, suitable for testing thin-walled beams

with different cross-section geometries and materials (provided an accurate material stress-strain description);

- A selection procedure is designed for testing alternative beam configurations, from the initial design and bending performance assessment, to the final selection process based on the most relevant project criteria;
- Thickness increase shows the greatest improvement regarding the beam's bending performance;
- The bending pattern of a beam is influenced by both geometry and material selection. The first affects the pattern's shape and the second, mainly, its magnitude;
- In a side impact collision test, a better bending performance measured in a simple three-point bending test, leads to a better local deformation pattern, but to a worse overall crash performance;
- In a side pole test, a beam with a better performance always leads to a smaller door intrusion;

7.2 Future Work

Once the Be project advances, the door design, the volumetry constraints and the performance requirements will all become available. In this scenario a more objective solution may be studied. Understanding which criteria the reference beam does not meet, and using the provided data on geometry and material modification, new solutions may be developed oriented for the specific project design challenges.

Scientifically, it would be interesting to look deeper at the crash behavior of the vehicle. This study was mainly focused on the improvement of bending performance, leaving the crash tests to validate the importance of such improvements. It would be relevant to test and prove some of the logical conclusions inferred from the data gathered during the complete vehicle simulations. Studying, for example, how the overall crash performance can be improved by working on the beam's surrounding components mechanical properties, or fully understanding when and why it becomes relevant to use a side intrusion beam during a side impact collision test, are two analyzes which would have a significant importance in a future context.

Bibliography

[1] World Health Organization. *Global Status Report on Road Safety 2015*, 2015.

[2] A. S. Hakkert and V. Gitelman. Thinking about the history of road safety research: Past achievements and future challenges. *Transportation Research Part F*, 25:137–149, Oct. 2014.

[3] A. Ghadianlou and S. B. Abdullah. Crashworthiness design of vehicle side door beams under low-speed pole side impacts. *Thin-Wallled Structures*, 67:25–33, Mar. 2013.

[4] E. Černiauskas, A. Keršys, V. Lukoševičius, and J. Sapragonas. Investigation of anti-intrusion beams in vehicle side doors. *Mechanika*, 6(86), Jan. 2010.

[5] A. Sheshadri. Design and analysis of a composite beam for side-impact protection of occupants in a sedan. Master's thesis, VTU, India, 2002.

[6] X. Zhang, H. Zhang, and Z. Wang. Bending collapse of square tubes with variable thickness. *International Journal of Mechanical Sciences*, 106:107–116, 2015.

[7] P. Marklund and L. Nilsson. Optimization of a car body component subjected to side impact. *Struct Multidisc Optim*, 21:383–392, 2001.

[8] F. Preston and R. Shortridge. An evaluation of the effectiveness of side – door beams based on accident exposure. Special Report 1973 UM-HSRI-SA-73-8, Highway Safety Research Institute, Huron Parkway & Baxter Road Ann Arbor, Michigan 48105, September 1973.

[9] T. Tang, W. Zhang, H. Yin, and H. Wang. Crushing analysis of thin-walled beams with various section geometries under lateral impact. *Thin-Walled Structures*, 102:43–57, Jan. 2016.

[10] W. Chen. Experimental and numerical study on bending collapse of aluminum foam-filled hat profiles. *Int. J. Solids Struct*, 38(44):7919–7944, 2001.

[11] Z. Zhang, S. Liu, and Z. Tang. Design optimization of cross-sectional configuration of rib-reinforced thin-walled beam. *Thin-walled Struct*, 47(8):868–878, 2009.

[12] Be Project. `http://www.pctdamobilidade.com/en/projects/detail/6`. [Accessed November 2016].

[13] EuroNCAP – European New Car Assessment Programme. `http://www.euroncap.com/en`, . [Accessed November 2016].

[14] Bosch Mobility Solutions. http://products.bosch-mobility-solutions.com/en/de/_technik/component. [Accessed November 2016].

[15] EuroNCAP – Autonomous Emergency Braking. http://www.euroncap.com/en/vehicle-safety/the-rewards-explained/autonomous-emergency-braking, . [Accessed November 2016].

[16] National Highway Traffic Safety Administration. *Traffic Safety Facts – 2012 Data*, March 2014.

[17] European Comission – Road Safety. http://ec.europa.eu/transport/road_safety/topics/vehicles/seat_belts. [Accessed November 2016].

[18] National Center for Statistics & Analysis. *Counts of Frontal Air Bag Related Fatalities and Seriously Injured Persons*, July 2007.

[19] T. Gandhi and M. M. Trivedi. Pedestrian protection systems: Issues, survey, and challenges. *IEEE Transactions on Intelligent Transportation Systems*, 8(3), Sept. 2007.

[20] National Highway Traffic Safety Administration. http://www.nhtsa.gov/nhtsa/Safety1nNum3ers/august2013/theFactsAugust2013. [Accessed November 2016].

[21] EuroNCAP – Pedestrians Safety. http://www.euroncap.com/en/for-engineers/protocols/pedestrian-protection, . [Accessed November 2016].

[22] Volvo. http://www.volvo.com. [Accessed November 2016].

[23] United Nations Economic Commission for Europe. *Agreement Concerning the Adoption of Uniform Technical Prescriptions for Wheeled Vehicles, Equipment and Parts which can be Fitted and/or be Used on Wheeled Vehicles and the Conditions for Reciprocal Recognition of Approvals Granted on the Basis of these Prescriptions – Addendum 94: Regulation No.95*, February 2014.

[24] M. van Ratingen, A. Williams, A. Lie, A. Seeck, P. Castaing, R. Kolke, G. Adriaenssens, and A. Millerg. The european new car assessment programme: A historical review. *Chinese Journal of Traumotology*, 19(2), Apr. 2016.

[25] European New Car Assessment Programme. *Oblique Pole Side Impact Testing Protocol*, November 2015.

[26] T. H. Yoon, H. Kim, C. Heo, and J. Kwon. An experiment and fe simulation for the development of a spfc1180 ahss one-body door impact beam about a car side collision. *International Journal of Precision Engineering and Manufacturing*, 17(1):81–89, Jan. 2016.

[27] G. Davies. *Materials for Automobile Bodies*. Elsevier, 2003.

[28] World AutoSteel. *Advanced High-Strength Steels Applications Guidelines Version 5.0*, May 2014.

[29] Frost and Sullivan. *Vehicle Technologies Programme*. U.S. Department of Energy.

[30] T. Megson. *Aircraft Structures for Engineering Students*. Elsevier, 2007.

[31] N. E. Dowling. *Mechanical Behavior of Materials – Engineering Methods for Deformation, Fracture and Fatigue*. Prentice-Hall International Editions, 1993.

[32] Altair Engineering. *RADIOSS Theory Manual*, January 2014.

[33] ASTM International. *Standard Test Methods for Bend Testing of Metallic Flat Materials for Spring Applications Involving Static Loading*, 2000.

[34] O. Hechler, G. Axmann, and B. Donnay. *The Right Choice of Steel*, June 2009.

[35] ASM International. *Metals Handbook – Properties and Selection: Nonferrous Alloys and Special-Purpose Materials*, volume 2. 10 edition, 1990.

[36] United States of America Department of Defense. *Metallic Materials and Elements for Aerospace Vehicle Structures*. 2003.

[37] R. Boyer, G. Welsch, and E. W. Collings. *Materials Properties Handbook: Titanium Alloys*. 1994.

[38] National crash analysis center. `https://web.archive.org/web/20150415013506/http:/www.ncac.gwu.edu/vml/models.html`. [Accessed November 2016].

[39] MESSRING. *Side Impact – ECE-R 95*.

[40] T. L. Teng, K. C. Chang, and T. H. Nguyen. Crashworthiness evaluation of side-door beam of vehicle. *Technische Mechanik*, 28:268–278, 2008.

Appendix A

Stress-strain Curves

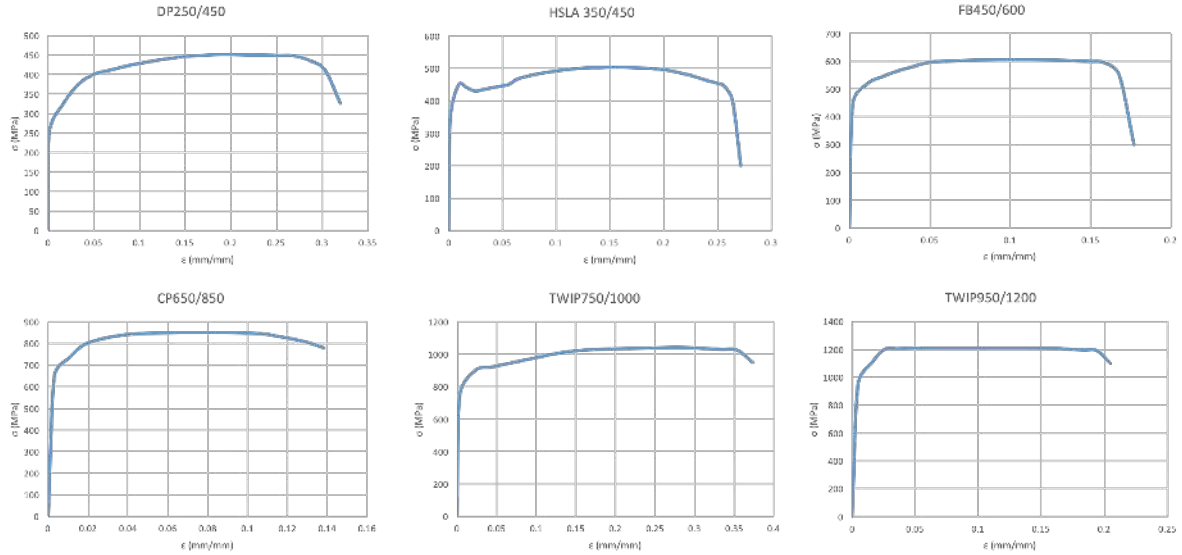

(a) Steel grades (Adapted from [28])

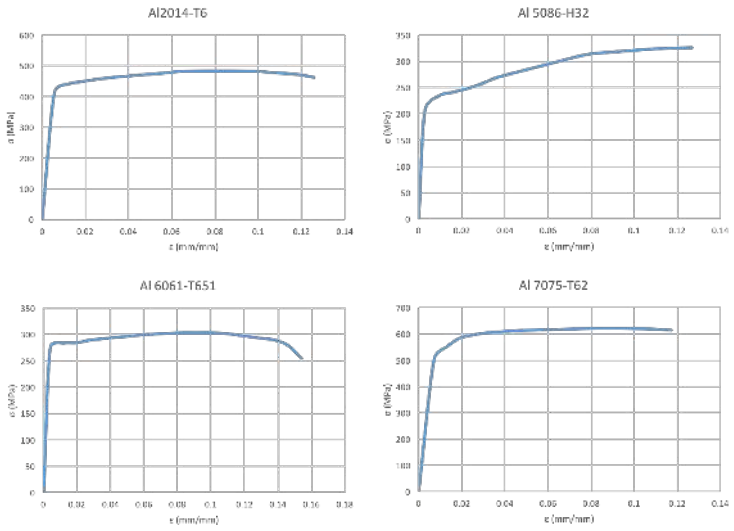

(b) Aluminum grades (Adapted from [36])

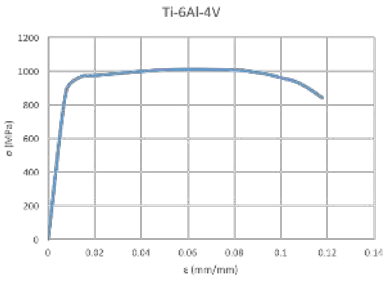

(c) Titanium grades (Adapted from [36])

Figure A.1: Stress-strain curves of the tested materials (Adapted from [28][36])

Appendix B

Force/Displacement Curves

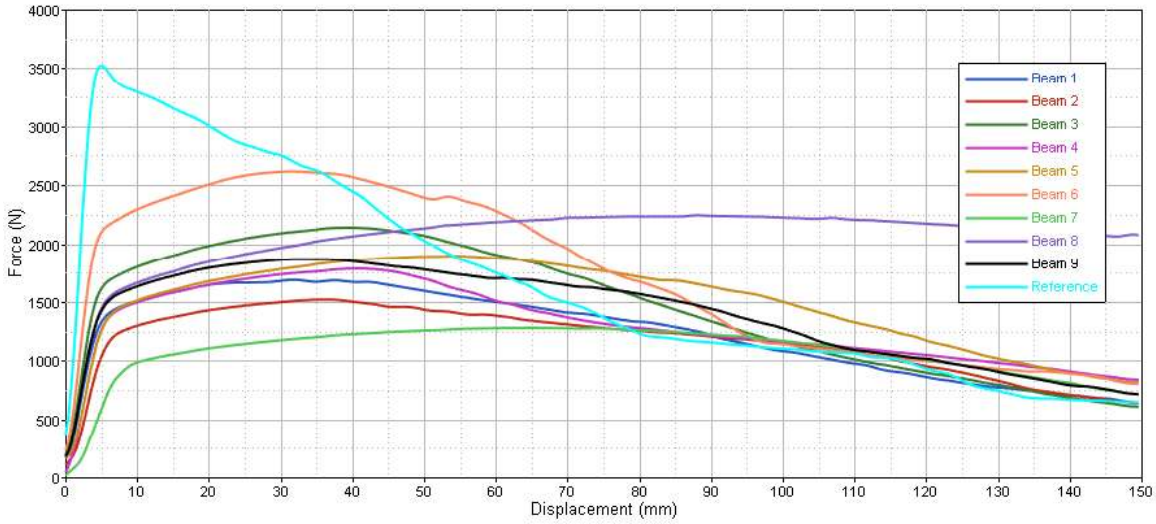

Figure B.1: Regular polygons force/displacement curves

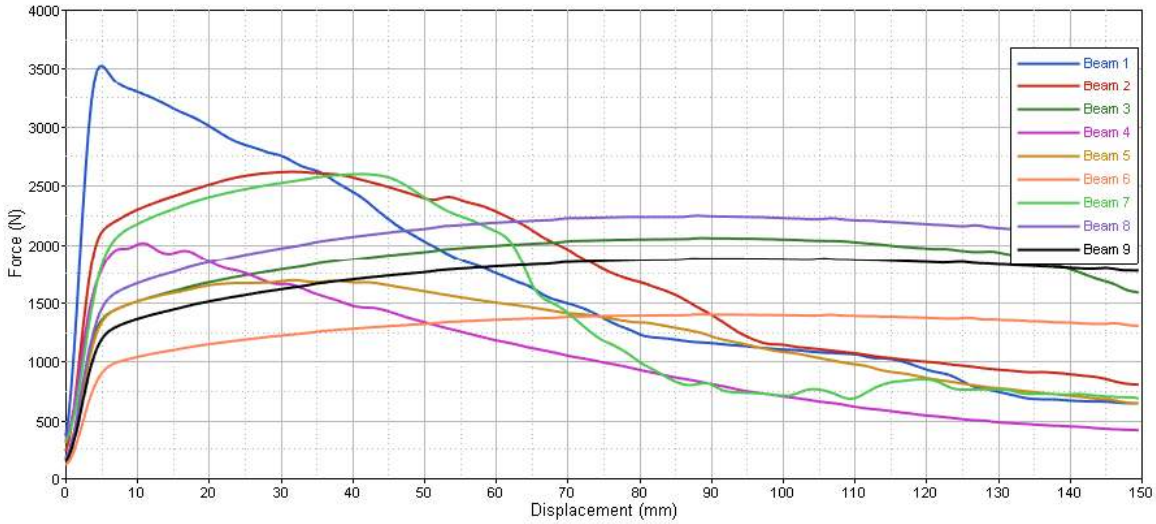

Figure B.2: Geometrical proportions force/displacement curves

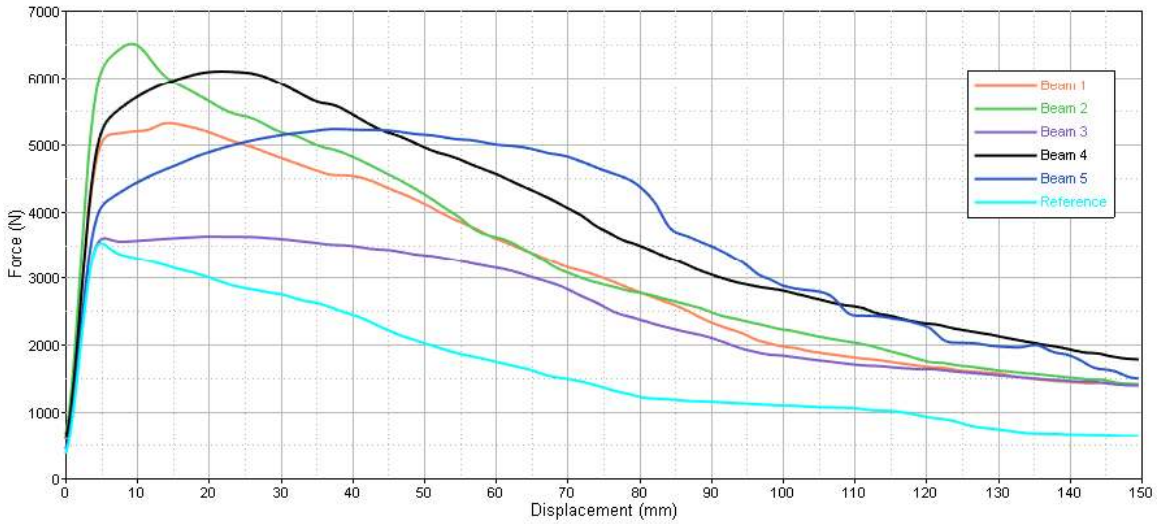

Figure B.3: Reference beam reinforcements force/displacement curves

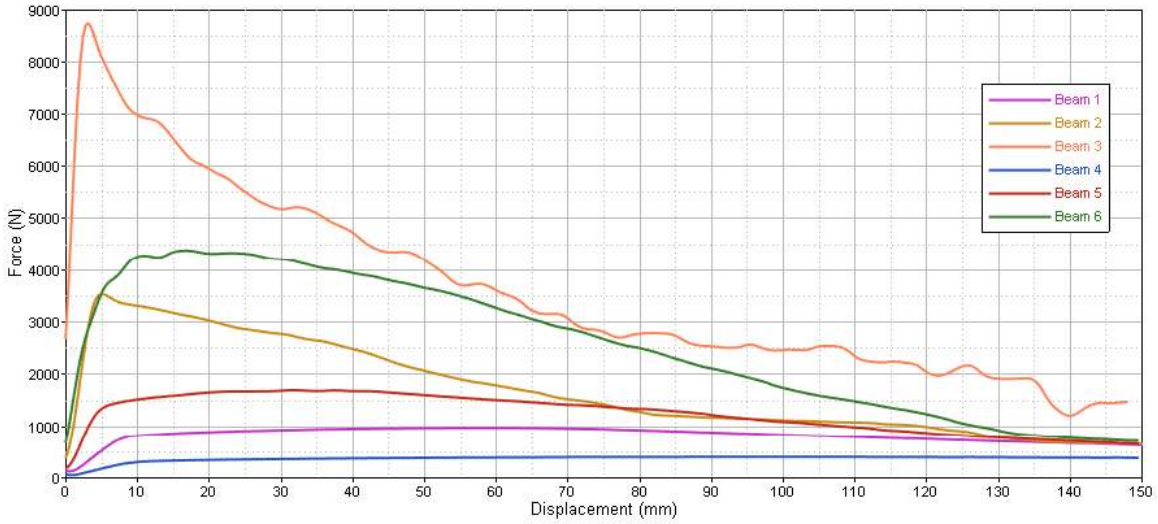

Figure B.4: Geometrical expansion/reduction force/displacement curves

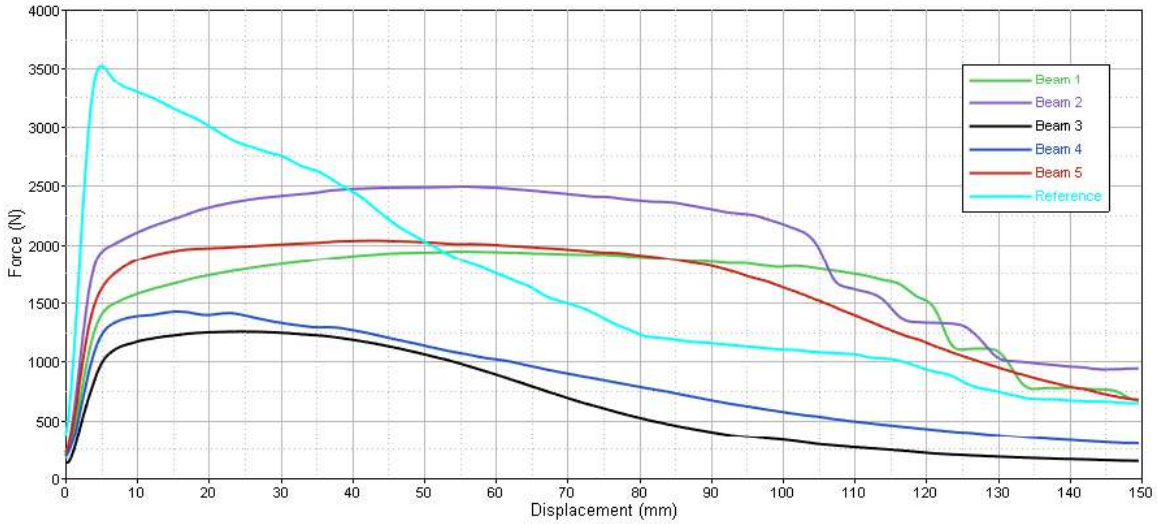

Figure B.5: Open sections force/displacement curves

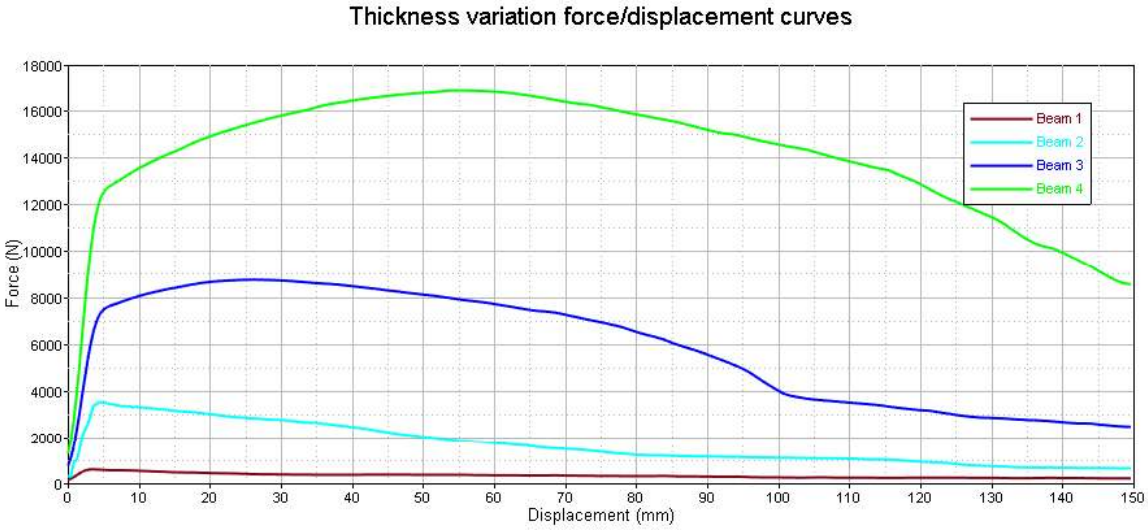

Figure B.6: Thickness variation force/displacement curves

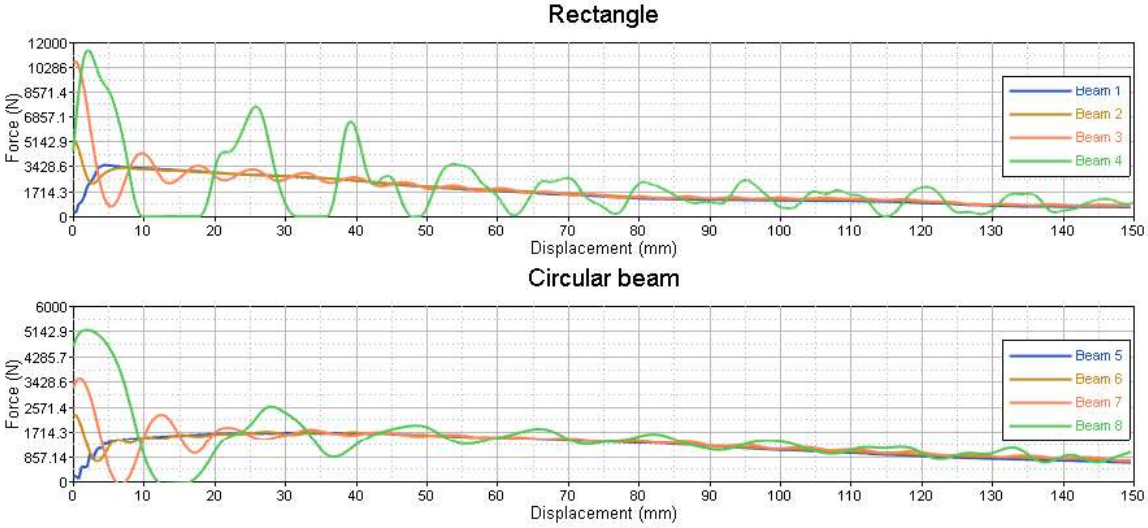

Figure B.7: Impact speed force/displacement curves

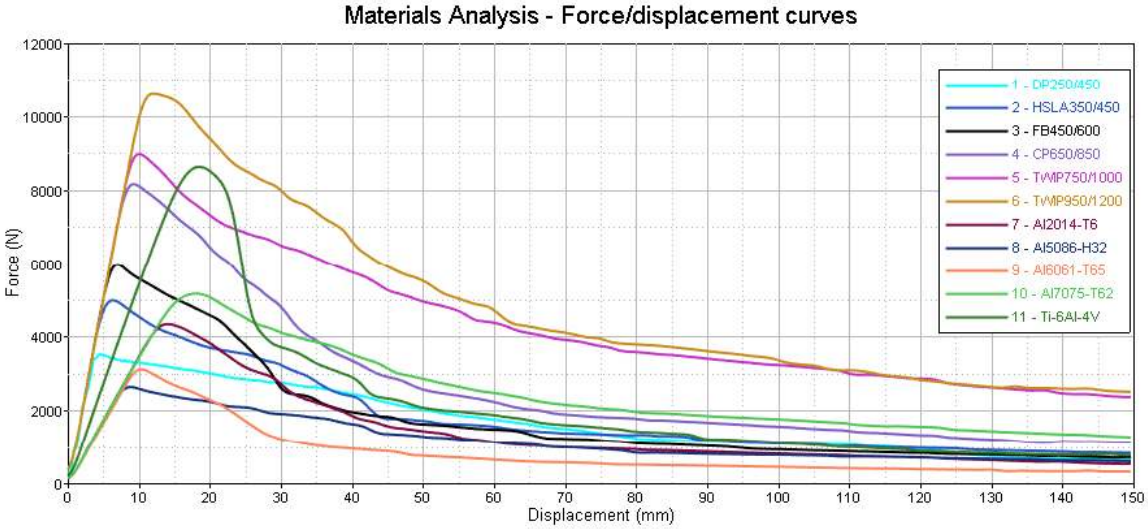

Figure B.8: Materials force/displacement curves